

Silicon Photomultiplier Classification of the Pre-Production GCT Camera of CTA

Silicon Photomultiplier Klassifikation der Pre-Production GCT Kamera von CTA

Master-Thesis von Ben Gebhardt aus Heidelberg

Tag der Einreichung:

1. Gutachten: Dr. Richard White (MPIK)

2. Gutachten: Prof. Jim Hinton (MPIK)

3. Gutachten: Prof. Tetyana Galatyuk (TU DA)



TECHNISCHE
UNIVERSITÄT
DARMSTADT

Fachbereich Physik

Max Planck Institut für Kernphysik Heidelberg

8 Silicon Photomultiplier Classification of the Pre-Production GCT Camera of CTA
Silicon Photomultiplier Klassifikation der Pre-Production GCT Kamera von CTA

Vorgelegte Master-Thesis von Ben Gebhardt aus Heidelberg

1. Gutachten: Dr. Richard White (MPIK)
2. Gutachten: Prof. Jim Hinton (MPIK)
3. Gutachten: Prof. Tetyana Galatyuk (TU DA)

Tag der Einreichung:

¹⁰
¹¹ **Abstract**

¹² whats this about



Abstract

13
14
15 worum es geht



16 List of Figures

18	1	Cosmic radiation	7
19	2	Fermi LAT	8
20	3	Cherenkov light cone	10
21	4	GCT and CHEC-M at Meudon	12
22	5	GCT optical system	13
23	6	CHEC focal plane	14
24	7	PMT and SiPM size	16
25	8	Structure and carrier multiplication through an avalanche inside a SiPM	17
26	9	Cherenkov light spectrum	18
27	10	Avalanche induced secondary effects	21
28	11	Teststand outside view	23
29	12	Thermal chamber inside view	24
30	13	Experimental setup scheme	25
31	14	Shaped versus unshaped signal	27
32	15	Zero pole cancelation	27
33	16	Multi p.e. persistence plot	28
34	17	Pulse height spectrum generated by the oscilloscope	28
35	18	Pedestal subtraction	31
36	19	Peak Detection	32
37	20	Fitted pulse area histogram	33
38	21	Regression line plots of 1p.e. and Δ p.e.	34
39	22	MPD parameter challenges and the integration window	36
40	23	MPD parameter challenges and the threshold	37
41	24	List of examined SiPM devices	39
42	25	CHEC-S SiPM	41
43	26	CHEC-S average pulse shape	41
44	27	CHEC-S gain	42
45	28	CHEC-S DCR	43
46	29	CHEC-S OCT	44
47	30	LCT5 6mm SiPM	46
48	31	LCT5 6mm average pulse shape	46
49	32	LCT5 6mm gain	47
50	33	LCT5 6mm DCR	48
51	34	LCT5 6mm OCT	49
52	35	LCT5 7mm SiPM	50
53	36	LCT5 7mm average pulse shape	50

54	37	LCT5 7mm gain	51
55	38	LCT5 7mm DCR	52
56	39	LCT5 7mm OCT	52
57	40	LCT5 LVR 6mm SiPM	53
58	41	LCT5 LVR 6mm average pulse shape	53
59	42	LCT5 LVR 6mm gain	54
60	43	LCT5 LVR 6mm DCR and OCT	54
61	44	SensL FJ60035 SiPM and average pulse shape	56
62	45	SensL FJ60035 gain	57
63	46	SensL FJ60035 DCR and OCT	57
64	47	DCR device comparison	59
65	48	OCT device comparison	60
66	49	Comparison based on two proposed points of operation	63
67	50	PDE versus OCT comparison	64
68	51	PDE results from the University of Nagoya	64
69	52	CTA in Chile and the stereoscopic technique	69
70	53	Current IACT experiments	69
71	54	OCT dependency on the cell-size	70
72	55	Pulse area spectra of three different integration windows	73
73	56	Breakdown-voltage versus temperature	74
74	57	Breakdown-voltage dependency	75
75	58	Shaped versus unshaped signal	76
76	59	Full schematic of the shaper developed at the University of Leicester.	76
77	60	List of devices in testing at the University of Nagoya, Japan.	78
78	61	CHEC-S pixel comparison of the gain	79
79	62	CHEC-S pixel comparison of the DCR	79
80	63	CHEC-S pixel comparison of the OCT	80
81	64	Description	81
82	65	Description	82
83	66	Description	83
84	67	Description	84

85 **Contents**

87	1 Cosmic Radiation	7
88	1.1 Air shower induced Cherenkov Radiation	9
89	1.2 Imaging Atmospheric Cherenkov Telescopes	10
90	2 Cherenkov Telescope Array	12
91	2.1 Gamma Cherenkov Telescope	13
92	2.2 Compact High Energy Camera	14
93	3 Silicon Photomultipliers	16
94	3.1 SiPM characteristics	16
95	3.2 Gain of a Silicon Photomultiplier	19
96	3.3 Thermally induced dark counts	20
97	3.4 Avalanche-induced secondary effects	20
98	3.5 Photon Detection Efficiency	22
99	4 Experimental Setup	23
100	5 Data Analysis	30
101	5.1 Tracefile Conversion	30
102	5.2 Pedestal Subtraction	31
103	5.3 Peak Detection	32
104	5.4 Gain Extraction	33
105	5.5 Analysis improvements	35
106	5.6 Data Challenges	36
107	6 Results	39
108	6.1 SiPM devices for CTA	39
109	6.2 Hamamatsu S12642-1616PA-50 50 μ m 3mm	41
110	6.3 Hamamatsu LCT5 50 μ m 6mm	46
111	6.4 Hamamatsu LCT5 75 μ m 7mm	50
112	6.5 Hamamatsu IVR 50 μ m 6mm	53
113	6.6 SensL FJ60035 6mm 35 μ m	56
114	7 Comparison	58
115	7.1 Dark Count Rate	58

116	7.2 Optical Cross Talk	59
117	7.3 Point of Operation Comparison	62
118	7.4 Photon Detection Efficiency	62
119	8 Conclusion and Outlook	64
120	9 Glossary	66
121	10 Bibliography	67
122	11 Appendix	69

123
124

1 Cosmic Radiation

125 Cosmic rays consist of a single particle with energies from 10^{10} to 10^{20} eV and describes extra-
126 solar charged particles arriving on Earth and hitting the atmosphere fig(1). They were discovered
127 by V.F. Hess in 1912 during the famous balloon flight experiments. He aimed to measure the
128 conductivity of air, that until then, was believed to be an insulator resulting in some problems
129 regarding the discharge of an electrically charged body, no matter how well it was isolated from
130 the ground. Hess found the air's conductivity to increase with higher altitude, concluding the
131 presence of a large amount of ionizing radiation above the atmosphere. The most energetic
132 laboratory based accelerators operate in the 10^{12} eV energy range.
133 Cosmic rays do not include those low energy particles originating from our sun. With a particle
134 energy up to 1keV, those are referred to as solar wind, which means, by definition, cosmic rays
135 arrive on Earth from outside our solar system. They consist of 87% protons, 12% α -particles
136 , 1% heavier nuclei and some electrons. High energy cosmic rays hitting Earth are very rare,
137 averaging to one per year in an area of one square kilometer. Except at those very high energies
138 ($>10^{18}$ eV) cosmic rays will not reach earth directly and can not be observed to pinpoint
139 their source. Traveling through the interstellar medium , they get scattered by the interstellar
140 magnetic fields, the cosmic microwave background and other hindrances and therefore have
141 lost all directional information. However, directly observable cosmic rays, for example at the
142 Pierre-Auger Observatory, provide an insight into cosmic particle accelerators.[2]

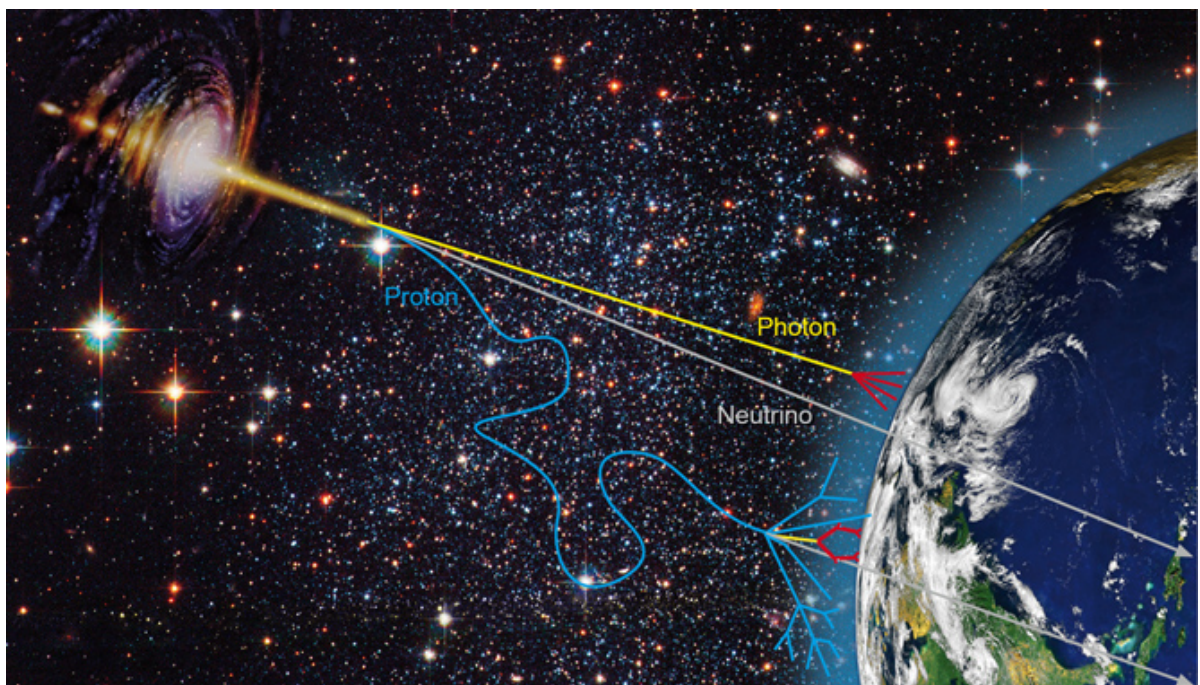


Figure 1: Gamma radiation photons (yellow) and scattered cosmic ray protons (blue) from an astrophysical source arriving on Earth. Neutrinos (grey) mostly do not interact. Picture from [26]

143 Cosmic rays of the higher energies are therefore observed via a detour: Gamma radiation.

144

145 Gamma radiation cannot be generated by
146 thermal emission of hot stellar objects, the
147 only event with a high enough temperature
148 to produce thermal radiation in the range of
149 GeV and TeV gamma radiation would be the
150 big bang, there is and has been nothing else
151 in the known universe. If thermal radiation
152 reflects the temperature of the emitting body,
153 what do gamma rays tell us?

154 Gamma radiation probe a non-thermal uni-
155 verse. In this one needs other mechanisms
156 to concentrate large amounts of energy into a
157 single quantum. The possible emission mechanisms are outlined below.

158 There are many diverse mechanisms of emitting gamma radiation. Gamma rays are generated
159 by high relativistic particles, in a first step for example: accelerated by the shockwave of a su-
160 pernova explosion. Those cosmic rays then collide with ambient gas, interact with photons or
161 magnetic fields, by inverse compton scattering, emitting high energy photons (down-top). Very-
162 high-energy (VHE) gamma radiation is defined as gamma radiation in the energy range of 10^{11}
163 to 10^{14} eV.

164

165 One such source of VHE gamma radiation and also the most famous, because the first to be
166 discovered, lies within the Crab Nebula. The Neutron Star located inside the Crab Nebula is a
167 Pulsar and the remnant of Supernova1054 and steadily emits gamma radiation energies up to
168 80 TeV. Another compound of the gamma radiation here is the so called Pulsar Wind Nebula. It
169 is composed of highly relativistic charged particles from the Pulsars giant rotating magnetic field
170 interacting with the expanding Supernova remnant via inverse compton scattering. Supernova
171 shockwaves themselves can also drive atomic nuclei to high energies which in turn emit observ-
172 able gamma-rays in a top-down fashion. Additionaly, binary systems consisting of a black hole
173 or pulsar orbiting a massive star can emit a flow of high-energy particles with variing intensity,
174 based on the elliptical orbit, where particle acceleration conditions vary.

175 So just like thermal radiation reflects the temperature of the emitting object, the flux and en-
176 ergy spectrum of the gamma rays reflect the flux and spectrum of the high energy seed particles,
177 coming from the source. So they can be used to trace these cosmic rays and electrons in distant
178 regions of our own galaxy or even beyond.

179 One surprise was the discovery of so called "dark sources" , objects emitting VHE gamma-rays,
180 but have no counterpart in other wavelenghts, meaning those objects might only be observable



Figure 2: FermiLAT Picuture from [27]

181 through gamma-rays. In extragalactical regions, gamma rays provide information on active
182 galaxies, where a constant stream of gas feeds a supermassive black hole at the center, releasing
183 enormous amounts of energy. From there, gamma rays are believed to be emitted, giving insight
184 into one of the most violent but to date poorly understood environments in our universe.

185 Even higher energy gamma rays could also be the product of decays of heavy particles, like
186 dark matter or cosmic strings. They therefore also provide a window to the discovery of dark
187 matter.

188

189 Gamma Radiation carries unique information about the most energetic phenomena in our
190 universe. The only problem is, our atmosphere is opaque for gamma radiation, gamma ray as-
191 tronomy in the lower energies is done by satellite based instruments like FermiLAT. The Large
192 Area Telescope, the principle scientific instrument on the Fermi Gamma-Ray Space Telescope
193 Spacecraft sensitive in the energy range between 20 MeV and 100 GeV, launched in June 2008.
194 fig (2) To reach the higher energy range through space based telescopes is very inconvenient,
195 since the required mass the telescope active area would need to detect the gamma rays increases
196 with gamma ray energy, and can therefore be very expensive to launch into space. Low energy
197 gamma rays can be efficiently captured by a volume appropriate for a spacecraft, for higher en-
198 ergy gamma rays using other interaction and detection media, like water or Earths atmosphere,
199 is more viable.

200 **1.1 Air shower induced Cherenkov Radiation**

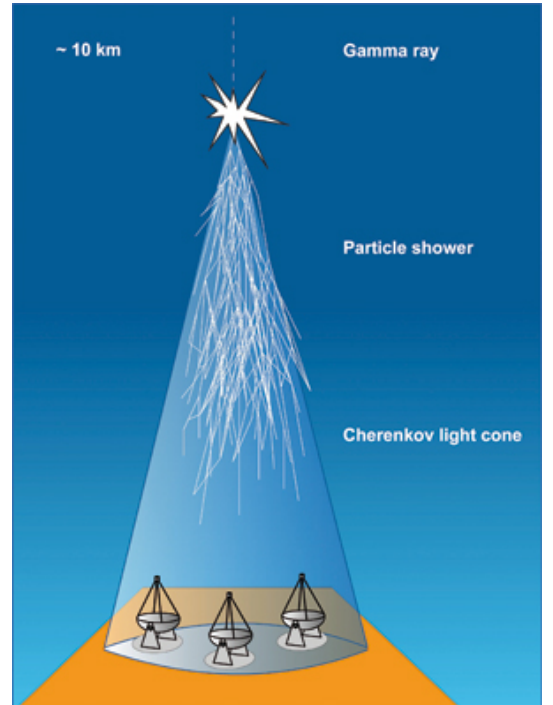
201 The effect of gamma radiation on Earth is visible through gamma-ray induced particle cascades.
202 When a primary particle, i.e. a gamma photon or cosmic ray enters the atmosphere and collides
203 with a nucleus of the air, it gets scattered and creates secondary electrons, positrons and pho-
204 tons. Those secondary particles also interact with the atmosphere creating a cascade of particles
205 called a particle shower.

206 In this air shower, the initial and each subsequent particle traveling through our atmosphere
207 emits Cherenkov light. Cherenkov radiation is a phenomenon caused by charged particles trav-
208 eling faster than the local speed of light would allow in that medium. This light is emitted in a
209 narrow cone with an increasing angle as the particles travel downward. This Cherenkov light
210 shows as a very short ($\sim 5\text{ns}$) flash with a peak in the UV-spectrum at around 330nm. Thus, we
211 can image the particle cascade measured with the telescope and can reconstruct the direction
212 and energy through a stereoscopic image of the shower taken by multiple telescopes (see sec-
213 tion A), reconstructing the position of the source in the sky. It is also possible to reconstruct the
214 energy of the original photon from the amount of light produced, because energy is conserved,
215 so all energy of the original photon is now distributed between the particles of the shower.
216 To determine whether it is a hadronic shower, originating from cosmic rays, or a gamma shower,

218 originating from gamma ray photons, the shape of the shower and so called Hillas parameters
219 are used to determine the difference.

220 221 1.2 Imaging Atmospheric Cherenkov Telescopes

222 The technique, pioneered by the Wipple Collaboration
223 behind the ground based experiments called
224 Imaging Atmospheric Cherenkov Telescope (IACTs)
225 aims at measuring the time, direction and energy
226 of flashes of Cherenkov light from extensive air
227 showers caused by VHE gamma radiation. Those
228 ground based instruments have a much larger ef-
229 fective detection area than any satellite based in-
230 strument, which have a typical detection size of
231 1m^2 . The range of the Cherenkov flash being be-
232 tween 300-600nm, current generation Silicon Photo-
233 multipliers (SiPMs) are a promising candidate to re-
234 place the progenitor photon detector used in previ-
235 ous experiments like HESS, the Photomultiplier Tube
236 (PMT).



237
238 **Figure 3:** The cone of Cherenkov light
239 emitted by an extensive air
240 shower. Picture from [28]

241 Current ground based IACT experiments are HESS,
242 MAGIC and Veritas. (see section B) HESS¹, based in
243 Namibia, consists of four telescopes the size of 12 m
244 operating in the energy range of 3 GeV to 100 TeV. The
245 chosen name is in honor of Victor Hess, the first to discover cosmic rays. The recent HESS
246 upgrade added a fifth larger telescope in the center of the array with a mirror diameter of
247 28 m. MAGIC², based in La Palma one of the Canary Islands, is a system consisting of two
248 17 m diameter telescopes at 2200m asl³, covering the energy range 30 GeV and 30 TeV. Veri-
249 tas⁴, operating between 50 GeV - 50 TeV consists of four 12 m telescopes, based in Arizona, USA.

250
251 Due to the limited effective area, caused by the number of telescopes spread over a wide area,
252 most cascades are viewed by only 2 or 3 of the telescopes. Additionally, due to the low flux of
253 VHE gamma radiation, detectors for this energy range are spread over a large area, making
254 space based instruments, which detect the incident gamma ray, an inconvenient choice.

¹ High Energy Stereoscopic System

² Major Atmospheric Gamma Imaging Cherenkov Telescopes

³ above sea level

⁴ Very Energetic Radiation Imaging Telescope Array System

253 Another detection concept for VHE gamma radiation are ground based air shower particle
254 detectors such as the High-Altitude-Water-Cherenkov observatory (HAWC) [6]. It employs a
255 similar detection principle, recording shower particles reaching arrays of ground based particle
256 detectors filled with water as detection medium, in contrast to air in IACTs. Those have the
257 advantage of a larger duty cycle than IACTs, as they are able to operate during the day. Their
258 limited sensitivity even with high observation time however will not allow them to compete
259 with the sensitivity and resolution of IACTs such as in the CTA. The array will however be able
260 to provide useful complementary information.

²⁶¹ 2 Cherenkov Telescope Array

²⁶² The Cherenkov Telescope Array, CTA, is a proposed ground-based observatory array of many tens of telescopes distributed over a larger energy range than before. It will allow detection of gamma rays over a large area on the ground and from multiple different directions. The array will consist of 60 - 100 telescopes of different designs and sizes to cover the aimed for energy range and area. Science goals are the understanding of cosmic rays and their role in the universe, including the study of cosmic particle accelerators, such as pulsars, pulsar wind nebulae , supernova remnants and gamma ray binaries. Secondly particle acceleration around black holes of supermassive or stellar size and lastly physics beyond the Standard Model. There are currently three groups of telescopes planed, differing in their size and achievable energy range:[2]



Figure 4: The GCT Structure with mounted CHEC-M at the Observatory at Meudon, Paris, one of the telescopes of CTA.

- ²⁸⁵ 1. LST⁵ The low energy instrument, between 20 and 200 GeV, is a 23 meter class telescope with a moderate field of view (FoV) of about 4.5°.
 - ²⁸⁷ 2. MST⁶ The medium energy range, from around 100 GeV to 10 TeV, is covered by a telescope of the 12 meter class with a FoV of 7°.
 - ²⁸⁹ 3. SST⁷ The high energy instrument, operating between a few TeV to 300 TeV, is a 4 meter telescope with a FoV ranging from 9.1° to 9.6°.
- ²⁹¹ There are currently two sites planed, which when deployed, will achieve full-sky coverage. The ²⁹² southern site in the Atacama Desert in Chile, one of the most driest and isolated regions on ²⁹³ Earth, will consist of four LSTs, 24 MSTs, and about 70 SSTs covering an area of 4 km². The

⁵ LST large sized telescope

⁶ MST medium sized telescope

⁷ SST small sized telescope

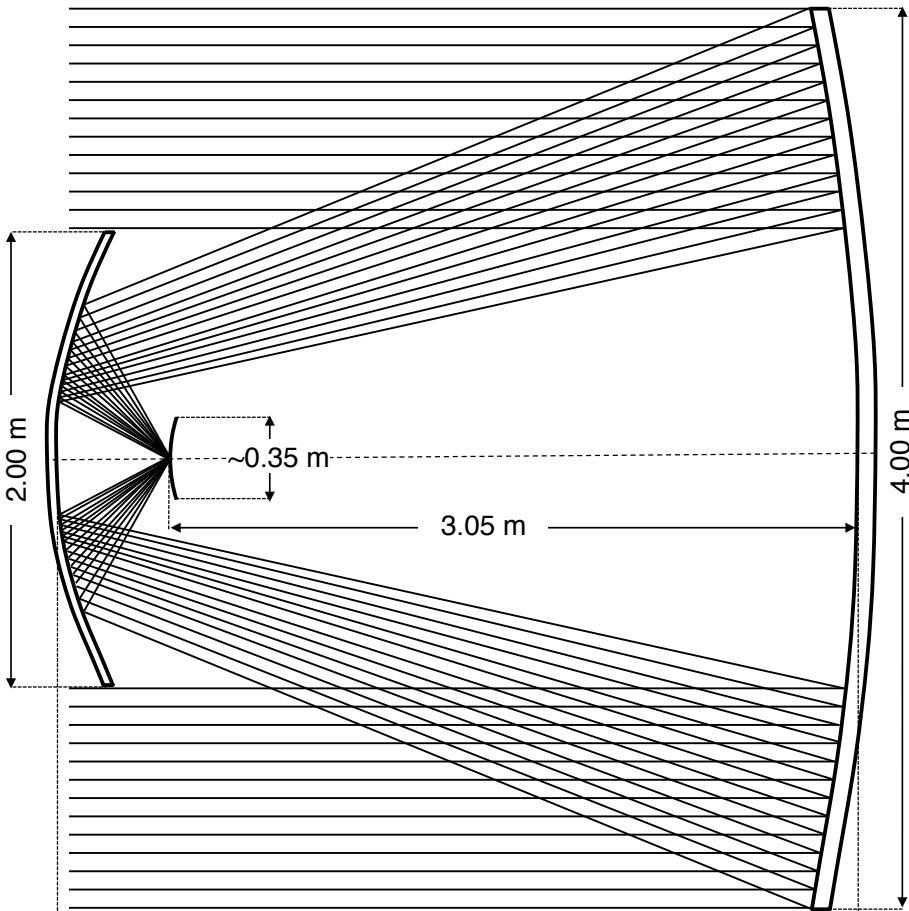


Figure 5: Optical mirror system of the GCT telescope. A primary(4 m)-secondary(2 m) mirror optics system focuses the light onto a 0.35 m camera focal plane.

294 northern site will only cover 0.4 km^2 and will only contain four LSTs and 15 MSTs due to spac-
 295 ing reasons with the MAGIC observatory at the same location at the Roque de los Muchachos
 296 Observatory on La Palma, one of the Canary Islands.

297
 298 One proposed concept for the SST is the Gamma Cherenkov Telescope (GCT) fig(4).
 299

300 **2.1 Gamma Cherenkov Telescope**

302 The reflector design of IACTs traditionally consists of multiple mirror segments, which focus the
 303 incident light onto a camera covering $\sim 1 \text{ m}$ with pixels $\sim 25 \text{ mm}$ in diameter. Such a reflector
 304 design is proposed for both, the LST and the MST of CTA resulting in the telescope sizes men-
 305 tioned in Section 2 above, that will use the traditional PMTs fig(7)(left).

306 For the SST such a design would result in a cheap telescope structure, but a disproportionately
 307 expensive camera, i.e. the cost and size of the structure is reduced, while the cost of the camera
 308 is not. The cost of one SST camera would be near the cost of a MST camera, which given the

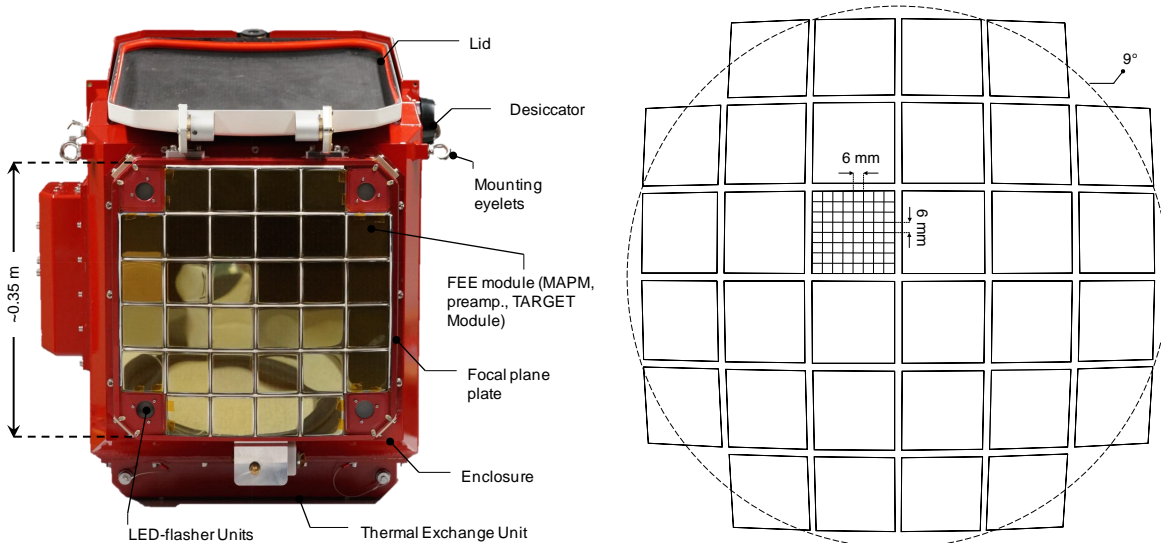


Figure 6: Front view of the CHEC-M prototype (left), view of the camera focal plane. Schematic of the focal plane (right), illustrating the 9° FoV with 6mm² pixels. Pictures from [18]

309 number of SST telescopes at the southern site is inconvenient.
 310 The alternative solution is the reduction of the camera plate scale through a dual-mirrors de-
 311 sign allowing the use of more affordable photosensots. The optical system of the telescope is
 312 complemented with a secondary mirror added to the primary mirror. This shortens the effective
 313 focal length so the focal surface will lie between primary and secondary mirror fig(5). This
 314 optical design is based on the Schwarzschild-Couder design first produced by Karl Shwarzschild
 315 (Schwarzschild, 1905) and later refined by Couder (Couder, 1926) and then adapted for use
 316 in IACTs by Vassiliev and Fegan [10]. With the dual-mirror design optimised for GCT by Blake
 317 et al. [11] the camera plate scale is reduced, allowing the use of more affordable photosen-
 318 sors, Silicon Photomultipliers (SiPMs) and multi-anode photomultipliertubes (MAPMTs) among
 319 them, potentially reducing the cost of each SST.

320 2.2 Compact High Energy Camera

322 The Compact High Energy Camera, or CHEC fig(6) is one of three prototype camera concepts in
 323 development for one of the SST structures within CTA. One camera features 2048 photosensors,
 324 building equally many readout channels per camera. The readout is done by so called TARGET⁸
 325 modules for sampling, digitization and triggering, one of those consists of 4 ASICs⁹ with 16
 326 channels each. The camera houses 32 TARGET modules, one of them responsible for readout
 327 of 64 photosensors. The TARGET modules build the front-end of the integrated electronics¹⁰
 328 inside the CHEC camera connecting the buffer to the cameras backplane. After the photosensor

⁸ TARGET TeV Array Readout with GS/s sampling and Event Trigger

⁹ ASIC Application Specific Integrated Circuit

¹⁰ FEE front end electronics

329 is triggered the buffer amplifies the signal, that is then send to the ASIC inside the TARGET
330 modulde, where an analog-to-digital converter and a shaper convert the signal before it is send
331 to the backplane for transfer to the main array hub. Two iterations of the CHEC camera are
332 tested, CHEC-M is the first design based on MAPMs as photosensors and was the initial pro-
333 tototype platform all improvements to the electronics are tested on. CHEC-M since then moved
334 to Meudon in Paris and is now mounted on the GCT structure for further testing of the entire
335 GCT prototype. The second iteration of the camera: CHEC-S, based on SiPMs as photosensors
336 is a similar concept, with applied improvements to electronics and mechanical design. The two
337 cameras are similar in shape and can both be mounted on the GCT structure with minor alter-
338 ations.

339

340 In order to make an educated choice on the best SiPM device to use to populate the cameras
341 focal plane, an in-depth characteristic study on pulse-shape, gain, temperature-dependence,
342 detection efficiency, thermal noise and correlated secondary effects is conducted by multiple
343 groups within the CTA collaboration.

344

345 This paper studies the gain, noise from thermal, as well as correlated secondary effects and
346 their temperature dependence.

3 Silicon Photomultipliers



Figure 7: The size of the photodetector still used in progenitor IACT experiments (PMT)(left) compared to an SiPM(right). Picture from [23]

349 Silicon Photomultipliers (SiPMs) are semiconductor photo detectors, that have attracted in-
 350 creased attention over the last decade for their possible use in astroparticle physics. The sensor
 351 consists of an array of avalanche photo-diodes, typically $\sim 50 \mu\text{m}$ in size. Depending on the
 352 pixel-size, one pixel contains several 1000 diodes, hereafter called cells. Each cell is a PN junc-
 353 tion fig(8) supplied with a reverse bias-voltage above breakdown, which is called operation in
 354 Geiger-mode, in analogy to the Geiger counter. In this mode, a photon or thermal excitation will
 355 produce an electron-hole pair in the depleted region. Through impact ionization these charge
 356 carriers will in turn trigger an avalanche in a cell, which in turn generates a large output pulse
 357 typically in the range of several Mega electronvolt. This avalanche is then passively quenched
 358 by a resistor to limit the current in the substrate and to reset the cell to a quiet state so it is
 359 photosensitive again. The signal of the SiPM is the sum of the signal of all cells, read out over
 360 their quenching resistor via a common output.

361

362 3.1 SiPM characteristics

363 Silicon Photomultipliers posses major advantages over their progenitor, the Photomultiplier-
 tubes, or PMT fig(7). They are more resistent to mechanical and accidental light-exposure
 365 damage through ambient light. Silicon Photomultipliers have a lower power consumption and,
 366 operating at a much lower bias-voltage, there is no need for high-voltage as in PMT. They posses
 368 a high photon detection efficiency and are insensitive to magnetic field changes. There is rapid
 369 improvement, being a fairly new technology, with new generations every ~ 5 months and de-
 370 creasing costs per mm^2 . Viewed over all cells of the whole pixel, fluctuations in the gain are

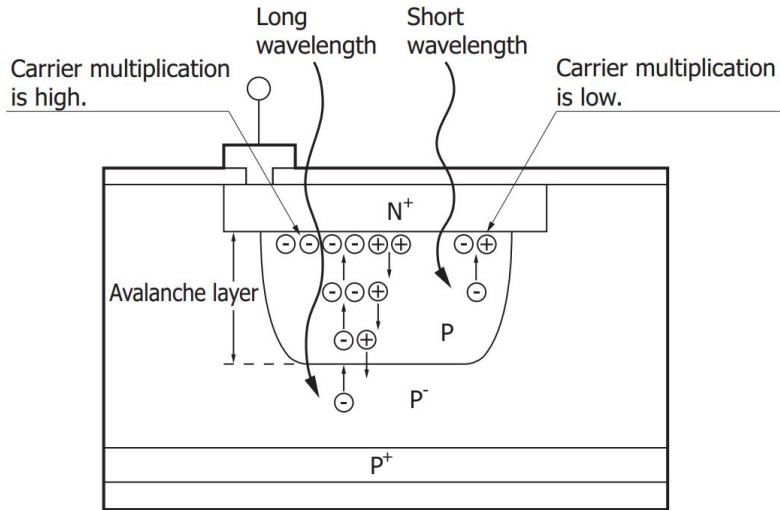


Figure 8: Structure and carrier multiplication through an avalanche inside a SiPM. Picture from [16]

371 very small. This is because of the uniformity during manufacture and visible in the width and
 372 the clear resolution of the p.e. peaks in the pulse area spectrum. See section ?? for examples.
 373 MAPMs on the other hand posses larger gain fluctuations, which is due to their structure. These
 374 make Silicon Photomultipliers an interesting candidate in astrophysics experiments for both,
 375 space- and ground-based telescopes (like IACTs). However SiPMs also posses drawbacks, one
 376 of which is their temperature dependence through their gain and Dark Count Rate. Another
 377 source of worry is their Optical Cross Talk (OCT), although manufacturers advance to reduce
 378 this source of noise.

379 Advantages:

- | | |
|--|---|
| 380 1. Sturdiness | 387 5. No need for HV as in PMTs |
| 381 2. May be exposed to ambient light (obse ³⁸⁸ | 388 6. High Photon detection efficiency |
| 382 vation during bright moonlight periods ³⁸⁹ | 389 7. Insensitivity to magnetic fields |
| 383 possible) | 390 8. Being a fairly new technology it is |
| 384 3. Low power consumption ($\leq 50\mu\text{W}/\text{mm}^2$) | 391 steadily improved, meaning a new gen- |
| 385 4. Low operation voltage (typically ~ 20 ³⁹² | 392 eration of SiPMs every 5months |
| 386 100 Volts) | 393 9. Rapidly decreasing cost per mm^2 |

394 Drawbacks:

- 395 1. temperature dependence, gain and Dark Count Rate
 396 2. Noise through Optical Cross Talk

397
 398
 399 There is a multitude of desired attributes of SiPMs by CHEC, and CTA in general, among them
 400 is a high enough fill-factor (detector space versus dead space) to guarantee high Photon De-

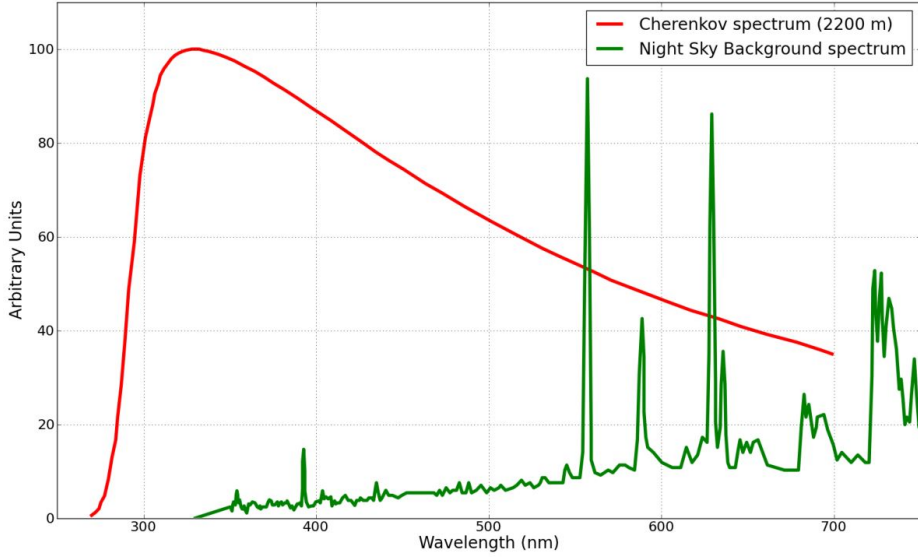


Figure 9: The spectrum of Cherenkov light observed from an extended air shower at 2200m asl. compared to the expected NSB measured in La Palma. Cut-off of the spectrum at wavelengths below ~ 300 nm due to atmospheric absorption. The emission peaks above ~ 550 nm in the NSB spectrum are mostly attributed to atomic oxygen, hydroxide and sodium in the atmosphere. Units on the y-axis are arbitrary because NSB and Cherenkov light vary by different parameters. There is a region between 550 and 650 nm, where the Cherenkov light spectrum and contributions from the NSB overlap. Image from [9]

401 tection Efficiency (PDE) 3.5. The PDE quantifies the absolute efficiency of any photon detector
 402 to absorb a photon and produce a measurable signal at its output. To achieve a high PDE in
 403 the 400 nm regime, the design moves to very thin implantation layers on the surface in order
 404 to minimize the absorption of shorter wavelength photons in insensitive areas fig(??). Different
 405 entry window coatings and avalanche structures (trenches etc.) explore the capable enhance-
 406 ments in the blue sensitive UV region.

407 The peak of the spectral response of the SiPM is desired to be around the spectral peak of the
 408 Cherenkov light at ~ 400 nm and at the same time, must have a fast enough drop to ensure
 409 less Night Sky Background (NSB) pick up (Figure(??)). The overall noise from thermal and
 410 correlated secondary effects, like cross-talk, of the SiPM must be sufficiently below the expected
 411 NSB rate at the location (usually around $\sim 20\text{-}80$ MHz[9]). It is common practise to compare
 412 those two characteristics directly to showcase the behavior of the PDE versus OCT. A point of
 413 low cross-talk, where the PDE is still at maximum is desired.

414 Another important characteristic is the temperature dependence of the gain. While the CHEC
 415 camera is observing, the preferred fluctuation of the gain is below 10%. The camera focal plane
 416 underlies temperature shifts during operation, which will be slightly countered by cooling the
 417 photosensing area. Despite that the focal plane will still be warming up, so a lower gain depen-
 418 dence on temperature is desired in order to minimise the gain fluctuations.

419 3.2 Gain of a Silicon Photomultiplier

421 The gain of a Silicon Photomultiplier measures the internal conversion of a photon incident into
422 a signal at the output. The amplification of the device is expressed as the average number of
423 charge carriers produced. There is no distinction whether the incident was caused by a single
424 original photon or a thermal electron. The gain (M) (eq 1) of a Silicon Photomultiplier results
425 from the deposited charge (Q) of the pulse generated from one cell when it detects one photon,
426 devided by the charge per electron (e). The charge deposited per event is proportional to the
427 cells capacitance (C) and the supplied over-voltage ($V_{bias} - V_{breakdown}$).[9] This results in the
428 gain (M) in units of total number of charge carriers, usually in the several 10^6 range.

$$M = \frac{Q}{e} \quad (1)$$
$$Q = C \times (V_{bias} - V_{breakdown})$$

429 Estimation can be done via the voltage mean of the 1 p.e. amplitude: (e.g. see Figure
430 (26)). For a better understanding, stating the gain in units of mV per photoelectron or $\frac{mV}{p.e.}$
431 is more suitable, as it gives a direct correlation between detected photoelectron and expected
432 voltage amplitude. Given the very narrow pulse shapes, using the average pulse amplitude and
433 extracting FWHM as a time measure of the total charge flowing during discharge and using the
434 formula (eq 2):

$$Q(p.e.) = C \times (V_{bias} - V_{breakdown}) \quad (2)$$
$$U(p.e.) = \frac{Q(p.e.)}{t(FWHM)} \times 50\text{ohm}$$

435 Resulting in the expected event charge flowing during capacitor discharge. Given the bias-
436 voltage and C as capacitance of one cell and the resistance (50ohm) of the quenching resistor, a
437 conversion factor and the average amplitude per photoelectron can be extracted.
438

439 The gain is obviously higher the larger the cell capacitance or the higher the bias-voltage
440 (eq 1) will be. But increasing the bias-voltage also increases dark counts and crosstalk. The
441 gain is also dependent on the temperature, mainly through the quenching resistor but also from
442 the silicon bulk itself, at a certain bias-voltage decreasing as temperature rises. The quen-
443 ching resistor is affected by a lowering of the electrical conductivity with rising temperature, in
444 accordance to the Wiedemann-Franz law, stating that the ratio of electrical and thermal con-
445 ductivity remains constant. The silicon bulk at rising temperatures underlies increased crystal
446 lattice movement. This impinges charge transport by increasing the probability that carriers
447 might impact on the lattice before the carrier energy has become large enough for continued

448 ionization. In order to counteract this, the electric field must be increased by increasing the sup-
449 plied bias-voltage so ionization is more likely. Doing this has drawbacks as discussed before. For
450 application as a photon detector, keeping the gain constant is an inevitable step, otherwise the
451 shifting gain leads to problems. To do that, either the bias-voltage need to be adjusted to match
452 ambient temperature, leading to problems with varying dark counts and crosstalk. Or the sur-
453 face temperature must be regulated to be kept constant. Although more challenging hardware
454 would be required, the latter option has obvious advantages, keeping dark counts and crosstalk
455 and more important the gain constant by simply regulating the surface temperature.

456 Taking into account equation 1, it appears that the breakdown-voltage can be estimated from
457 the zero-crossing of a linear extrapolation of the gain at every bias-voltage per temperature. By
458 doing this a linear breakdown-voltage dependence of the temperature can be observed. See
459 appendix E

460 When parametrized over over-voltage, the gain is essentially temperature independent.
461 For gain measurements see section 6.

462 3.3 Thermally induced dark counts

464 Inside the Silicon Photomultipliers depleted region a dark pulse originates from thermal exci-
465 tation of an electron to the conduction band. Without an event photon present to trigger the
466 avalanche, it is still indistinguishable from a photoelectron pulse. These thermally generated
467 carriers are observed along with the signal from a real photoelectron, presenting an irreducible
468 source of noise. The number of dark pulses observed is referred to as dark counts and the number
469 per second as the dark count rate. For applications that need to operate in an environment with
470 low noise, those dark counts are a concern. In IACT application of SiPMs however, this is only
471 a minor problem, since IACTs operate in a naturally noisy environment. Even though sky dark-
472 ness is one of the prime criteria of the proposed site selections for CTA, the surrounding NSB at
473 the most darkest side in Chile will still exceed any random noise in the detector. The pollution
474 of those NSB photons is unavoidable noise and will essentially limit the low energy resolution
475 of the telescope to the NSB rate. As long as any random noise, being dark counts or other, is
476 significantly below the NSB rate, it will not affect the telescopes performance.

477 Telescope performance simulations of the Schwarzschild-Couder MST of CTA at the site of
478 Chilc showed a rate of $\sim 20 - 80$ MHz per pixel for one of the older SiPM iterations from
479 Hamamatsu.[9] This is purely for NSB photons and pixels with a size of 6×6 mm², the cov-
480 ered range originates from differences in illumination level of the night sky by galactic- and
481 extragalactic-fields.

482 3.4 Avalanche-induced secondary effects

484 An avalanche originating from the primary cell can sometimes, either directly or by reflection,
485 propagate outside the cell and trigger an avalanche almost simultaneously in a secondary cell.

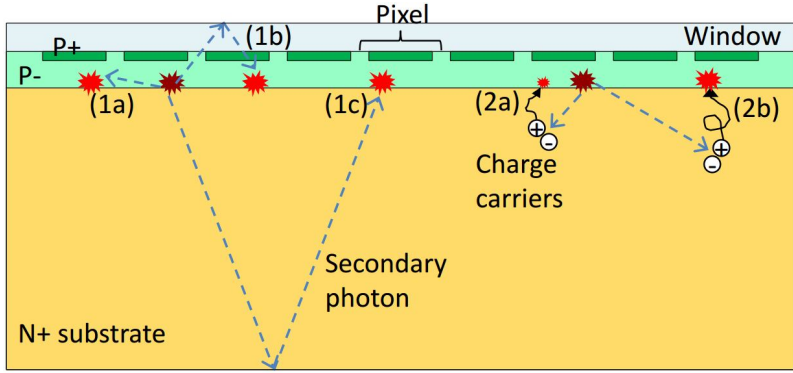


Figure 10: Secondary effects (bright red) caused by primary avalanches (dark red) in a Silicon Photomultiplier. In this paper a single pixel, in this figure, is referred to as a cell (see 3). Everything labeled under 1 is associated with prompt cross-talk, afterpulsing labeled as 2a, and delayed cross-talk labeled as 2b. Image adapted from [13]

486 This will, unless accounted for, degrade the Silicon Photomultipliers photon counting resolution,
 487 since the signal will be a merge of cross-talk cells and real incident cells. This effect is
 488 referred to as the Optical Cross Talk, since it is conveyed via secondary photons generated in
 489 the primary avalanche. Afterpulsing also falls under this category, with the main difference to
 490 cross-talk being that the carrier triggers a secondary avalanche in the primary cell, basically gen-
 491 erating a parasitic pulse inside the previously fired cell. Contained in a single cell, afterpulsing
 492 increases the measured charge registered for an incident photon. The difference in arrival time
 493 of the secondary avalanche distinguishes different components comprising the cross-talk and
 494 afterpulsing. Those secondary avalanches can again emit photons, that can trigger secondary
 495 avalanches themselves, leading to high amplitudes, even in dark conditions. Cross-talk is de-
 496 pendent on the ability of the secondary photons to reach a neighboring cell. This means, that
 497 an increase in cell-size and therefore cell-area should directly correlate with the Optical Cross
 498 Talk of a pixel. The OCT dependency on the cellsize was tested and can be found in section C.
 499 Figure (10) shows different physical processes causing secondary effects in Silicon Photomulti-
 500 pliers based on their delay time. Cause of the delay time is the dependence on the penetration
 501 depth of the incident photon, or the region the dark count generated, and the diffusion time
 502 inside the substrate. At long delay times of up to 70ns afterpulsing and cross-talk are not
 503 distinguishable.[13] The prompt Optical Cross Talk happens basically simultaneous to the pri-
 504 mary avalanche, since it is unaffected by the primary cells recovery time and is labeled 1 in
 505 Figure (10). It is either triggered by the secondary photon directly (1a) reaching the neigh-
 506 boring cell, or after first reflecting on the surface layer (1b) or the bottom surface (1c). If the
 507 cross-talk avalanche delay time is shorter than the detection resolution, the difference in signal
 508 between an Optical Cross Talk event or an incident photon being detected, is not observable.
 509 Time delayed Optical Cross Talk is caused by a carrier generated in the non-depleted substrate
 510 diffusing to a neighboring cell and triggering an avalanche in the depleted region (2b). If the

511 carrier stays in the primary cell, the triggered avalanche is labeled afterpulsing (2a) and will
512 have a lower amplitude, due to the cell not being recovered yet. The delay time is influenced
513 by how deep the carriers are being trapped in the substrate, the time they need to diffuse to the
514 surface, and also distinguished by traps with different lifetimes.

515 This is very important in IACT performance, since this effect gives random NSB and dark count
516 photons the ability to rise to larger amplitudes. The consequent need to raise the trigger thresh-
517 old to counteract the resulting rising accidental-triggerate has a negative impact on the low
518 energy resolution of the telescope.

519

520 Parametrized with over-voltage, the secondary avalanche effects are temperature indepen-
521 dent, for OCT measurements see section 6.

522 3.5 Photon Detection Efficiency

$$PDE = \frac{N_{\text{detected photons}}}{N_{\text{total photons}}} \quad (3)$$

524 The Photon Detection Efficiency is the probability of a detector to absorb an incoming pho-
525 ton and produce a measurable signal at its output, and depends on a number of factors. First
526 the photon must enter the depleted region via transmission through the surface of bare sili-
527 con, which has a reflectivity of 30%. However, the transmission probability can be improved
528 by coating the surface with a substrate with adequate thickness and a refraction index between
529 air $\eta_{\text{air}} = 1$. and silicon $\eta_{\text{silicon}} = 3.4$. Devices presented in this paper are coated with epoxy,
530 a silicon resin and glass. The coating also has the added benefit of insulating and protecting
531 the cells against environmental influence. A possible negative effect of coating is an increase in
532 prompt cross-talk and a larger dependency of the overall cross-talk on the cellsize. The second
533 factor is quantum efficiency, describing how susceptible the depleted region is to photons ex-
534 citing electrons from the valence band to the conduction band. This is sometimes referred to as
535 spectral response of a detector to reflect the wavelength dependence of a detector and makes
536 the PDE wavelength dependent. The over-voltage dependency of the PDE is conveyed by the
537 third factor, the avalanche probability. It depends on the electric field present, and thus on the
538 applied over-voltage. The last factor is the fill-factor: the more the surface area of the detector
539 is covered with active-area cells and the less dead-area exists between cells the higher the fill-
540 factor is.

541 The Photon Detection Efficiency is commonly measured by illumination of the pixel and a cali-
542 brated reference photodiode with a flashing light source, and determining the average number
543 of photons hitting the photosensor during a light pulse.

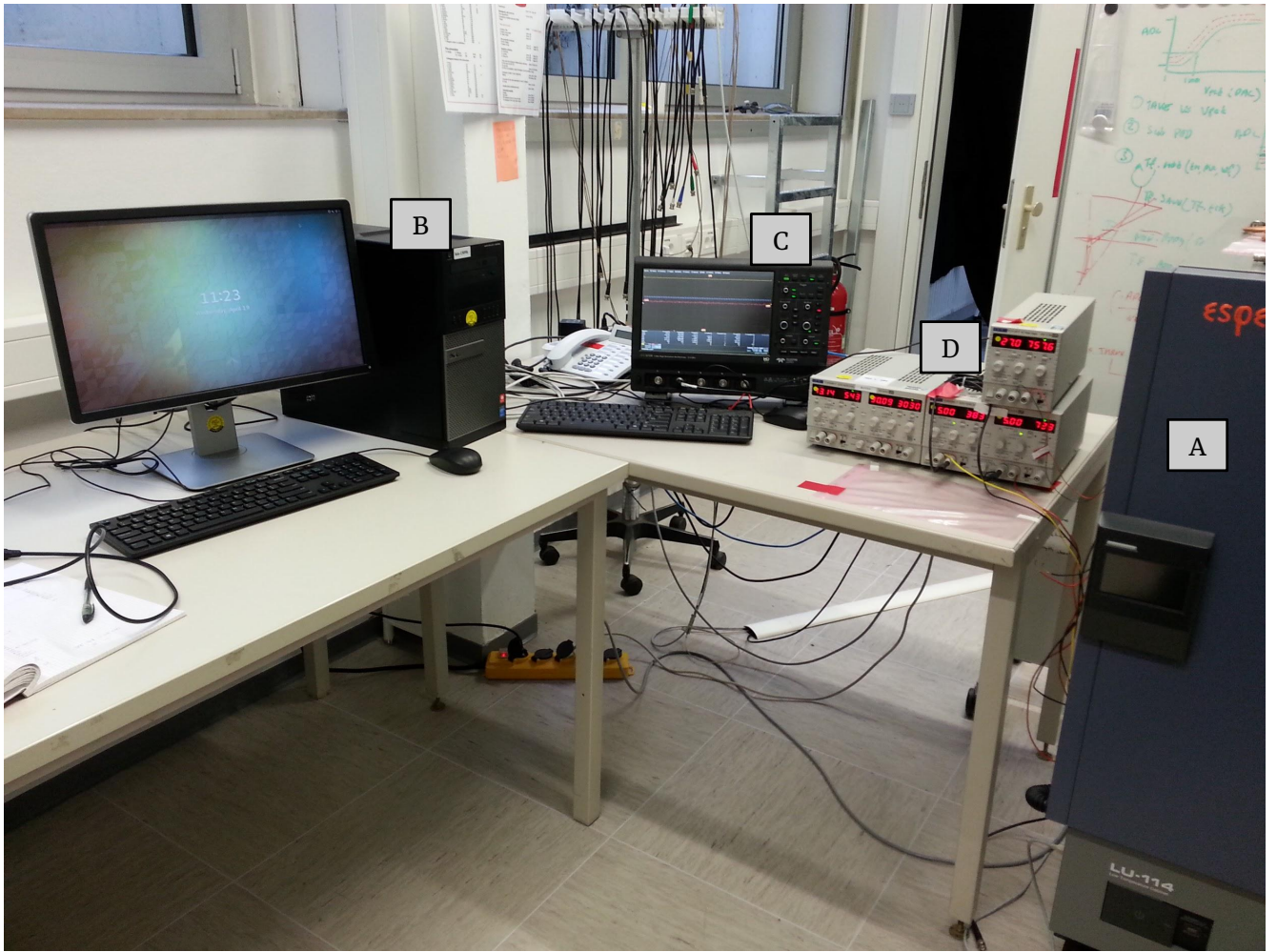


Figure 11: Outside view of the teststand with the ESPEC LU-114 thermal chamber (A), the Lab-PC (B), the Lecroy HD6104 oscilloscope (C) and the TTi power supplies (D).

544 4 Experimental Setup

545 The experimental setup in general is designed to house a variety of SiPM devices. Over the
 546 course of this paper, 5 different types of SiPMs were mounted on the setup and evaluated. It
 547 involves a thermal chamber Figure(59)(A) for temperature regulation which proved light tight
 548 and thus also serves as a dark box, to prevent any stray light to reach the SiPMs surface. The
 549 thermal chamber in question is a LU-114 constant climate cabinet from ESPEC with a pro-
 550 grammable interface for remote control. The chamber is able to raise and lower the inside
 551 temperature with a $\pm 0.5^\circ\text{C}$ accuracy, direct measurements of the SiPMs surface with a tempera-
 552 ture probe confirmed this. In the absence of light tests, heating of the SiPM surface through the
 553 dark current proved no concern.

555

556

557 Depending if the SiPM Figure(59)(A1) in testing is pre-manufactured on a test-array or sup-

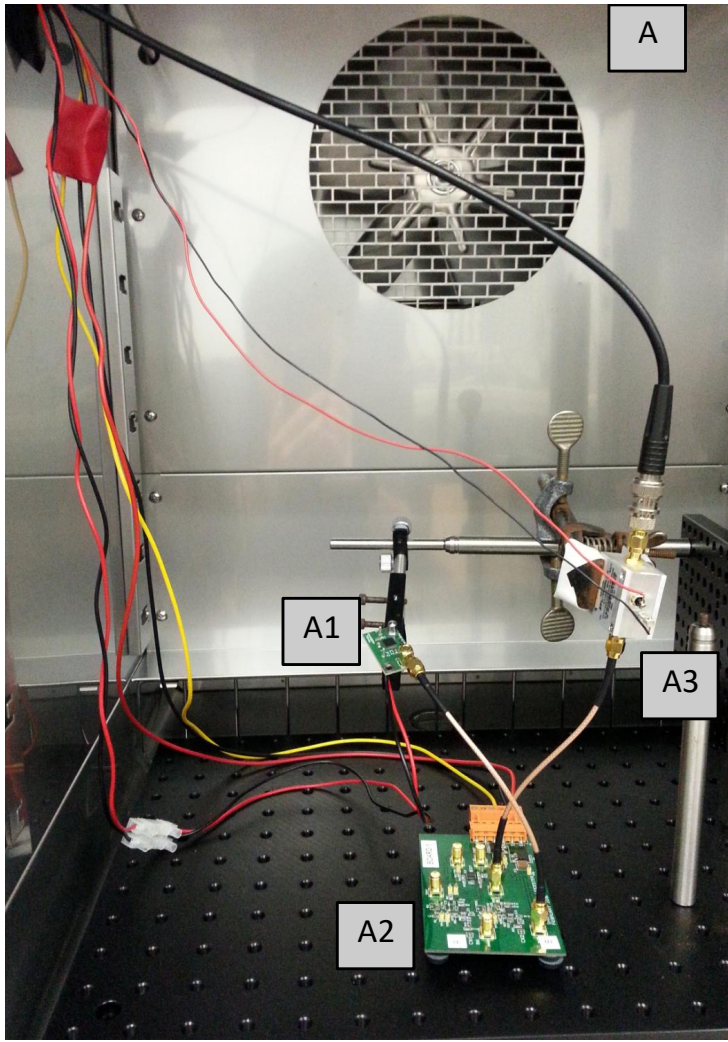


Figure 12: Inside view of the thermal chamber (A), with the SiPM (A1), the shaping electronics (A2) and the MiniCircuits PreAMP (A3). Signal throughput in the top left corner.

plied as a standalone chip, it is either mounted directly on a mechanical arm inside the chamber in the former case, or in the latter the mechanical arm supports a specifically designed PCB connecting to the device. Via the mount, bias-voltage is supplied and signal is transferred to the shaper Figure(59)(A2). In some cases the output signals amplitude is too low to trigger the oscilloscope, therefore amplification is needed. I used an amplifier from MiniCircuits Figure(59)(A3) supplied with different voltages depending on the tested device to amplify the shaped signal.

564

Data acquisition in the Laboratory is realized by a Lab-PC Figure(59)(B), that forms the central control station for multiple pieces of equipment. It is connected to the oscilloscope Figure(59)(C), which records the waveforms of the device in testing, and then sends the data back to the PC via ethernet. The oscilloscope is a Lecroy HDO6104 1GHz HS Oscilloscope capable of 2.5 GS/s.

570

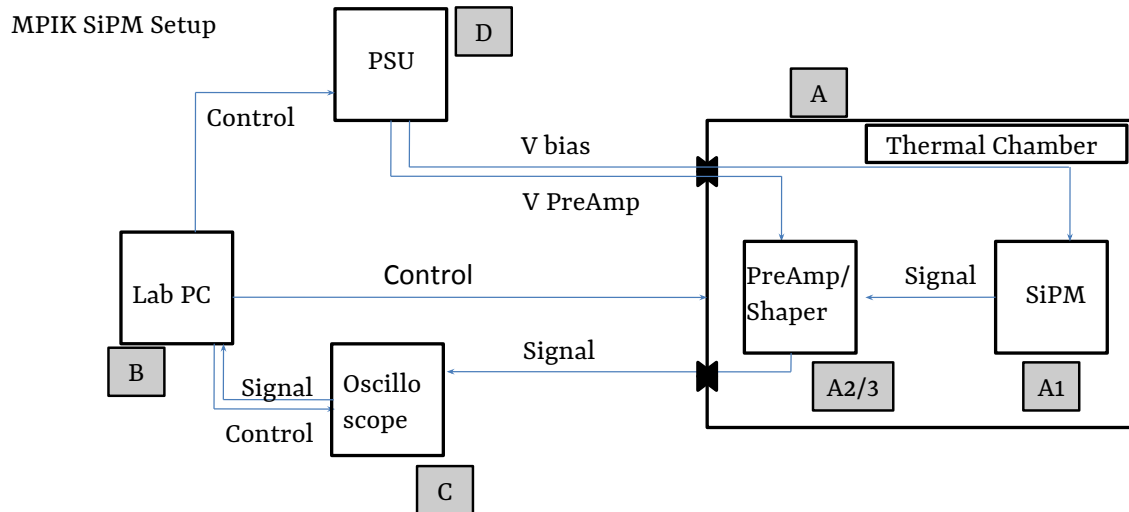


Figure 13: Experimental setup scheme, Annotations see text

571 The power supplies Figure(59)(D) control the bias-voltage of the Silicon Photomultipliers,
 572 ramping of the bias-voltage is controled by the PC. Lastly the thermal chamber is connected
 573 to the Lab-PC, where the data acquisition script controls the temperature, and continuously
 574 rechecks it during temperature ramps. Signal transfer from the shaper to the oscilloscope is via
 575 a throughput on the side. All equipment is connected via ethernet, plugged into a common hub,
 576 to form a local network. While the temperature of the thermal chamber is ramping from the
 577 previous to the next set-point, the data is send to the Lab-PC.

578

579

580 Temperature regulation is an issue in the teststand, as there is no way of controlling the SiPMs
 581 surface temperature. In dark conditions however, without conducting illumination tests, the
 582 shift in temperature on the SiPMs surface is only minimal. See section E for the breakdown-
 583 voltage dependence on temperature. Checking the surface temperature of all devices with a
 584 temperature probe during testing showed minimal rising temperatures. So the influence of the
 585 temperature on the breakdown-voltage is only of minor concern. However, once illumination
 586 tests begin, the rising temperature on the SiPMs surface will no longer be negligible and the
 587 temperature must be regulated, either by cooling of the surface or including the temparature
 588 parameter.

589

590 There is also the issue of the saturation of the input of the oscilloscope making the higher
 591 over-voltage range difficult to reach, due to potential multi p.e. pulses being amplified and
 592 reaching the input. **This is possible because of the difference in amplitude between a 1 p.e. and**
a multi p.e. event and the electronic noise, forcing a high resolution of the amplitude in the
 593 **oscilloscope. A possible solution could be a filter set to attenuate such pulses to a given voltage**

595 so data is not lost. Lowering the electronics noise would have the same effect on the lower
596 over-voltage range.

597

598

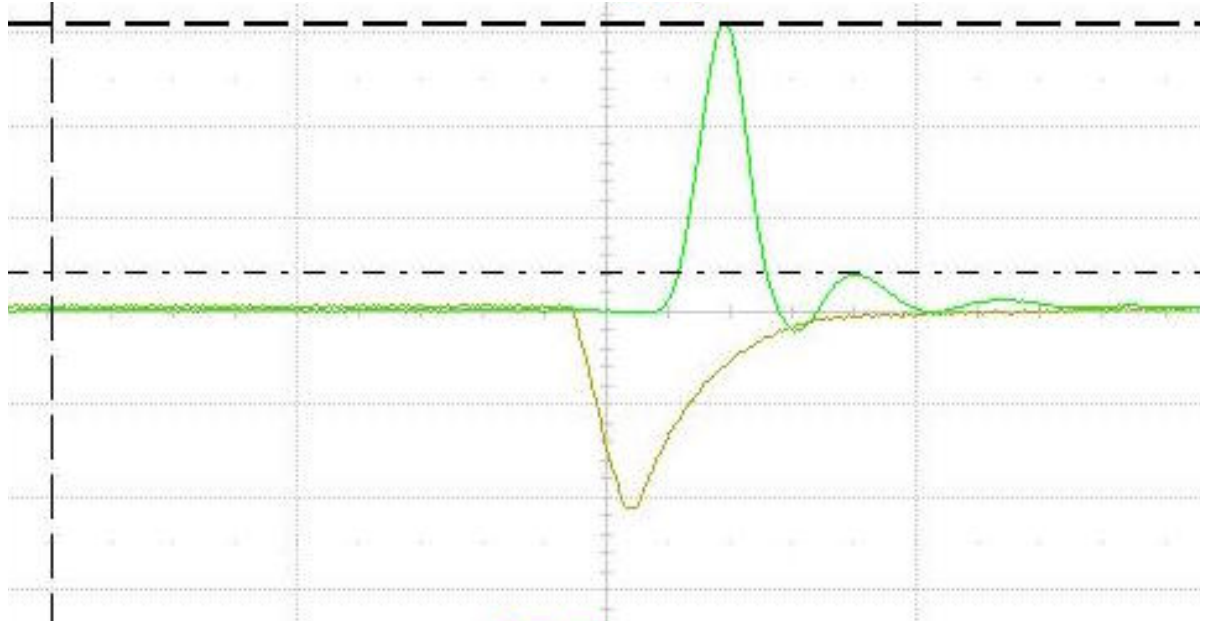


Figure 14: The shaped and unshaped pulse from a pulse generator emulating the output of the front-end buffer of the CHEC-S SiPM. The unshaped pulse in yellow and negative, due to the buffer-output. The shaped pulse now flipped through the electronics in green. Zoomed, Image credit [20]

599 The shaper consists of two stages, the main
 600 components are an Op-Amp amplifier serving
 601 as an input buffer followed by a zero pole
 602 cancelation circuit for pulse shaping and is
 603 commonly used in photon-counting applica-
 604 tions. A zero pole cancelation circuit is ba-
 605 sically a RC circuit eq(4) (C_Z, R_0) supressing
 606 the high frequencys to narrow the pulses from
 607 the usual ~ 50 ns to ~ 10 ns, using a high-pass
 608 filter with a tunable time constant, through
 609 f_C which gives control over the frequency re-
 610 sponse of the circuit.[21]

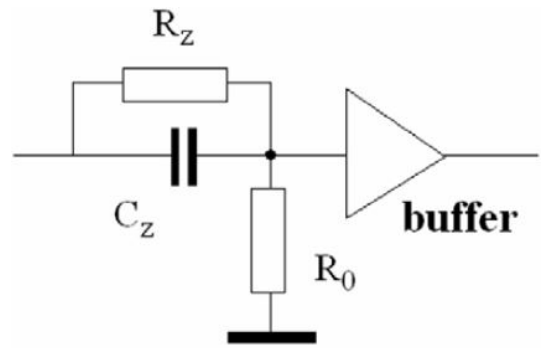


Figure 15: A Zero Pole cancelation circuit com-
 monly used in photon counting applica-
 tions. Taken from [21]

$$R_0 \times C_Z = 1/(2\pi \times f_C) \quad (4)$$

611 In Figure 14, reference by Luigi Tibaldo [20], the shaped and unshaped pulse is shown,
 612 the negative amplitude (yellow) corresponds to the unshaped signal mimiced by a function
 613 generator to emulate the output of the front-end buffer of the CHEC-S SiPM, with a fall-time of

614 approximately 9 ns followed by the exponential rise with 90 % to 10 % in 23 ns. These tests
 615 correspond to an initial design of the shaper and do not correspond to the final setup.

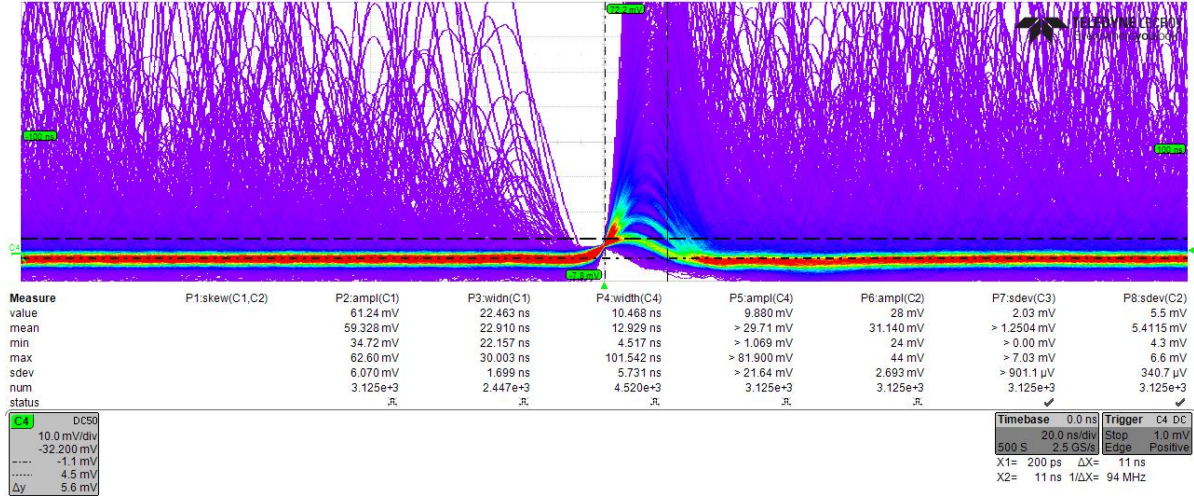


Figure 16: Persistence figure of the shaped pulse after adapting the electronics to a preferable pulse shape. In the center, a row of pulses with rising amplitudes is visible. These are the multiple N p.e. pulses, differing by ~ 5 mV. The purple area off-center is due to delayed cross-talk and after-pulsing. Image credit [20]

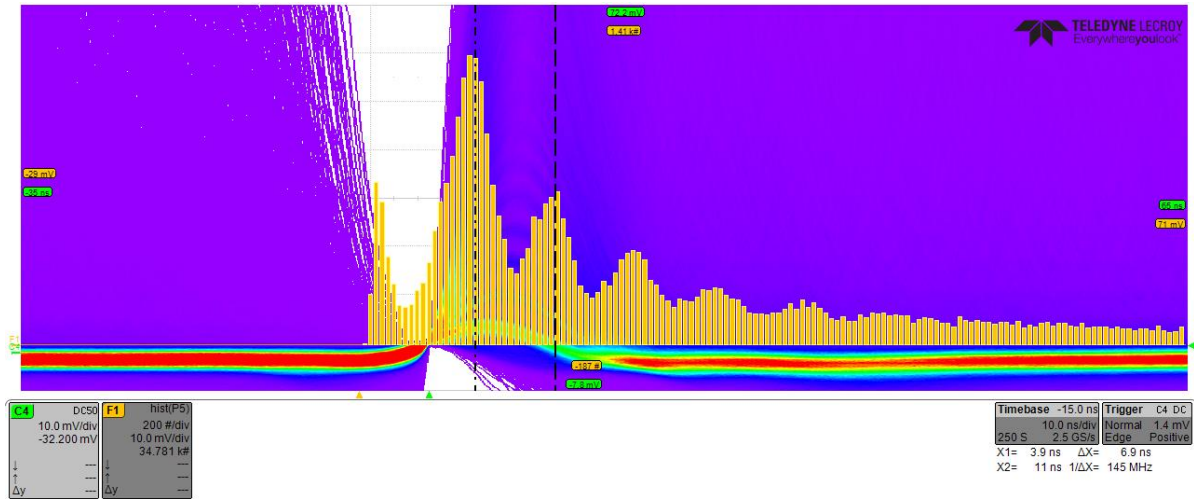


Figure 17: An oscilloscope based pulse height spectrum in the same scheme as the persistence figure fig(16). The distance between the peak maxima delivers an estimation of the gain of the SiPM at this bias-voltage. Image credit [20]

616 The shaper board contains tuneable capacitors (C9) and resistors (R20) (see schematic ap-
 617 pendix F), that can be tuned and optimized for ideal pulse layout. The green pulse in Figure
 618 14 shows the output after shaping, with a width of FWHM of 9 ns. The amplification between
 619 input and output is approximately 6-7. The output pulse has some ringing after the main pulse,
 620 the first afterpulse has a 12 % amplitude relative to the main pulse. For the complete unzoomed

621 figure, see appendix F.

622

623 After tweaking the tunable electronics on the shaper to a preferable pulse shape, clear single p.e.
624 peaks are visible in a persistence plot. fig(16). The peaks have an amplitude of ~ 5 mV/p.e.,
625 from this and from the following, a gain estimate for the peak finding threshold in the anal-
626 ysis can be made. With the same configuration a gain estimate at different bias-voltages of
627 the SiPM is possible through an on-oscilloscope pulse height spectrum fig(17). The distance in
628 peak maxima is a reference to the gain of the SiPM, in the case of Figure 17 close to ~ 5 mV/p.e. .

629

630 This chain of shaper modification is done for every SiPM from Hamamatsu Photonics K.K.
631 tested in this paper (4 in total) as they arrived as a single unmounted device, in need of
632 shaping and amplification. The device from SensL is premounted on a test array, preshaped
633 and only externally amplified.

634 5 Data Analysis

636 The analysis of the Silicon Photomultiplier waveforms is done exclusively in python following
637 the sequence:

638

- 639 1. data conversion
640 2. pedestal subtraction
641 3. peak detection
642 4. gain extraction
643 5. calculation

644 The waveform data, after being transferred to a separate PC, is analyzed offline. The goal is
645 to extract event-data from the waveforms in order to produce pulse-area spectra for every bias-
646 voltage at every temperature. To that end, the pedestal of the electronic noise must be found and
647 subtracted from the data. After that, event-pulses are detected and integrated. This generates
648 a list of pulse-areas, which is in turn used to fill a pulse-area histogram. To this pulse-area
649 histogram, a model is fitted from which the gain can be extracted. Due to the linear behavior
650 of the gain with rising bias-voltage, a regression line is fitted, from which the Dark Count Rate
651 and the Optical Cross Talk are calculated using the original pulse-area histogram.

652 5.1 Tracefile Conversion

654 The oscilloscope produces the waveform data in its intrinsic data format, called a trace with
655 the data suffix trc in binary. A trace file contains a header and two binary lists, an amplitude
656 based on the oscilloscope's voltage-range and offset, and a list of the same length containing the
657 associated event-time, based on the time-range and horizontal offset. The first step is therefore
658 a conversion of the amplitude and associated event-time of all segments of a waveform trace
659 file into two lists of floats.

660 5.2 Pedestal Subtraction

662 A single waveform from the oscilloscope is
663 anticipated to be uncentered fig(18)(grey), it
664 will be slightly above or below zero, depending
665 on the device setup (some devices pro-
666 duce inverted signals). The signal is mixed
667 with electronic noise when it is observed
668 and forms a pedestal, shifting the mean of
669 the waveform from its original position to
670 zero. Pedestal subtraction removes this av-
671 erage noise.

672 The first step of the process is reading in the
673 uncentered waveform fig(18)(grey) and cal-
674 culating an initial mean(mean0), expected to
675 be slightly higher than the actual mean of the
676 noise, due to the presence of event-pulses.
677 The waveform is then shifted to about zero,
678 by subtracting the mean0. A second mean of the now nearly centered waveform is taken
679 (mean1). Now a new, same-sized array is formed and filled with the data from the wave-
680 form that is smaller than mean1, this represents the negative part of the noise. The data larger
681 than mean1, the positive noise, is also filled into the array, but is negative-signed. This cre-
682 ates an array of the waveform centered around zero and, above the mean1, folded towards the
683 negative. It proved reliably, that calculating the root-mean-square of this helper-array is a solid
684 possibility of stripping the waveform of event-peaks. Taking the root-mean-square with a factor
685 3 of the helper-array, a cut is now applied to the waveform on both, the positive and negative
686 side. In that fashion, the remnant is the waveform between the positive and the negative root-
687 mean-square and is now called a peakless-signal, representing the noise of the waveform.
688 Pedestal subtraction is done by calculating the mean of this peakless signal and subtracting
689 it from the waveform. After that, the peakless signal is also smoothed by convolving it with
690 a wide-windowed gaussian and subtracted from the waveform to eliminate any slow moving
691 noise, the resulting waveform is called "Filtered Signal 1" fig(18)(blue).

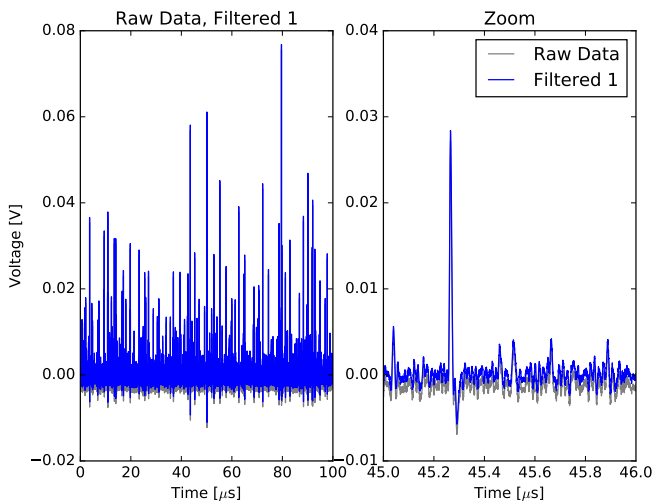


Figure 18: Raw, real data from a HPK SiPM in grey, in blue the pedestal subtracted and smoothed "Filtered Signal 1"

5.3 Peak Detection

Peak detection exploits the fact, that the first derivative of an event-peak will cross zero into the negative at the time of the peak maximum. The presence of random noise in the signal however will lead to many false detections. Therefore, before the detection of the event-peaks, the waveform fig(19)(grey) is smoothed with a narrow-window gaussian with a width of about the FWHM of the devices characteristic event-pulse, in order to attenuate non-event peaks fig(19)(blue). After the first derivative of the signal is calculated, which in python is a fast process if using arrays, a number of parameters decide the validity of the detected peaks. Most important parameters are a certain predetermined minimum amplitude, called the amplitude threshold or: minimum peak height. This is determined from initial examination of pulses on the oscilloscope and entered as a parameter to the analysis chain, but could later be calculated based on the noise level. The second important parameter defining validity is the minimum peak distance, which defines how close two events can occur after another. The value is determined by the FWHM of the device in testing, which is expected to be sensible enough to resolve two events happening close after another. The peak detection algorithm can not distinguish between instantaneous and delayed Optical Cross Talk, but nonetheless, due to the fact, that the signal data is taken over many micro-seconds, all events are detected, independent of their source. On the other hand, this also means, that it is possible for two events to happen at the same time, for example a real photoelectron-event coinciding with delayed Optical Cross Talk or two simultaneous dark events being misinterpreted as one dark event + its prompt cross-talk. This can not be distinguished and will lead to a slight shift of the amplitude, due to the mostly lower amplitude of afterpulsing and cross-talk events.

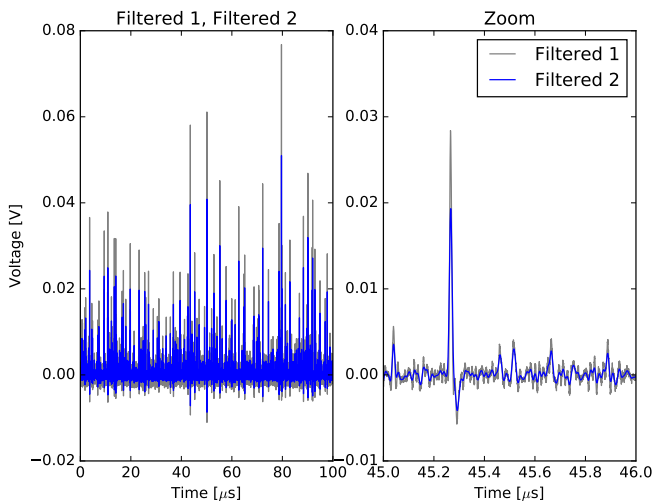


Figure 19: "Filtered Signal 1" in grey before smoothing with a narrow gaussian to generate "Filtered Signal 2" in blue, which is used for peak finding.

5.4 Gain Extraction

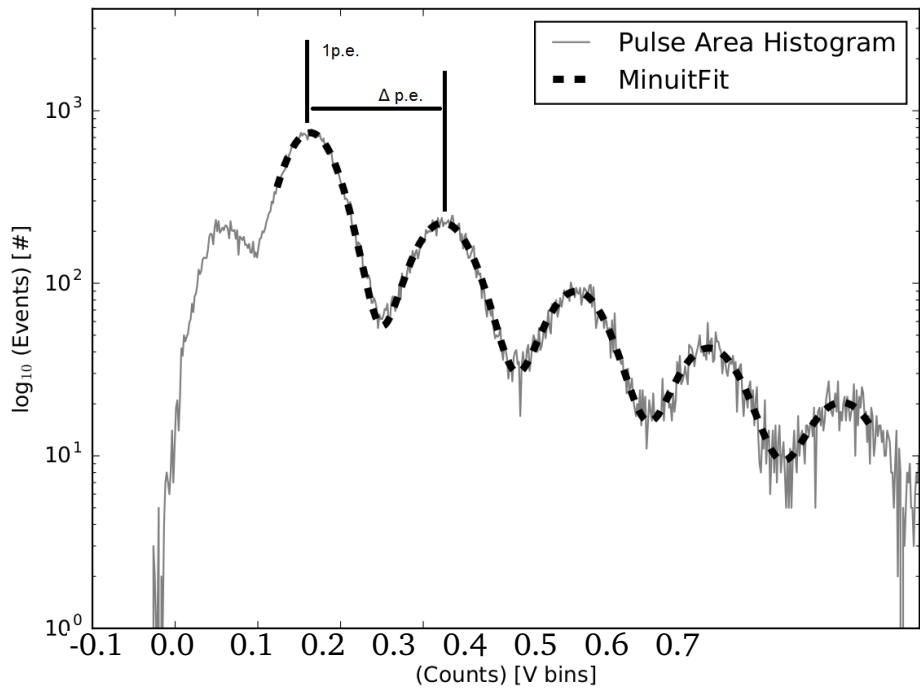


Figure 20: Pulse Area Histogram of a HPK S12642 with 1p.e. and Δ p.e. positions. Multi gaussian fitted function eq(5) as black dashed line.

726 The detected peaks are integrated with a window extending symmetricaly from the peak
 727 maximum, the width is chosen as slightly wider than the peaks FWHM. The generated list
 728 of peak areas is generating a peak area histogram (see section ??). The amplitude, position
 729 and sigma of the first p.e. peak is calculated and fitted with a single gaussian using pythons
 730 scipy curvefit, the fitted parameters serve as a first guess. After the first guess parameters are
 731 determined, the histogram is fitted with a function of multiple gaussians eq(5) using iMinuit
 732 in python, seen in Figure (20). To determine the number of gaussians to fit, another function
 733 checks the viability of each N p.e. peak, among the checked parameters is the ratio in height
 734 to the 1 p.e. peak and the amplitude of the checked Nth p.e. peak in the histogramm. The fit
 735 function $F(x)$ is a function of multiple gaussians with equal spacing eq(5). N is the multiplicity
 736 of the funciton or range the fit function is to be applied. A is the Amplitude of the Nth p.e. peak
 737 with σ , \bar{x} is the x-position of the 1 p.e. peak, Δx is the p.e. spacing distance.

$$F(x) = (N \times \left[A \times e^{\frac{-(x-(\bar{x}+N \times \Delta x))^2}{2 \times \sigma^2}} \right]) \quad (5)$$

738 Two parameters are extracted from the fit to the peak area histogram. The first \bar{x} , the posi-
 739 tion of the 1p.e. peak is the position of the maximum of the first peak in the histogram, and the

740 position of corresponding multiple p.e. events should be integral factors of the 1p.e. position.
741 This proved to not be the case for some devices, the suspected source of this error is a pedestal
742 generated during the peak integration. For a more detailed study of the effect of the integration
743 window see section 5.6.

744

745 A second parameter is extracted from
746 the peak area histogram to deal with this
747 problem, which is the distance between N
748 p.e. peak maxima of the histogram, la-
749 beled Δ p.e. . This distance defines
750 the gain, as it gives a measure of the
751 difference of the generated signal of a
752 1p.e. signal and a 2p.e. signal. The
753 apparent pedestal of the pulse area his-
754 togram makes extraction of the two par-
755 ameters necessary in order to calculate the
756 Dark Count Rate and the Optical Cross
757 Talk.

758

759 The gain of a Silicon Photomultiplier has
760 a linear dependence of the supplied bias-
761 voltage. Given that the bias-voltage range is
762 deliberately chosen such that the over-voltage ranges from about 1V growing upwards, the
763 range of linearity only starts at around the point of operation given by the manufacturer of the
764 device. At the higher end of the bias-voltage range the behaviour usually starts to divert from the
765 linearity. In order to get an estimation of the gain over a large range, both previously extracted
766 parameters, the 1p.e. peak and the distance Δ p.e. are fitted with a linear regression line. The fit
767 assumes linearity utilizing weighted least squares inherited from pythons statsmodels package.
768 For the fit, the data, where more than 2 gaussians are fitted to the peak area histogram has a
769 stronger weight.

770

771 Plotting both extracted parameters, as well as their respective regression lines versus bias-
772 voltage, as in Figure (21), shows the difference between the two parameters. Comparing
773 the manufacturer supplied breakdown-voltage from the datasheet for all devices showed, that
774 the zero-crossing of the 1p.e. regression line is more consistent with datasheet values, in con-
775 trast to the zero-crossing of Δ p.e. , which lies slightly higher. The over-voltage, corresponding
776 to the set bias-voltage at any given temperature is calculated from this breakdown-voltage.

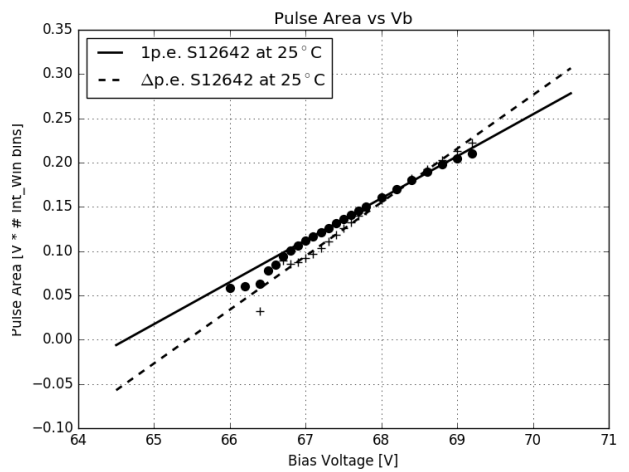


Figure 21: 1p.e. position and Δ p.e. extracted from the Pulse Area histogram at every bias-voltage for HPK S12642 with their respective regression lines.

777 Dark Count Rate and Optical Cross Talk are calculated utilizing 1p.e. position and Δ p.e.
778 derived from the regression line. Both values are applied, in the calculation, to the peak area
779 histogramm with the Dark Count Rate of a Silicon Photomultiplier being defined as all events
780 exceeding 0.5 p.e. in apmlitude $N_{events(\geq 0.5p.e.)}$ occuring over the experiment time $T_{experiment}$ 6.
781 Included in the measurement are thermally generated dark counts, as well as delayed cross-talk
782 and afterpulsing with only a minor contribution.

$$DCR = \frac{N_{events(\geq 0.5p.e.)}}{T_{experiment}} \quad (6)$$

783 The Optical Cross Talk of a Silicon Photomultiplier is defined as all events exceeding 1.5 p.e. in
784 apmlitude [$N_{events(\geq 1.5p.e.)}$] devided by all events exceeding 0.5 p.e. in amplitude [$N_{events(\geq 0.5p.e.)}$]
785 7. It scales with the number of photons produced inside an avalanche, as well as the probability
786 of these photons to trigger a neighboring cell

$$OCT = \frac{N_{events(\geq 1.5p.e.)}}{N_{events(\geq 0.5p.e.)}}. \quad (7)$$

787 **5.5 Analysis improvements**

789 For one, at higher DCR the multi hit coincidence of 2 1p.e. pulses rises and together with the
790 resolution of the waveforms this could lead to the OCT being calculated high (see section K).
791 Changing the determination of the threshold from being measured with an oscilloscope and
792 added as a parameter by hand, to being determined on a per-waveform basis before peak-
793 finding could improve the lower over-voltage resolution depending on electronic noise.
794 The source of the 'pedestal' in the pulse area spectra is suspected to originate from the pulse
795 integration, but this is not certain.

5.6 Data Challenges

5.6.1 The influence of the minimum peak distance

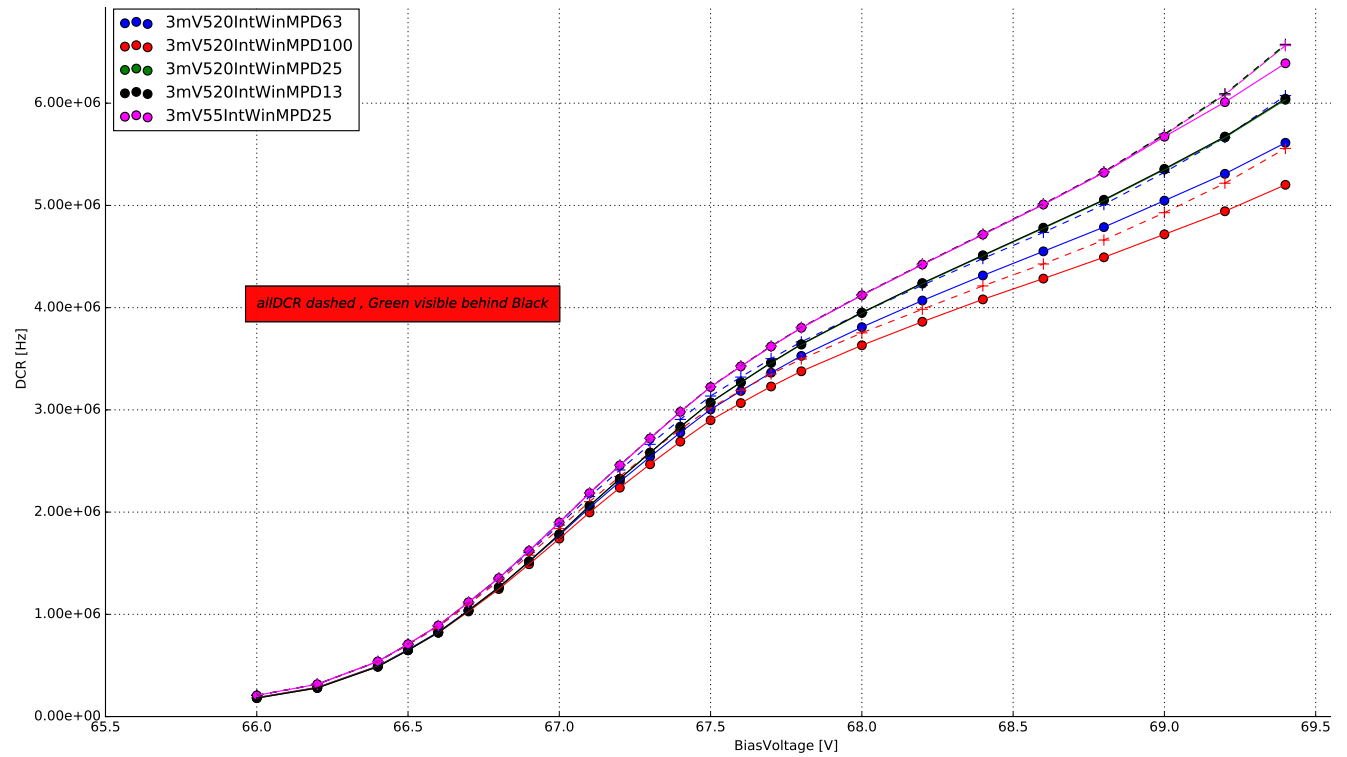


Figure 22: The difference between 4 minimum peak distance windows, in time-bins, during the peak detection. The dashed lines are the Dark Count Rates considering all recorded events, forming an upper limit. In pink, the effect of a different integration window is shown.

The influence of the minimum peak distance is shown in Figure (22). Based on their bin-width, four different windows are tested. With the oscilloscopes sampling rate of $2.5 \frac{GS}{s}$, the windows of 100, 63, 25 and 13 time-bins, correspond to 40, 25, 10, 5 ns windows respectively. With a event pulse FWHM of 10ns, setting the minimum peak distance to 100 bins, resulting in a 40ns window is visibly to large, as the algorithm will skip over valid data Figure (22)(red). After an event is detected, skipping over 40ns worth of data will result in errors of the Dark Count Rate, since the calculation uses the complete experiment time. Therefore a more reliable distance window must be chosen. The second window of 25ns was the next approach, originating from the length of the pulse-tail fig(22)(blue). This would lead to no detected events overlapping with the tail of one previously detected, resulting in a sharper pulse-area spectrum. Compared to a window of approximately the pulse FWHM, the previously discussed window would still lead to lost event-data. Since the sharpness of the pulse-area spectrum is already sufficient, a window around the pulse FWHM was chosen as reference for all measured de-

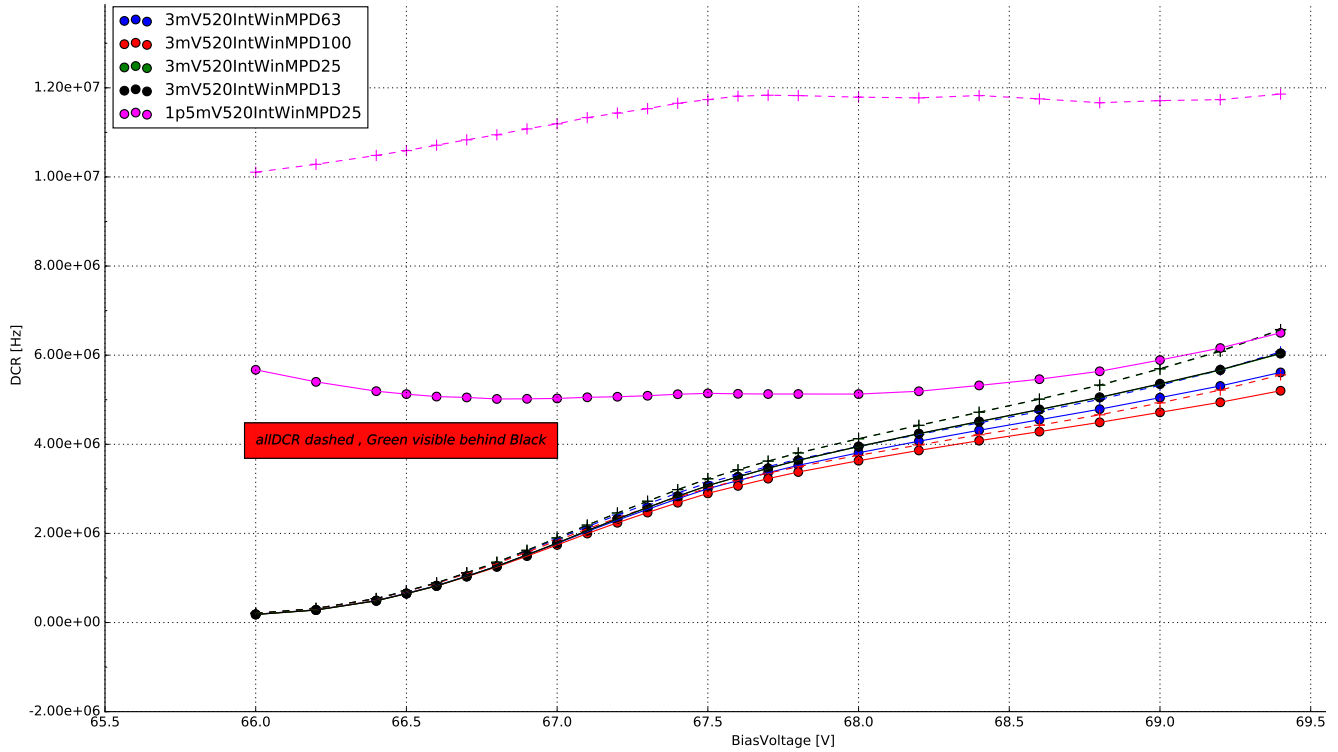


Figure 23: The difference between 4 minimum peak distance windows, in time-bins, during the peak detection. In pink, the effect of a lowered peak detection threshold is shown. The dashed lines are the Dark Count Rates considering all recorded events, forming an upper limit.

813 vices Figure (22)(green). Going lower than the pulse FWHM showed no improvement Figure
 814 (22)(black).

815 5.6.2 The influence of the integration window

816 Figure (22) also shows the influence of the size and shape of the integration window on the Dark
 817 Count Rate. The influence of the chosen integration window is most visible in their respective
 818 pulse area spectra. Choosing a narrow, symmetrical integration window of 5ns left and right of
 819 the peak maxima, the noise peak, or zero-peak, is much more prominent compared to the pulse
 820 area spectrum of a symmetrical 10 ns window. This leads to errors in the multi-gaus fitting
 821 step, or the fitting will fail altogether. An asymmetrical integration window of 5ns left, 20ns
 822 right, to capture the influence of the pulse-tail proved, at first, to be the best solution as their
 823 was no visible zero-peak present. The low amplitude pulses are averaged out by the extended
 824 integration window to the right of the pulse-maximum. The downside of the asymmetrical
 825 window is the shifting of the pulsle area spectrum and the fact, that the N p.e. peaks get
 826 blurred. The next step was widening the window on both sides. This proved the best solution,
 827 since there is no zero-peak visible and the N p.e. peaks are gaussian shaped. Please see the
 828 Appendix for the respective plots of pulse area spectra of the different windows ??.

830 5.6.3 The influence of the peak detection threshold

832 Choosing an adequate peak-finding threshold is a crucial step. Lowering of the threshold to
833 ~ 0.5 p.e. will cause the peak finding algorithm to misinterpret a lot of noise peaks as actual
834 dark incidents. This, of course, leads to errors in the gain extraction and even if a gain regression
835 line can be extracted, the resulting Dark Count Rates and Optical Cross Talk will be incorrect.
836 Figure (23), shows the effect a low peak finding threshold has on the Dark Count Rate.

6 Results

6.1 SiPM devices for CTA

Manufacturer	pixel size	cell size	coating	connection	specifics	pre-Amp
HPK S12642-1616PA-50 *CHEC-S SiPM	$3mm^2$	$50\mu m$	SR	TSV	no trenches	CHEC-S buffer
HPK LCT5 S13360-6050CS	$6mm^2$	$50\mu m$	SR	wire-bonds	trenches	MS 13V
HPK LCT5 6.975MM-SIL Single	$6.915mm^2$	$75\mu m$	SR	wire-bonds	trenches	MS 8V
HPK 6050HWB-LVR-LCT	$6mm^2$	$50\mu m$	SR	TSV	trenches	MS 13V
SensL FJ60035	$6mm^2$	$35\mu m$	glass	TSV	no trenches	MS 15V

Figure 24: List of SiPM devices which results are presented in this paper. *(SR: silicon resin , MS: MiniCircuits , TSV: through silicon via)

Silicon Photomultiplier devices for CTA are researched by many different groups, validating different characteristics. Besides the current SiPM for CHEC-S, newly developed prototypes offer a diverse range of pixel- and cellsizes. The majority of the devices are tested in Japan, at the University of Nagoya, conducting in depth analysis of the characteristics over a wide over-voltage range at one static temperature, mainly focusing on PDE and OCT, and their correlation. This correlation of OCT and PDE for all devices determines the candidate for CHEC-S, by comparing the highest PDE at the lowest possible OCT for each device. At MPIK, chosen candidate devices are examined regarding different characteristics and their temperature dependence and as to assist in the final decision by confirming results with a different analysis technique.

The chosen devices include the current CHEC-S device HPK S12642-1616PA-50, from Hamamatsu Photonics K.K., to be implemented in the first prototype camera. It is a previous generation SiPM, which was decided for use in 2014.(, due to the limited availability in high PDE devices at that time.) The manufacturer supplies a 16*16 channel premounted tile of $3mm^2$ pixels with a cell-size of $50\mu m$. To emulate the usage in a TARGET module, 4 $3mm^2$ pixels are electrically connected to form a $6mm^2$ superpixel. The tile is typically coated with epoxy resin, but due to specific requirements regarding the uniformity of the coating, it was replaced with a very thin layer of silicon resin equivalent to later prototypes. The CHEC-S devices electronic connection is realised via the new through-silicon-via (TSV) concept of running a connecting

860 solder through the silicon bulk, instead of wiring on the outside, greatly increasing the fill-factor,
861 but also including some disadvantageous sideeffects later shown.

862

863 Additional tested devices include the LCT5 generation from Hamamatsu Photonics K.K., so
864 called due to their low cross talk properties, namely the commercial available S13360-5050CS.
865 This device is the first to include physical trenches between the cells, effectively dividing the
866 cells optically and thus reducing prompt cross-talk probability.

867

868 The LCT5 generation also made two prototype devices available for testing at MPIK, the first,
869 HPK LCT5 6.975MM-SIL Single, is a larger iteration with a cellsize of $75\mu\text{m}$ and a pixelsize of
870 6.915mm^2 , leading to larger fill-factor, which would imply higher PDE, but also DCR and OCT.
871 Being from the LCT5 generation it also includes optical trenches. The second device available
872 is a LCT5 prototype designated 6050HWB-LVR-LCT , LVR meaning low-voltage-range, with the
873 same physical dimensions and properties as the S13360 device but incorporating TSV technology
874 and possibly other unknown deviations.

875

876 The final device is a commercially available test-array designated FJ60035 from SensL, pre-
877 mounted on a test-array by the manufacturer. It has the same pixel-size, but a much smaller
878 cell-size $35\mu\text{m}$ than the previous mentioned devices, and such a lower fill-factor, and a different
879 coating (glass).

880

881

882 The tests conducted in Nagoya contain many different iterations of the LCT5 generation with
883 varying pixel- and cell-sizes. For a full overview of the considered Silicon Photomultipliers,
884 please refer to section H.

6.2 Hamamatsu S12642-1616PA-50 50 μ m 3mm

887 The Silicon Photomultiplier by Hamamatsu Photonics designated
 888 S12642-1616PA-50 is a 3 mm by 3 mm device. The array uses
 889 the through-silicon-via technology, meaning there are no wire-
 890 bonds present, the electrical connection is realised through the
 891 silicon-body. The pixels are coated with a thin film of silicon
 892 resin, after the previously used epoxy resin proved not uniform
 893 enough. The electrical contact is realized through the through-
 894 silicon-via (TSV) technology, establishing connection through the
 895 silicon bulk, allowing a tighter fit of the cells, with minimal dead-
 896 space. One array consists of 256 pixels, four of which are electrically tied together to form a
 897 6mm by 6mm superpixel respectively. This practice is necessary for the pre-production camera
 898 CHEC-S, because the focal plane is mechanically designed to house 64 6mm² pixels, connected
 899 to the TARGET modules. Furthermore this is expected to have an influence on the results due
 900 to electrical crosstalk, but this is only of minor concern due to the following.

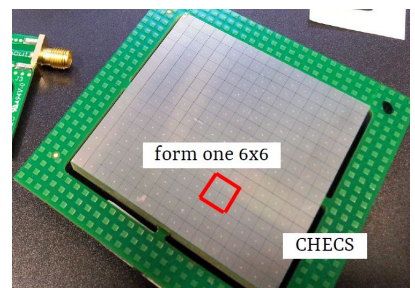


Figure 25: CHEC-S tile

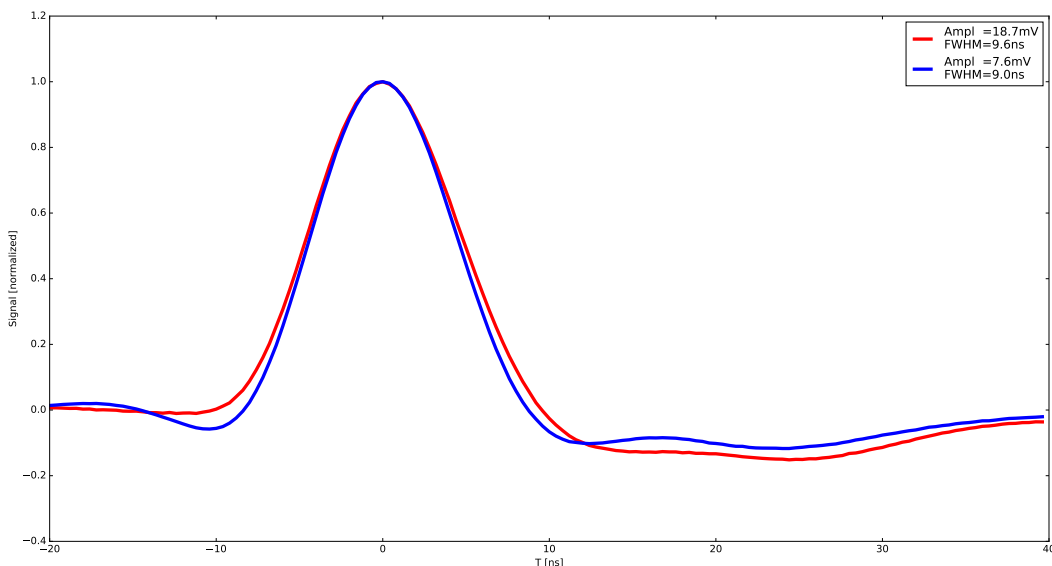


Figure 26: The average pulse shape of the 1photoelectron in blue and the 2photoelectron pulse in red of HPK S12642 at 25° C and 67.8V, which is around the proposed operating point. Both pulses are averaged over »1000 events and normalized to illustrate possible differences in pulseshape resulting from the utilized shaping electronics. Both pulses have a FWHM of around 10ns and are nearly free of ringing. The resulting average amplitude of the 1p.e. pulse is later used to calculate the Gain in [mV/p.e.] instead of [V*IntWin] by cross-referencing the 1p.e. amplitude at multiple bias-voltages.

901 The measurements of the CHEC-S tile concentrate on the array as an as-is device. This means
 902 their performance, influenced by external factors outside the actual Silicon Photomultipliers
 903 physics, are valid on the assumption, that the way the measurements were conducted is the way
 904 the photomultiplier will later be incorporated into the camera. On that ground, deviations of my
 905 results from the results of other groups and the manufacturer itself are expected. To clarify this
 906 further, for example, it is expected that the tests done at Hamamatsu Photonics where conducted
 907 on a single 3mm^2 pixel, not an array of 256 pixels, where 4 are tied together. Also divergence
 908 of shaping and amplification electronics between the groups will result in some differences.
 909 For this test, the CHEC-S tile is connected to the CHEC-S buffer, supplied with $\pm 4\text{V}$, where the
 910 signal is amplified. This signal in turn is then shaped via the CHEC-S shaper, developed by the
 911 University of Leicester, see section 4. This whole amplification and shaping chain is simulating
 912 later usage in the TARGET modules. Multiple measurements were conducted on different pixels
 913 of the CHEC-S tile, see section I.

914 6.2.1 Gain 915

916 As described in section 3.2, the average pulse shape fig(26) is used to convert the relative gain
 917 from the analysis procedure to an absolute gain in sensible units. This is necessary, because the
 918 analysis aims to use pulse-area rather than -height, which results in this relative gain being in
 919 units of $V \times \text{timebins}$, instead of voltage. In Figure (??) (left) the relative gain is shown, the
 920 right side shows the gain after conversion. A lower gain with increasing temperature is expected
 921 and described in detail in the chapter 3.2. In short, increased lattice movement due to higher
 922 temperature hinders photoelectron transport. The effects visible at extreme bias-voltages at both
 923 ends are partially analysis related. The gain of a SiPM is expected to be linear over bias-voltage
 924 at a constant temperature.

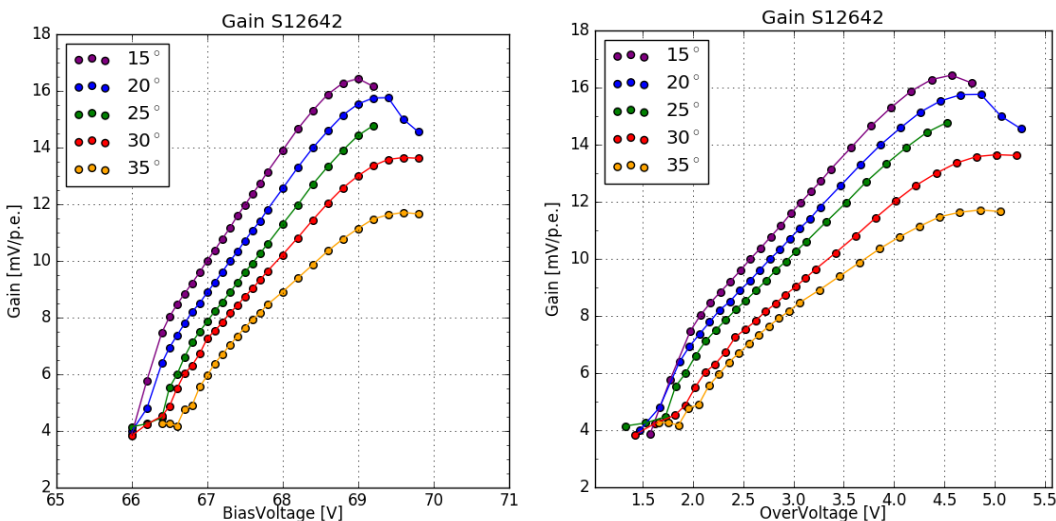


Figure 27: Gain of the HPK S12642 pixel, plotted against over-, bias-voltage and temperature.

In the lower regime at $V_b \sim 66.5V$ the gain is low compared to the noise, so the analysis struggles to pick up pulses. Depending on the determined peak-finding threshold, the analysis is suspected to interpret noise peaks as 1p.e. peaks at an increasing rate, the lower the overvoltage is. This is visible in the sudden break in linearity at $30^\circ C$ and $35^\circ C$, where the gain is almost in a plateau, due to this effect. The roll-over of the gain at the highest bias-voltages is in part a result of a voltage drop across the bias resistor occurring, because of high current flow through the SiPM. At higher temperatures, and therefore higher dark rates, the effect occurs at lower over-voltages. A second influence is caused again, by the noise at $V_{ov} 5V$, which is very high compared to the proposed point of operation at $V_{ov} 3V$. The same threshold is again counting the now increased noise peaks as 1p.e. peaks, but due to the abundance of 1p.e. pulses this results in an apparent lowering of the gain.

6.2.2 Dark Count Rate

The Dark Count Rate is expected to increase with temperature, which is the case for S12642 shown in Figure (28) and to follow a nearly linear progression, a sudden turn-up or turn-down of the Dark Count Rate would be analysis related. The turn-up at a certain point is visible in Figure (28), particularly for $15^\circ C$ (purple) and $20^\circ C$ (blue) respectively. At $15^\circ C$ and an over-voltage of $\sim 4V$, the Dark Count Rate starts to deviate from the previously linear behaviour. It starts to rise more rapid than before, the Optical Cross Talk at that point is also very high; exceeding 50% fig(29) (left). For the higher temperatures of $25^\circ C$ (green) and $30^\circ C$ (red) this critical point is not reached, so the effect is barely, if not at all visible. At

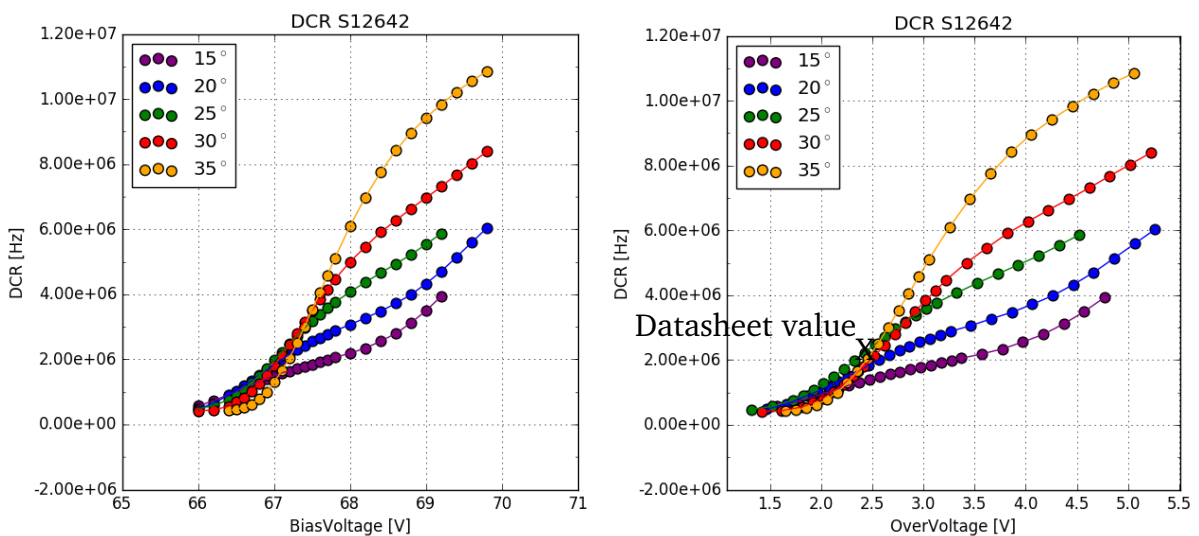


Figure 28: Dark Count Rate of the HPK S12642 pixel, plotted against over-, bias-voltage and temperature. Datasheet value at operation voltage = 2.4V and $25^\circ C$ measured by current

945

946 $35^\circ C$ (yellow), due to the high rate of 9-10 MHz, the analysis is not able to detect every

947 peak. At this point, heating of the Silicon Photomultipliers surface due to the high rate could
 948 also affect the Dark Count Rate through a slight shift of the temperature upwards, away from
 949 35°C . So that the Dark Count Rate declared at 35°C is in reality the rate at higher temperatures.

950

951 At the lower end of the bias-voltage range, a major part of the found 1p.e. pulses are sus-
 952 pected to be noise related. So the Dark Count Rate changing to a plateau is expected. This
 953 is also due to the fact, that the measurements are done with a fixed bias-voltage range. Due
 954 to the increase of the breakdown-voltage with rising temperature, part of the measured bias-
 955 voltage range corresponding to a very low over-voltage, attributes to this effect. In order to
 956 reliably measure beyond an overvoltage of 2.5V in the lower range, the noise would need to be
 957 improved.

958 6.2.3 Optical Cross Talk

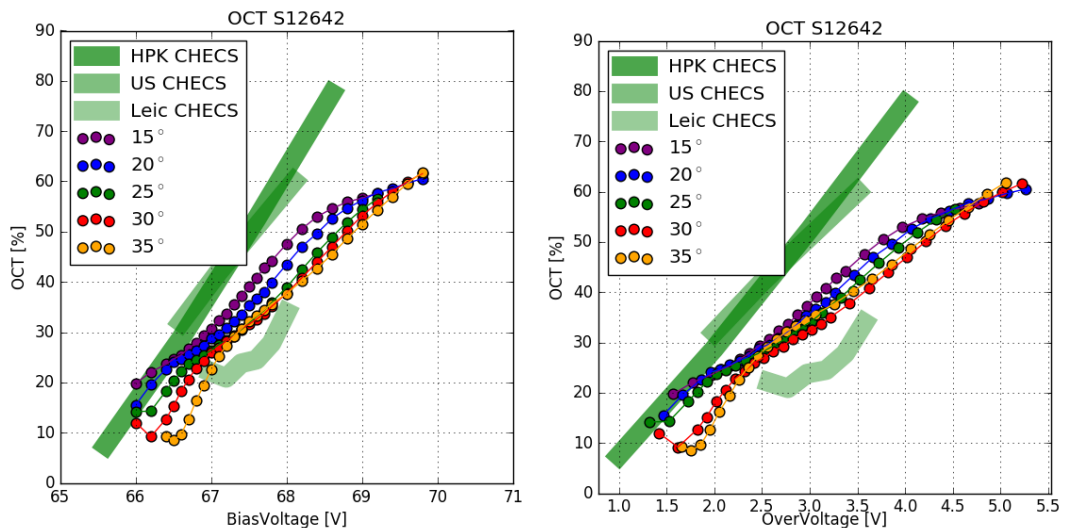


Figure 29: Dark Count Rate of the HPK S12642 pixel, plotted against over-, bias-voltage and temperature.

960 The Optical Cross Talk is expected to be linear and independent from temperature. This is
 961 confirmed for HPK S12642. Minor deviations from that are probably due to slight errors in the
 962 breakdown-voltage calculation from the gain regression line. The deviation of 30°C and 35°C
 963 below an over-voltage of 2V stems from the way the gain regression line is used to calculate
 964 both Dark Count Rate and Optical Cross Talk. At higher temperatures the lower voltage range
 965 is dominated by noise, so using the gain regression line to calculate the Optical Cross Talk at
 966 those low voltages leads to the visible effect of the first few datapoints of 30°C and 35°C .
 967 The deviations between the different groups results at 25°C (green) are caused by 4 major
 968 factors. Firstly the difference in the tested device. While the device measurements in this
 969 thesis has every four 3mm^2 pixels electrically tied together, the way the device will later be
 970 implemented into CHEC-S, the groups in the US[17] and Hamamatsu Photonics[16] are likely

971 to run tests on one 3mm^2 pixel only. Secondly a slight difference in amplification and shaping
972 electronics is suspected. The measurements conducted in this thesis as well as the measurements
973 of Leicester are done with the same shaper and buffer configuration. The difference here is,
974 thirdly, measurements are done with dark counts only, while measurements from other groups
975 are conducted with a pulsed light source and reading out timed windows. This causes the results
976 from Leicester to be difficult to compare against, their surface temperature of the SiPM is likely
977 much higher than 25°C , and thus, a misinterpreted breakdown-voltage at 25°C causes a shift
978 of the Optical Cross Talk to the right. Lastly the difference in actual data taking and analysis
979 procedure must be mentioned, also this is only of minor concern, as we will see with other
980 measured devices.

981 6.3 Hamamatsu LCT5 50 μ m 6mm

983 The Silicon Photomultiplier designated HPK S13360
984 6050CS fig(30) is an LCT5, meaning Low Cross Talk
985 5th iteration device from Hamamatsu Photonics. It is
986 one of the most promising candidates for later usage in
987 CHEC-S. It has a pixel size of 6mm² consisting of 14400
988 cells with a cell size of 50 μ m. The present device and
989 its similar iterations are the first to incorporate trenches
990 bordering each cell, effectively insulating the cells and
991 reducing the prompt Optical Cross Talk. Tests are done
992 with a single pixel only, in contrast to measurements
993 done on S12642. It is mounted on a ceramic chip and
994 coated with a silicon resin that is UV-transparent. Wire-
995 bonds supply the electrical contact. A similar, but not tested, device from the same generation
996 uses through-silicon-via (TSV) technology.

LCT5 6mm

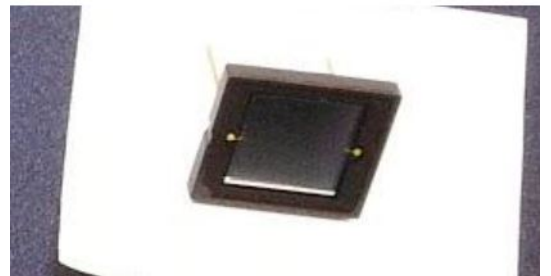


Figure 30: HPK S13360 6050CS pixel

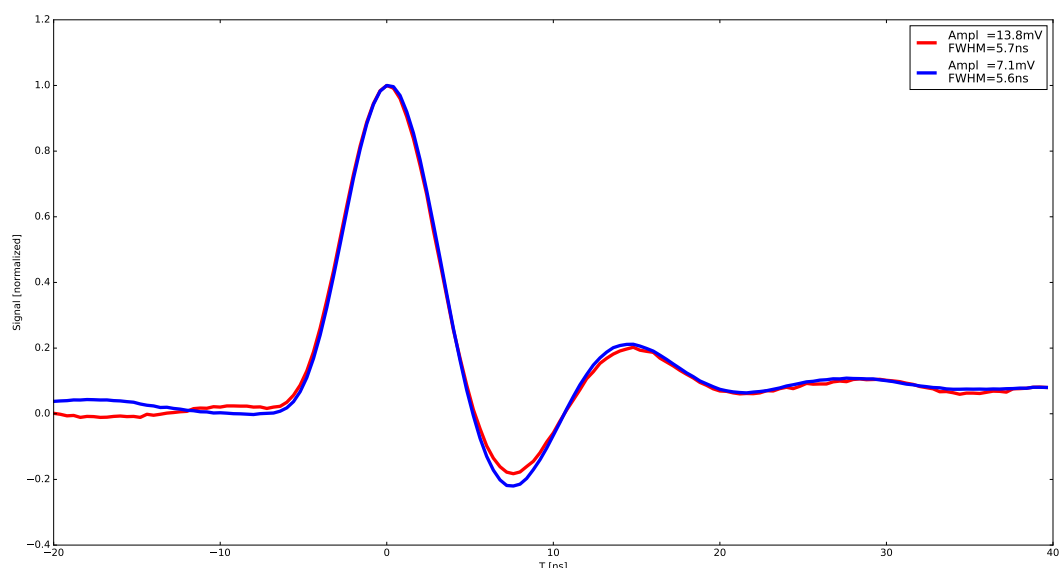
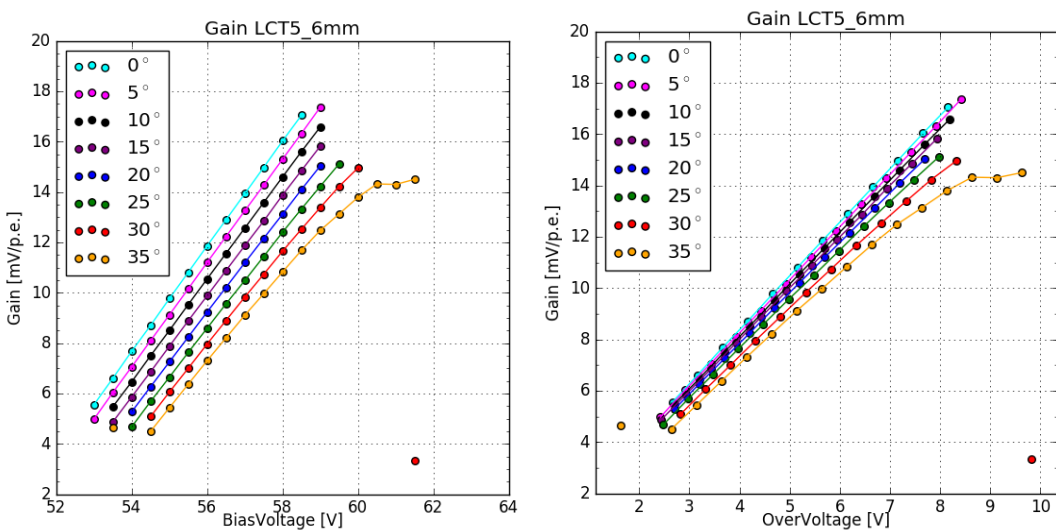


Figure 31: The average pulse shape of the 1 photoelectron in blue and the 2 photoelectron pulse in red of HPK S13360 6050CS at 25° C and at point of operation. Both pulses have a FWHM of around 5ns and ring for approximately 20ns with an undershoot of 20%.

997 The layout of the single pixel test device made external amplification necessary. An amplifier
998 from MiniCircuits was supplied with 13V during this test. Shaping of the pulse is conducted
999 by a CHEC-S shaper, modified to fit the new unshaped pulse. The pulse shape fig(31) makes
1000 the pulses appear much harder to analyze, due to the possibility of events occurring during the
1001 ringing window. This assumption proved untrue, due to the devices low Dark Count Rate and
1002 Optical Cross Talk, resulting in a low multi incident probability.

1003 6.3.1 Gain

1005 The gain of the LCT5 50 μ m 6mm device is clearly linear with some minor outliers at 30°C.
1006 The same effect as with S12642 is visible at 35°C, again counting noise peaks as 1p.e. peaks,
1007 resulting in an apparent lowering of the gain and the slope changing over into a plateau. In
1008 Figure(32)(left) the gain is shown, plotted against over-voltage. It is still dependent on tem-
1009 perature, but due to reliable breakdown-voltage calculation, the spread is much smaller than,
1010 if plotted against bias-voltage. The same conversion is done to transform relative gain into an
1011 absolute gain with sensible units. When parametrized with over-voltage, the gain is essentially
temperature independent.



1012 **Figure 32:** Gain of the HPK S13360 pixel, plotted against over-, bias-voltage and temperature.

1013 6.3.2 Dark Count Rate

1015 The Dark Count Rate of two similar HPK S13360 devices is shown in Figure(33). The bars
1016 show the difference between the two devices, the results of one device is used as a reference,
1017 while the deviation is illustrated with the filled bar. The Dark Count Rate of HPK S13360
1018 follows the expected behaviour, mostly linear in the significant range and rising with increasing
1019 temperature. Below an over-voltage of 2.5 V the gain is suspected to be too low enough so noise
1020 peaks can be misinterpreted as events. Thus the regression line calculation is unreliable in this
1021 range. The turn-up at high over-voltages is most prominent at 0 °C(teal) after an over-voltage
1022 of 9 V. This is also the point where the Optical Cross Talk rises very rapidly. The datasheet
1023 values from the manufacturer cover a large range of the DCR at an over-voltage of 3V, making it
1024 difficult to compare against, the manufacturer determines the DCR by measuring the current.

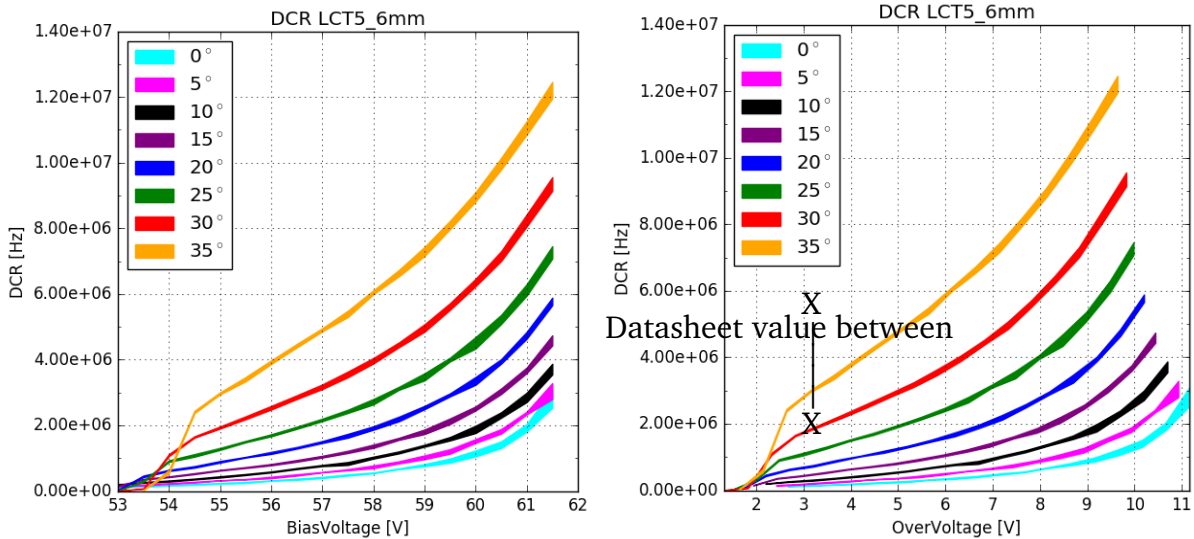


Figure 33: Dark Count Rate of the HPK S13360 pixel, plotted against over-, bias-voltage and temperature. The Datasheet value at 25°C of the DCR at $V_{OV} = 3V$ covers a very large range to exactly compare against, and is measured by current

1025 6.3.3 Optical Cross Talk 1026

1027 The measurements of the HPK S13360 SiPM done at the Nagoya University, Japan fig(34) (faded
1028 green bar), correlate very strong with results from this thesis of the OCT in the over-voltage
1029 range between 2.5V and 9V. The Optical Cross Talk in this range is linear and independent from
1030 temperature, with minor deviations attributed to the breakdown-voltage calculation from the
1031 regression line, causing the horizontal shift. In contrast to the dark counts measurements in this
1032 thesis, the measurements at Nagoya University followed a pulsed light source approach, reading
1033 out a time-window after the laser incident. This could have consequences, since Optical Cross
1034 Talk with a longer delay time could be missed. Deviations below an over-voltage of 2.5V are
1035 expected, they are very likely caused by the regression line calculation being unreliable in this
1036 range due to the analysis method misinterpreting noise as dark count events. Above an over-
1037 voltage of 9V, which is also the point of the turn-up of the Dark Count Rate, the Optical Cross
1038 Talk is no longer linear and the deviation from the results of Nagoya University increase very
1039 rapidly. The rapid increase in both Dark Count Rate and Optical Cross Talk is suspected to be
1040 caused by the over-voltage reaching ranges, where interpretation of noise as a 1p.e. pulse be-
1041 comes more likely. This, joint together with the usage of the MiniCircuits amplifier supplied with
1042 13V, makes false interpretation of noise as pulses even more likely. These two reasons in con-
1043 junction are suspected to be responsible for both, the sudden rise of the Dark Count Rate as well
1044 as the deviation of the Optical Cross Talk from linearity and the results of Nagoya University,
1045 above over-voltages around 9V. In summary, the correlation between the two measurements,
1046 conducted by two different methods of data acquisition and analysis, is evident.

1047

1048

1049 The S13360 series is the first to incorporate physical barriers, called trenches, effectively insu-
 1050 lating the cells from each other. This drastically reduces the prompt cross-talk, while increasing
 1051 the percentage the delayed cross-talk contributes to the overall cross-talk shown. This could
 1052 also be the reason for the up-turn, compared to data from the University of Nagoya; at higher
 1053 over-voltages the contribution from delayed cross-talk is higher[14]. With the trenches effec-
 1054 tively reducing the prompt cross-talk and the difference in analysis, the effect could be partially
 1055 explained by increased contribution of the delayed cross-talk. More on this subject in chapter 7.

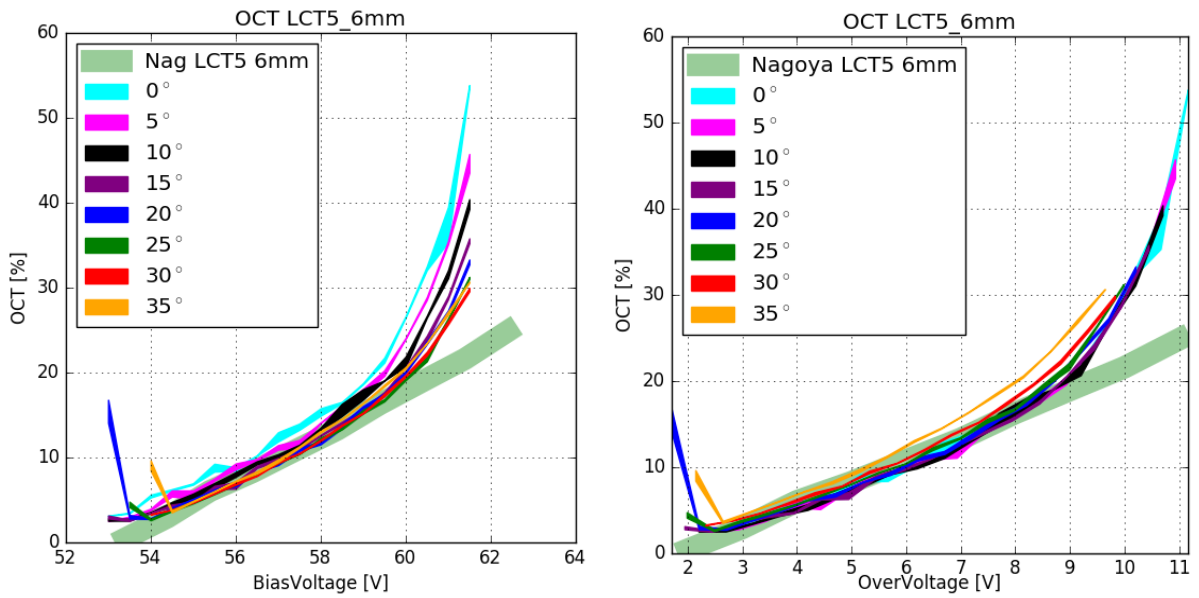


Figure 34: Optical Cross Talk of the HPK S13360 pixel, plotted against over-, bias-voltage and temperature.

1056
1057

6.4 Hamamatsu LCT5 75 μ m 7mm

1058 The device named 6.975MM-SIL Single is a larger LCT5
1059 prototype Silicon Photomultiplier of the same design as
1060 S13360-6050CS fig(35). With an increase in cellsize to
1061 75 μ m, the device gains a higher fill-factor than 50 μ m
1062 devices. The pixel-area is also expanded to 6.915mm²,
1063 which will result in a higher fill-factor (less deadspace),
1064 both size increases together will presumably result in a
1065 higher PDE but also a higher OCT. Since it is a prototype
1066 device, there is limited data from datasheets. The ID
1067 number suggests, that it is also a wire-bond device with
1068 a UV-transparent silicon-resin coating. It is also a single
1069 pixel test device, so external amplification is necessary
1070 with the MiniCircuits PreAMP, supplied with 8V during this test. The signal is shaped by a
1071 differently modified CHEC-S shaper, which results in a pulse shape similar to S12642, but with
1072 a much lower amplitude fig(36).

LCT5 7mm



Figure 35: HPK LCT5 7mm pixel

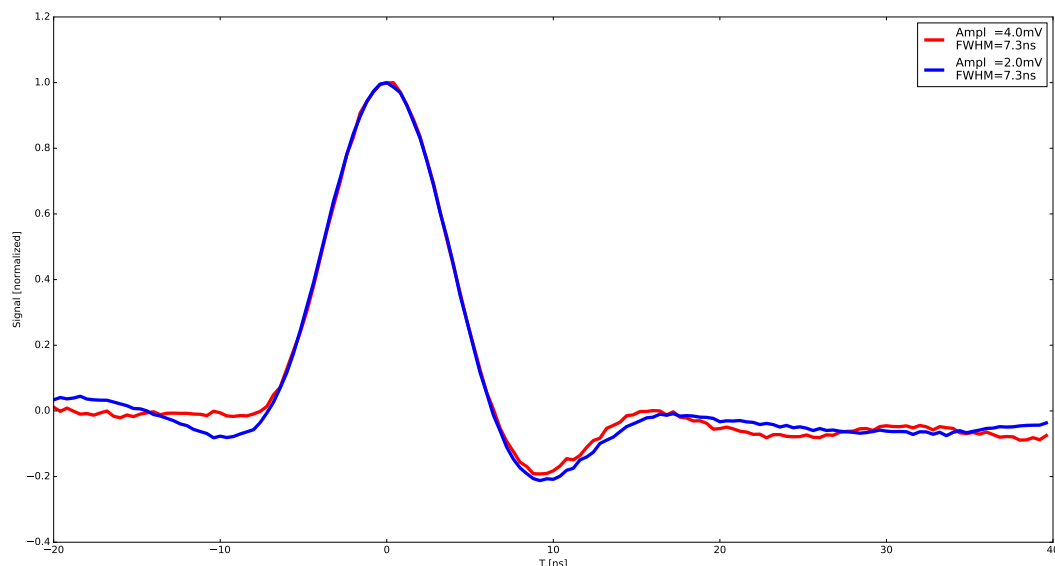


Figure 36: The average pulse shape of the 1 photoelectron in blue and the 2 photoelectron pulse in red of HPK LCT5 7mm at 25° C and at point of operation. Both pulses have a FWHM of around 7ns and an undershoot of 20%, with no ringing.

1073 6.4.1 Gain

1075 Figure(37) shows the gain of the LCT5 7mm de-
1076 vice. Two sets of measurements are done for 25°C
1077 to extend the measured range. The first set of mea-
1078 surements covers the lower over-voltage range,
1079 where the low gain makes external amplification
1080 necessary with a MiniCircuits PreAMP supplied
1081 with 8V. The lowest possible amplification of the
1082 PreAMP is chosen, so that reaching the point of
1083 saturation of the oscilloscope input is as late as
1084 possible as the over-voltage rises. Saturation of
1085 the oscilloscope occurs due to the possibility of
1086 generating very large p.e. (>10 p.e.) events at the
1087 higher over-voltages, which are saturating the in-
1088 put. Joint together, the LCT5 7mm device and the
1089 MiniCircuits PreAMP at 8V reach this point at an
1090 over-voltage of ~ 6 V. In Figure(37) the results from

1091 the lower range measurement are displayed as the lower-range green line extending between an
1092 over-voltage of 1.6V to 5.4V. The configuration for the second test removes the PreAMP from the
1093 setup, which makes the lower over-voltage range unaccesible, but extends the range to higher
1094 over-voltages. This configuration reaches the point of saturation at an over-voltage of ~ 8 V. The
1095 higher range measurement results are displayed as the second green line (25°C) extending from
1096 3.4V to 7.2V over-voltage in Figure(37). There is a clearly visible overlap of the two measure-
1097 ments between ~ 3.4 V and ~ 5.4 V . It also seems, that the gain dependency on temperature is
1098 reversed. While for all other devices, the gain lowers with rising temperatures, the LCT5 7mm
1099 device seems to show inversed behaviour. This inverse behaviour is caused by the calculation
1100 of the breakdown-voltage from the gain-regression line and is likely an error. Plotting the gain
1101 versus bias-voltage, however, shows the expected behaviour of the gain.

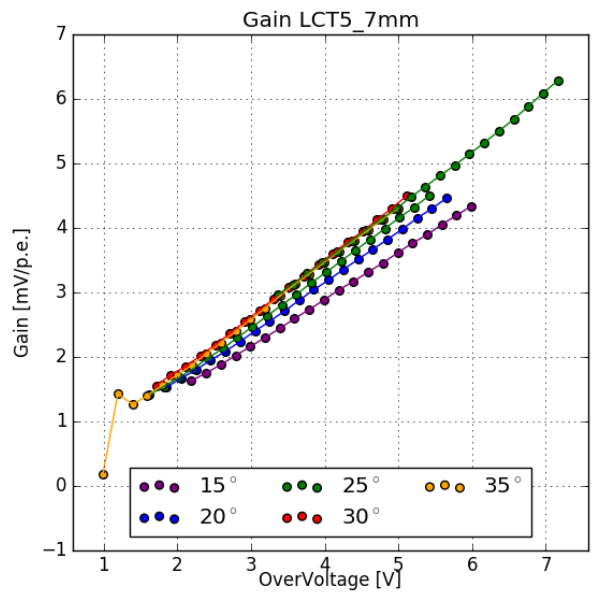


Figure 37: Gain of the HPK LCT5 7mm pixel

1102 6.4.2 Dark Count Rate

1104 The behaviour of the Dark Count Rate of the HPK LCT5
1105 7mm device is shown in Figure(38) and is as expected,
1106 in contrast to the behaviour of the gain of LCT5 7mm,
1107 as discussed in section 6.4.1. It follows a linear pro-
1108 gression in the relevant range and increases with rising
1109 temperature. I suspect the over-voltage range above
1110 $\sim 2.5V$ to be relevant. The extended range measure-
1111 ment at $25^{\circ}C$ confirms this behaviour. LCT5 7mm
1112 shows a linear Dark Count Rate over an over-voltage
1113 range of 4V. The faded green bar in Figure(38) shows
1114 results from measurements undertaken by the Depart-
1115 ment of Physics and Astronomy at the University of
1116 Catania. Those measurements were conducted on the
1117 exact same device, which is an important point, but
1118 with a different method of data acquisition and data analysis. Analysis techniques are dis-
1119 cussed in chapter 7. The correlation between the two experiments is evident, although there is
1120 differences in the acquisition and analysis process.

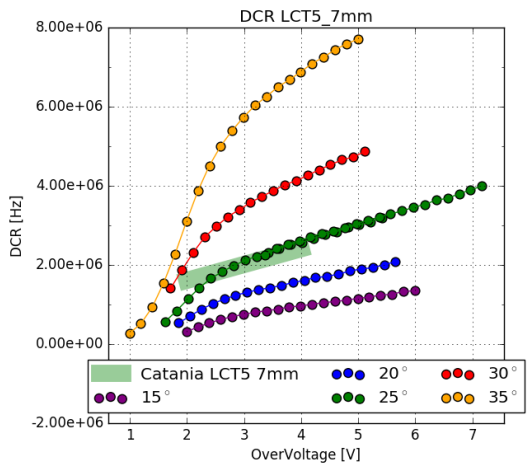


Figure 38: Dark Count Rate of the HPK LCT5 7mm pixel

1121 6.4.3 Optical Cross Talk

1123 The Optical Cross Talk is expected to be linear and in-
1124 dependent from temperature. This is the case in the, in
1125 section 6.4.2 established, relevant over-voltage range
1126 of above $\sim 2.5V$. Minor deviations are attributed to the
1127 calculation of the breakdown-voltage from the gain-
1128 regression line. The over-voltage is calculated from
1129 the former and the supplied bias-voltage, which in turn
1130 causes a slight horizontal shift. With that, comparing
1131 my results to the measurements from the University of
1132 Catania shows a strong correlation.

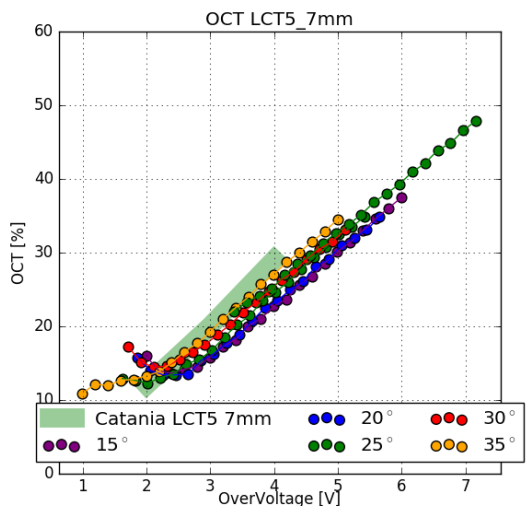


Figure 39: Dark Count Rate of the HPK LCT5 7mm pixel

1133 6.5 Hamamatsu LVR 50 μ m 6mm

1135 The Silicon Photomultiplier by Hamamatsu Photonics
1136 with the designation 6050HWB-LVR-LCT is a special
1137 prototype of the LCT5 design. LVR is an abbreviation
1138 of Low Voltage Range, meaning the device is meant
1139 to be operated at much lower operation voltages than
1140 other LCT5 devices. It has the same physical size as an
1141 LCT5 50 μ m 6mm device (S13360 chapter ??), a pix-
1142 ellsized of 6mm pixel with a cellsize of 50 μ m. The rec-
1143 ommended point of operation however is \sim 15V below
1144 that of the S13360 device, specifically at 40.2V(LVR)
1145 instead of 54.7V (S13360). It uses the TSV technology
1146 for electrical connection. The unshaped signal is similar to other LCT5 devices, therefore us-
1147 ing the same modified CHEC-S shaper is feasible in this case, resulting in a similar pulse shape
1148 fig(41). After that the signal is amplified with the same MiniCircuits PreAMP supplied with 8.5V.
1149

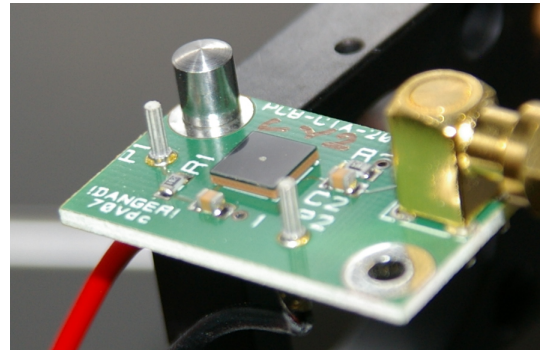


Figure 40: HPK LVR 6mm pixel

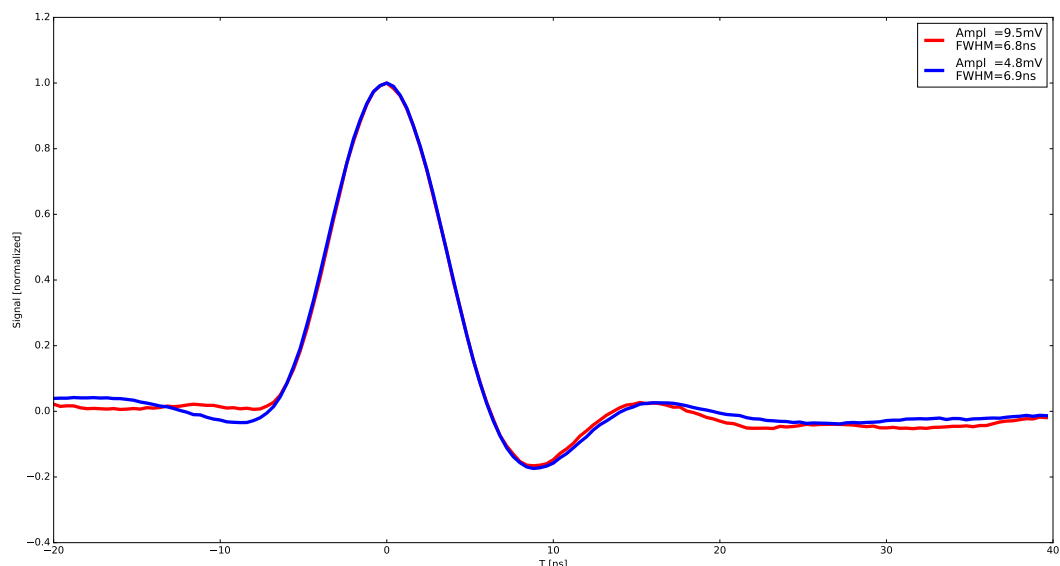


Figure 41: The average pulse shape of the 1photoelectron in blue and the 2photoelectron pulse in red of HPK LVR 6mm at 25° C and at point of operation. Both pulses have a FWHM of around 7ns and an undershoot of 20%, with no ringing.

1150 6.5.1 Gain

1152 Figure(42)(right) shows the gain of the LVR 6mm device. It is, as expected, linear over a
1153 long range and nearly independent of temperature when parametrized with over-voltage. The
1154 flattening of the slope to a plateau shape in the lower over-voltage range is caused by noise

1155 pollution. Only taking into account the linear region, limits the range, where the results are
 1156 relevant to an over-voltage range above ~ 2.5 V. Saturation of the oscilloscope in this range is
 1157 not visible, but a check with a more expanded range revealed, that the point of saturation of
 1158 the oscilloscope is at an over-voltage of ~ 5 V. The apparent overlap of the gain, when plotted
 1159 against over-voltage, is based on the calculation of the breakdown-voltage being very reliable
 1160 due to the large linear range. Plotted versus bias-voltage fig(42)(left) the expected behaviour
 of the gain, lowering with increasing temperature, is visible.

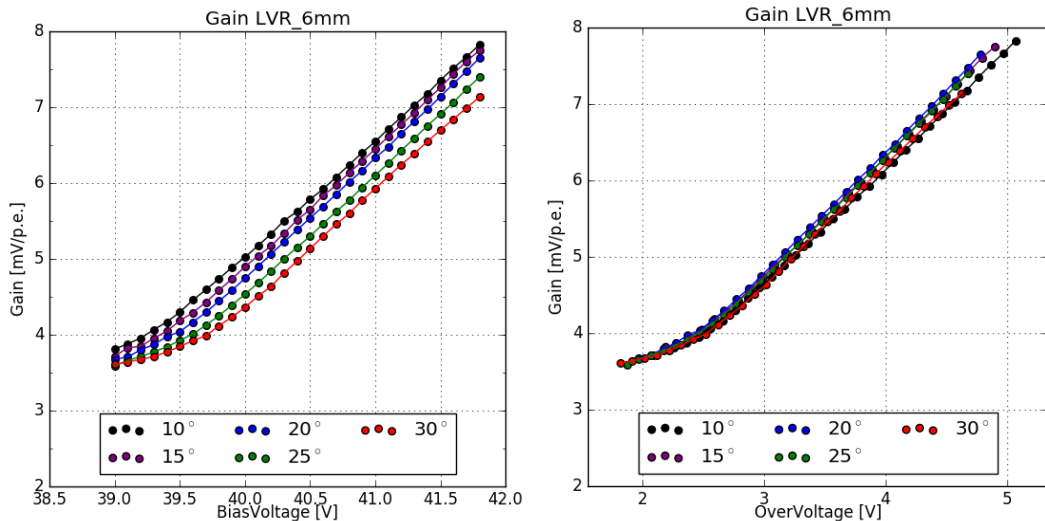


Figure 42: Gain of the HPK LVR 6mm pixel

1161

1162 6.5.2 Dark Count Rate and Optical Cross Talk

1163

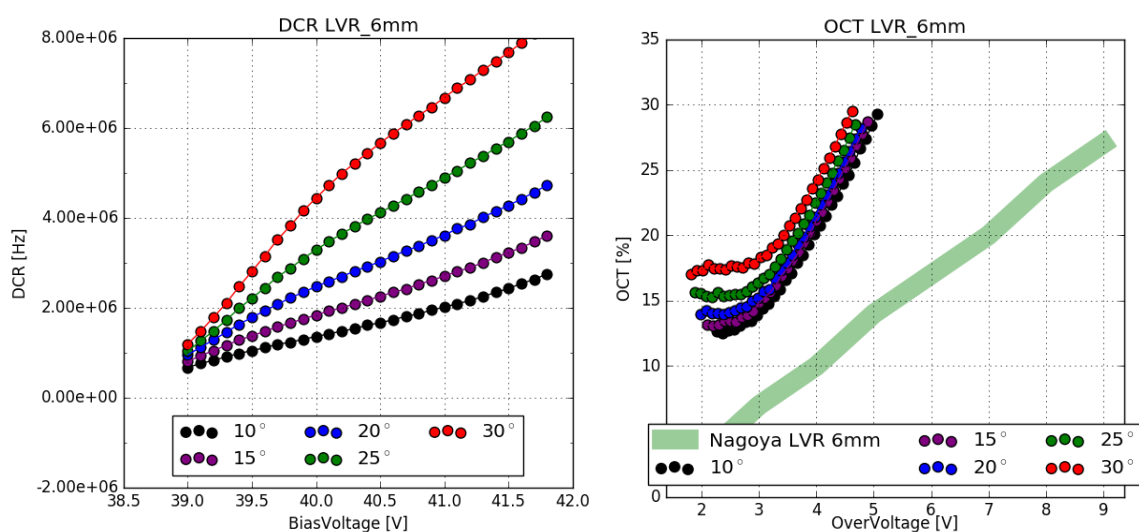


Figure 43: Dark Count Rate and Optical Cross Talk of the HPK LVR 6mm pixel

1164 The Dark Count Rate fig(43)(left), taking into account only the relevant over-voltage range
 1165 of $>\sim 2.5$ V seems to correlate, while the resulting Optical Cross Talk fig(43)(right) is very high

1166 compared to results from the University of Nagoya, which also cover a much wider range.
1167 Only taking into account the previously established relevant over-voltage range of $>\sim 2.5V$, the
1168 resulting Optical Cross Talk is a factor of two higher. The device being a prototype, it could be the
1169 case, that there are physical differences, a difference in coating, which combined with the TSV
1170 technology could lead to the present uncorrelation[19]. This uncertainty is a contrast to results
1171 from previous devices, where strong correlations between different groups and measurement
1172 techniques are evident.

1173 6.6 SensL FJ60035 6mm 35 μ m

1175 The Silicon Photomultiplier by SensL with the designation FJ-60035 is another candidate device
1176 for use to populate the focal plane of CHEC-S. It is also a 6mm device, but with a much smaller
1177 cellsize of 35 μ m, using the TSV technology, so there are no wire-bonds present. This results
1178 in 22292 cells on a single pixel with a fill-factor of 75% . It is coated with plain glass. The
1179 recommended point of operation is around 30V bias-voltage, lower even than that of the HPK
1180 LVR prototypes. The device is, by the manufacturer, pre-mounted on a printed circuit board,
1181 called a test array. This test array contains a fast output, that directly couples to the cells, and a
1182 slow output, conventionally read out via the quench resistor. For the conducted tests, I used the
1183 fast output amplified with the MiniCircuits PreAMP supplied with 12V. The SensL device was the
1184 first device measured, therefore the analysis procedure used was an older iteration compared to
1185 the procedure for the Hamamatsu devices.

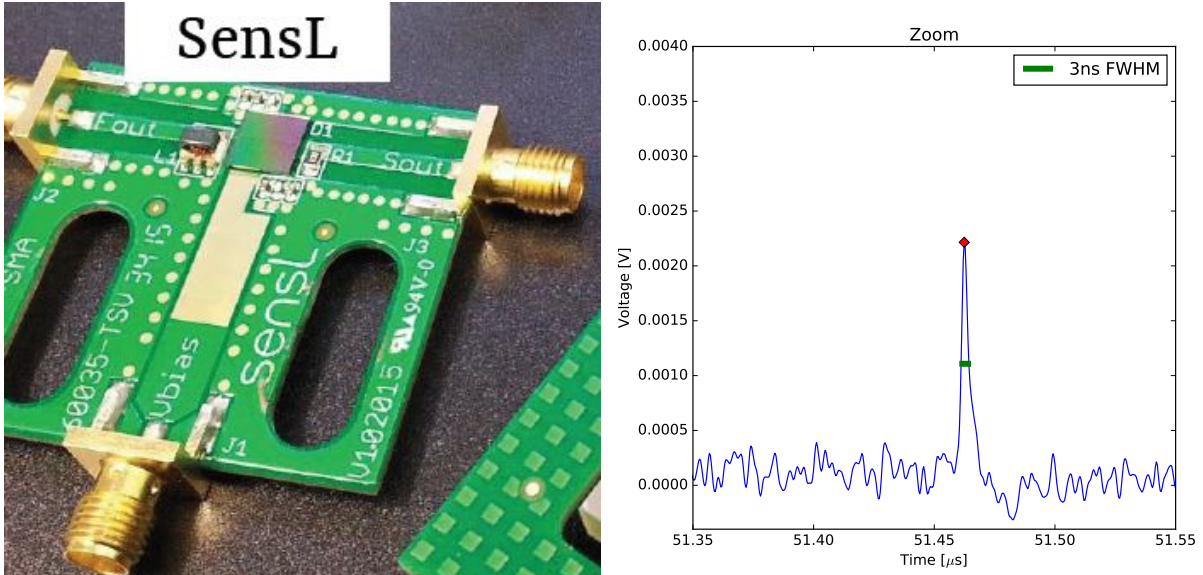


Figure 44: SensL Test Array and the average pulse shape at $V_{bias-voltage} = 29V$

1186 6.6.1 Gain

1188 Evaluating the SensL pulse area spectra shows the 1 p.e. position and Δ p.e. overlapping,
1189 so using the older analysis iteration introduced no error when evaluating the gain of the SensL
1190 device. It is clearly linear over a wide temperature range from -5°C to 35°C over an over-voltage
1191 ranging from 2V up to 8V. When plotted versus over-voltage the spread of the gain is even
1192 tighter signaling slight temperature independency, but still following the expected behaviour of
1193 decreasing with increasing temperature.

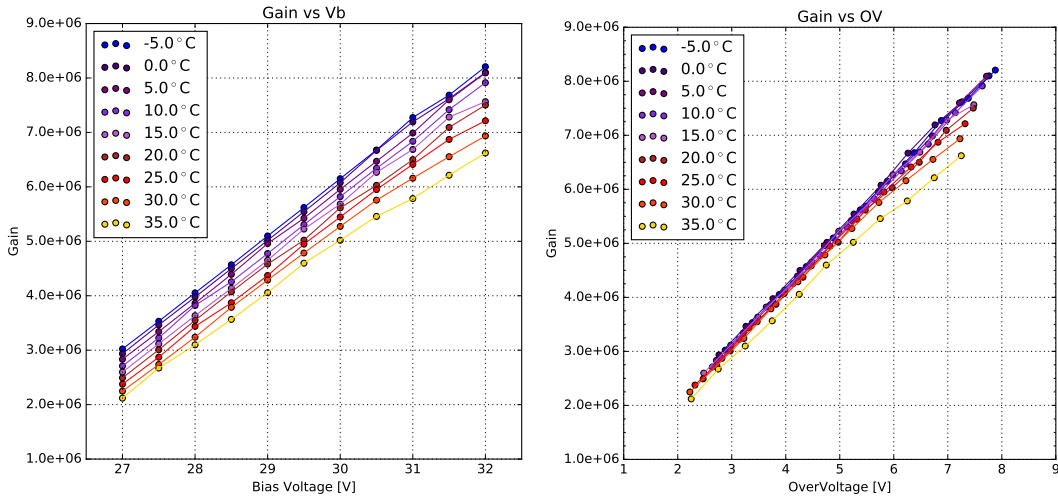


Figure 45: Gain of the SensL FJ-60035 test array

1194 6.6.2 Dark Count Rate and Optical Cross Talk

1195
1196 The Dark Count Rate fig(46)(left) also shows the expected behaviour. At very low temperatures
1197 the changes in rate over the over-voltage range is minimal. Increasing the temperature shows
1198 a rapid increase in thermally induced dark counts. The Optical Cross Talk fig(46)(right) on the
1199 other hand is independent of the device temperature, also as expected. In both cases, the values
1200 agree with values derived from the datasheet.

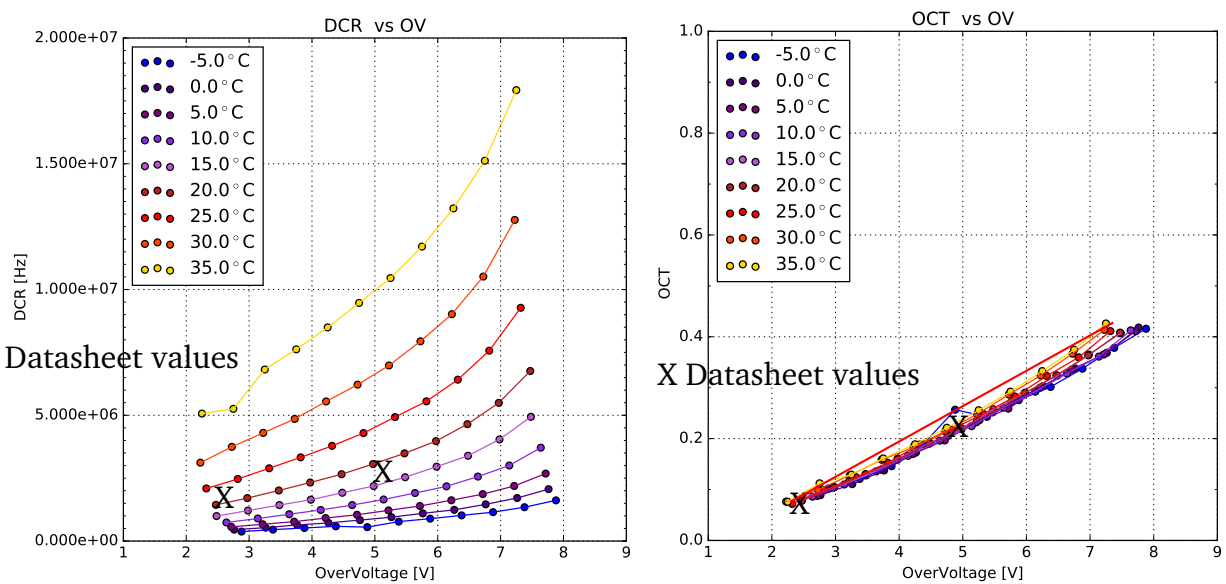


Figure 46: Dark Count Rate and Optical Cross Talk of the SensL FJ-60035 test array. Datasheet values, marked with X, measured at 21°C(~dark red). OCT results of Nagoya University marked by the red line.

1201 1202 7 Comparison

1203 A comparison of the performance of all devices is the significant step for choosing the Silicon
1204 Photomultiplier later to be used in CHEC-S. In order to do this, all measured characteristics are
1205 compared versus over-voltage. Operation of the CHEC-S camera in GCT will come down to a
1206 decision between two operational points. The first point will be marked by an Optical Cross Talk
1207 of under 15%. Every other attribute of the Silicon Photomultiplier at this over-voltage is then
1208 compared. This point will trade off precision for efficiency, a lower Optical Cross Talk makes
1209 real event detection easier, on the other hand, a lower Photon Detection Efficiency may forfeit a
1210 lot of potential data.

1211 The second point of operation is marked at the highest achievable Photon Detection Efficiency.
1212 My conducted measurements do not involve this, other groups are comissioned to determine
1213 the point of highest Photon Detection Efficiency, in other conducted measurements, that are
1214 comparable 51. This point will assure the highest detection of event photons, but will trade
1215 that for an increase in detector noise, due to the higher Dark Count Rate and more importantly
1216 Optical Cross Talk.

1217
1218 Comparing results to other groups is shown in Figure (47), using different experimental se-
1219 tups and procedures and therefore also entirely different analysis techniques. The groups, that
1220 evaluate SiPMs, the University of Leicester, the University of Nagoya and the University of Cata-
1221 nia, are all conducting fixed window readout of the SiPM after an expected light-pulse from a
1222 flasher-LED or pulsed laser.

1223
1224 The SensL device showed a very low PDE compared to the measured HPK devices fig(51).
1225 Therefore the following figures are only showing the HPK results for reasons of visual perfor-
1226 mance.

1227 1228 7.1 Dark Count Rate

1229 Comparing the Dark Count Rate of the measured devices and results from the other groups is
1230 shown in Figure 47. The differences in analysis procedure will only have a slight impact on the
1231 presumed Dark Count Rate, since all experiments record dark-count events over their respective
1232 acquisition time windows. On the other hand, if the readout window is sufficiently small, events
1233 originating from afterpulsing or delayed crosstalk could be missed. All groups experience the
1234 same multi-hit coincidence, meaning a light-event or dark-event coinciding with another, form-
1235 ing a (partial)multi p.e. event.

1236 Only two of the five measured devices have measurements result from other groups to compare,
1237 as it is not their focus. In the case of both, the IVR 6mm and the LCT5 7mm results can be
1238 discussed to some degree as matching. While the correlation is obvious for the LCT5 7mm de-
1239 vice Figure(47)(red), where the covered measurement range in this paper exceeds the external

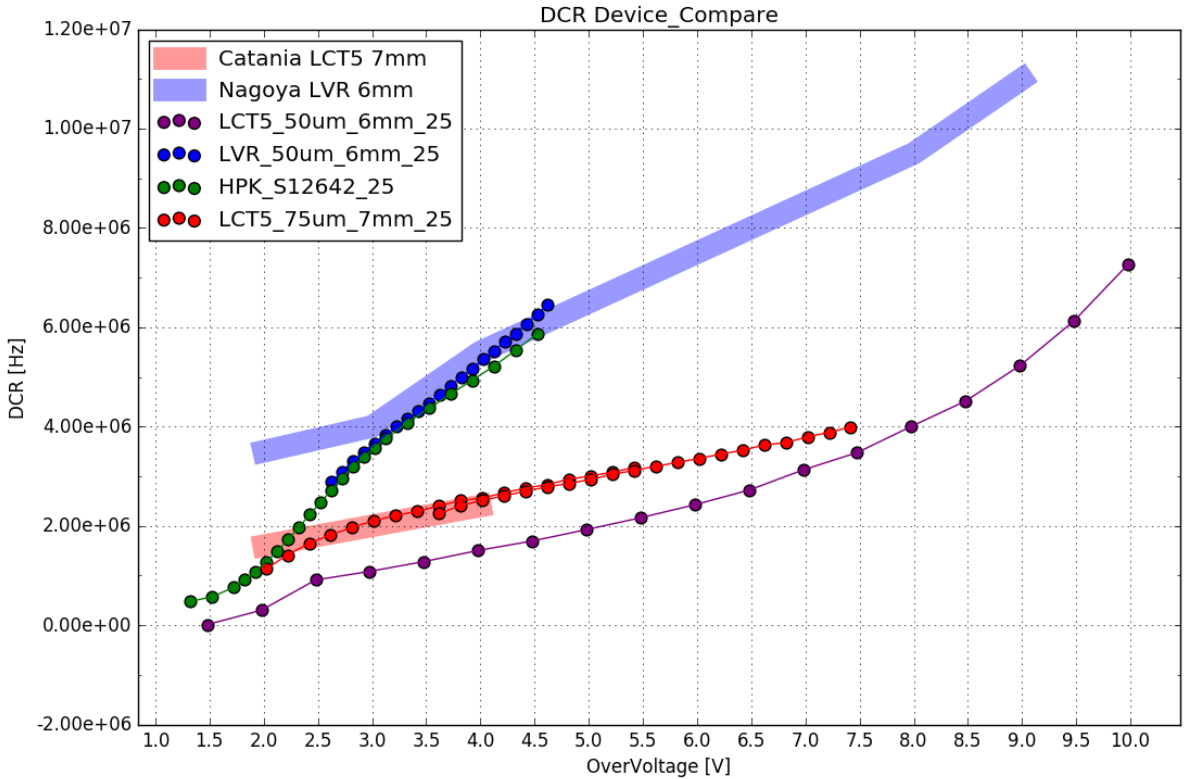


Figure 47: Dark Count Rate comparison of measured devices at 25°C. Description

1240 results, while matching and showing the same trend, the LVR 6mm results deviate. Between an
 1241 over-voltage of 3V and 4V the results overlap, the trend on the other hand is obviously different.
 1242 Additionally the limit on the higher range due to noise makes it impossible to compare against
 1243 the full range measured by the external group, so the DCR for LVR 6mm must be labeled as not
 1244 matching.

1245 7.2 Optical Cross Talk

1246 The comparison of the Optical Cross Talk between the different groups and the results presented
 1247 in this paper are dependent of the analysis and acquisition procedure. Extended trace analysis,
 1248 utilized in this paper captures all aspects of the Optical Cross Talk, prompt and delayed as well
 1249 as afterpulsing. The procedure of time window analysis, utilized by the groups being compared
 1250 to, are, due to their limited window, either biased towards the prompt cross talk or in extreme
 1251 cases, will not be able to capture delayed cross talk or time-delayed afterpulsing at all. Com-
 1252 paring data analysis techniques, for example, at the University of Leicester is therefore a vital
 1253 step. Their approach utilizes a pulsed laser as light source and involves no cooling of the SiPM
 1254 tile. The waveforms are extracted from the scope and a small time window is defined from
 1255 the known time position window of the incident pulse to search for peaks, find their value and
 1256 generate a histogram. To the pulse area histogram, a theoretical model of contributing factors
 1257 is fitted. This theoretical model simulates characteristics, updating continuously to find their cor-

1259 rect values. Those values are the full set of characteristics of the device in testing, among them:
 1260 gain curve, breakdown-voltage, OCT, PDE, noise, dynamic range, crosstalk probability.
 1261 There are a number of differences in their approach compared to the one utilized in this paper,
 1262 most important is the time window size. If the window after an incident pulse is too short,
 1263 data loss is a possibility, depending on the delay time of delayed cross-talk and afterpulsing
 1264 assisted by traps with long lifetimes. This is a problem, especially with devices of the LCT5 gen-
 1265 eration implementing physical trenches isolating the cells and effectively reducing the prompt
 1266 cross-talk, here the contribution from the prompt cross-talk to the overall Optical Cross Talk is
 1267 lowered. Missing data from delayed cross-talk and afterpulsing, because it will not be recorded
 1268 yet, would lead to errors in the overall Optical Cross Talk results being lower than expected.
 1269

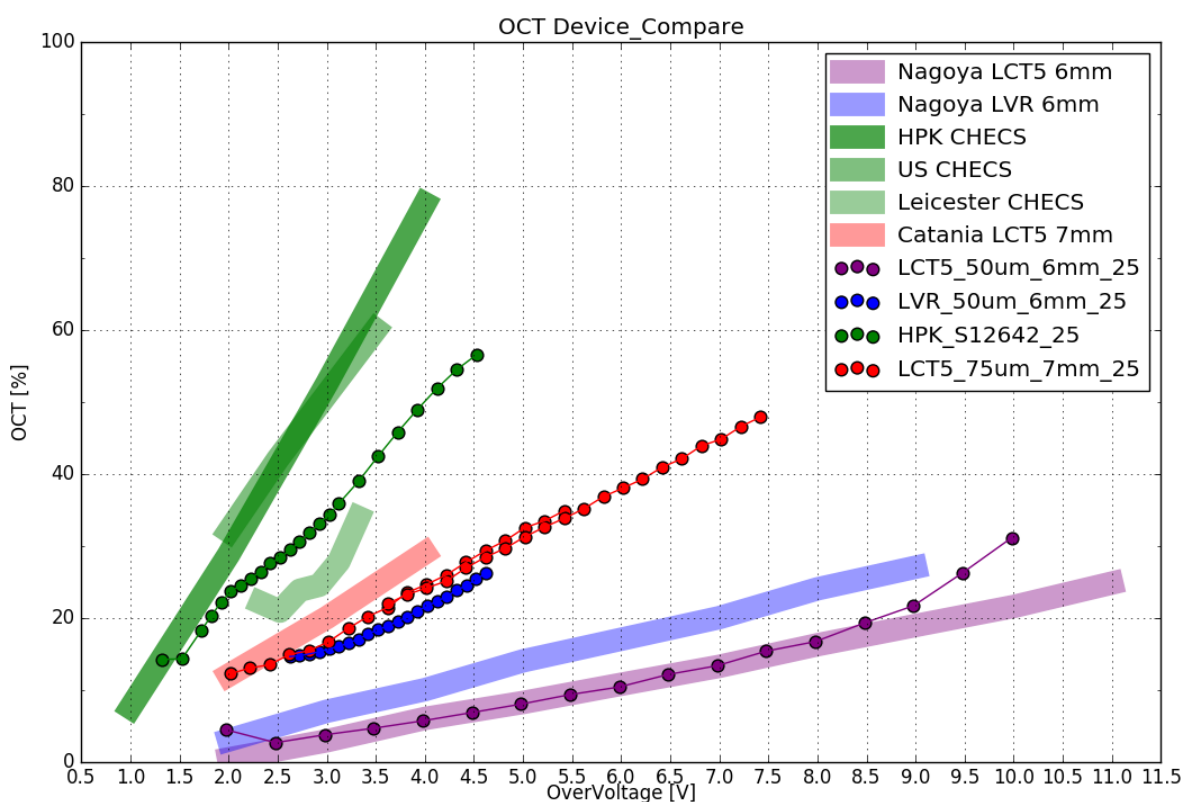


Figure 48: Cross Talk comparison of measured devices at 25°C. Description

1270 This is indeed the case for the S12642 tile in Figure 48 (green). The light green bar below
 1271 (negative y-axis) the dotted data presented in this paper shows the results form the University
 1272 of Leicester indeed being lower. In purple results of the LCT5 S13360 device with physical
 1273 trenches are shown. Compared to results from the University of Nagoya, there is a prominent
 1274 upturn at around an over-voltage of ~8V. This could be due to the differences in analysis tech-
 1275 nique. The University of Nagoya also employs time window analysis. LCT5 posseses lowered
 1276 prompt cross-talk probability, so the contribution of delayed cross-talk to the overall cross-talk
 1277 is higher than for S12642. With rising over-voltage the ratio between prompt and delayed

cross talk shifts towards a higher contribution from delayed cross-talk[14][19]. While at lower over-voltages ($\sim 0.5V$) the cross-talk is nearly entirely dominated by the prompt cross-talk with nearly no contribution of delayed cross-talk, at ($\sim 2V$) contributions are mostly equal and at high over-voltages ($\sim 7V$) the contribution of delayed cross-talk is expected to be above 80%, probably due to higher penetration depth and avalanche probability.

Results of the LCT5 7mm device from both groups mostly overlap, the slight shift between them is most likely caused by a small error in the breakdown-voltage calculation, due to no cooling of the tile in experiments involving light. In addition, the slope of both results seems to be mostly equal, and the extended range measurement, overlapping with the low-range results confirms that.

Even though results from 3 different groups mostly correlate, or have at least partially understood differences, the Optical Cross Talk of LVR 6mm Figure 48 (blue) compared to the results from the University of Nagoya do not show any correlation at all. This is concerning, because comparing S13360 (purple) to the same group showed strong correlation over a wide over-voltage range. Since there is also no datasheet present yet, this device is a prototype, the assumption is that the device examined is physically different than the device present at Nagoya. It may just be a difference in coating, which combined with the TSV technology could lead to the present uncorrelation[19].

7.3 Point of Operation Comparison

A different method of comparison involves the two proposed points of operation, illustrated at the beginning of section 7. By adding the PDE measured by external groups, all three characteristics can be illustrated together. Figure ?? shows the comparison result of the SiPMs examined in this thesis. A minimal OCT point of 15% in the left column, and the maximum PDE points in the right column, both include external PDE measurements.

At the first, minimal OCT, operation point the LCT5 6mm (S13360) device is favorable, since it possesses a high PDE of 49% with a fairly low DCR below the expected NSB. The currently used SiPM in CHEC-S only reaches 25% according to datasheet values.

The four HPK devices (the first four in the list), all have a maximum achievable PDE around the same level, $\sim 50\%$. The difference in DCR and OCT at this level is the deciding factor. While the current CHEC-S SiPM reaches a very high OCT level of $\sim 50\%$, the newer generation HPK SiPMs, with physical trenches, are well below at $\sim 25\%$. The DCR on the other hand seems to be similar for each device. The LCT5 7mm SiPM at this point of operation seems to have the lowest DCR among them, but the measurements of this device have not yet reached the maximum PDE value and will be extended, higher PDE is possible.

In both cases, the PDE of the SensL SiPM is not competitive.

Device	Min. OCT			Max. PDE		
	OCT	DCR	PDE	OCT	DCR	PDE
CHECS	15%	0.5 MHz	25% (DS)	50%	5 MHz	48% (DS)
LCT5 6mm	15%	3.4 MHz	49% (Nagoya)	22%	5 MHz	51% (Nagoya)
LCT5 7mm	15%	2.0 MHz	42% (Catania)	25%	2.5 MHz	53% (Catania)
LVR 6mm	15%	2.5 MHz	43% (Nagoya)	>27%	>6MHz	>50% (Nagoya)
SensL	15%	3.0 MHz	37% (Nagoya)	30%	6 MHz	40% (Nagoya)

Figure 49: Comparison table of the measured devices based on the two proposed operation points for CHEC-S. First point represents minimal achievable OCT, second point represents maximum achievable PDE. PDE values taken from results of other groups and datasheet values. Note that the LCT5 6mm device can achieve even lower OCT values ($\sim 3\%$ at $V_{ov} = 2.5$)

1314
1315

7.4 Photon Detection Efficiency

1316 The measurement technique in this paper utilizes only dark counts and aims at giving an un-
 1317 derstanding of the Optical Cross Talk and temperature dependencies of the different SiPMs
 1318 proposed, therefore no PDE measurements are possible. The point of operation with the highest
 1319 PDE as well as the PDE versus OCT behaviour is determined by a different group in Japan, at
 1320 the University of Nagoya. See Figure (51) for the current results of their endeavors. A figure
 1321 showing the behavior of PDE versus OCT is the usual procedure of comparing SiPMs, it gives a
 1322 correlated overview of the two most significant characteristics. This gives insight of the capabil-
 1323 ities of the different devices compared to the two proposed points of operation in section (7.3).
 1324 For consistency and to make comparison between group results easier, the PDE ascertained by
 1325 the groups, of devices in common, compared to the resulting Optical Cross Talk from this paper
 1326 produces Figure (50).

1327

1328 Comparing all devices at the two proposed points of operation produces the table in
 1329 Figure(49). This table together with Figure (50) of the 5 measured devices in this thesis,
 1330 where PDE data is accesible, is used to confirm results between groups and assist in the de-

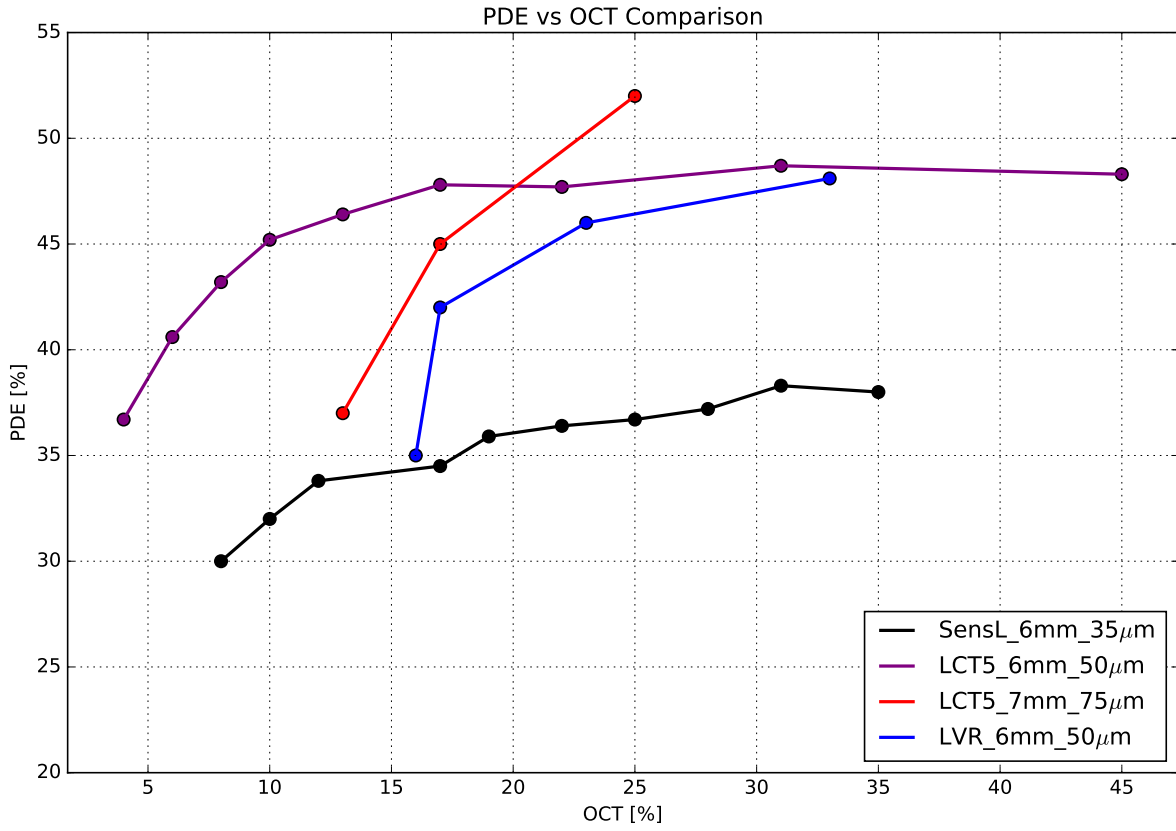


Figure 50: PDE results from the University of Nagoya parametrized with OCT results from this paper, where available. PDE measurements at $\lambda = 400\text{nm}$. An optimum device for IACT application would be in the upper left region.

cision on the most viable SiPM for CHEC-S. The final decision will be taken by the group at the University of Nagoya, by Hiro Tajima, the Photosensor work group lead scientist? of GCT based on measurements on substantially more devices (see appendix H, for the complete list). The PDE of SiPMs, when plotted versus the corresponding OCT at a common over-voltage point show the behaviour in Figure (50). A clearly visible saturation after a certain OCT marks the

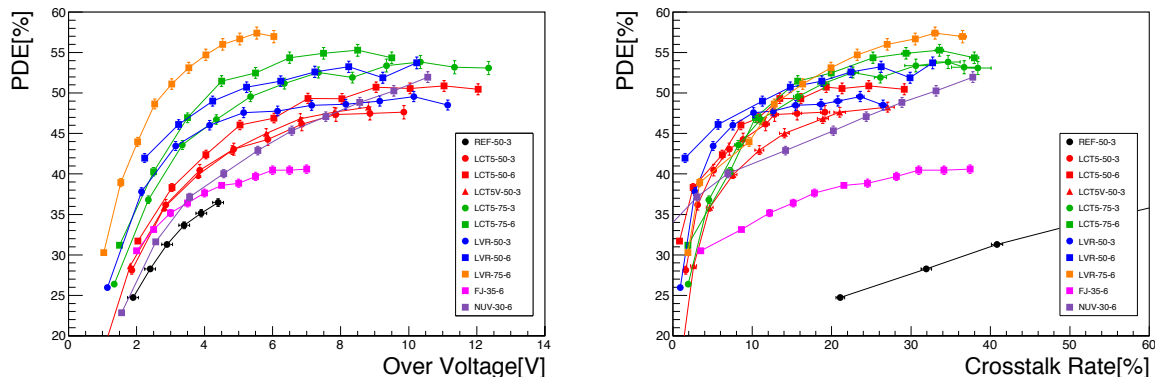


Figure 51: PDE Comparison Plots from the University of Nagoya at $\lambda = 400\text{nm}$

1336 point, from where an increase in power no longer increases photon-detection capabilities. An
1337 increase in OCT without rising PDE would have a adverse effect on the detectors resolution.

1338

1339 The prototype LCT5 7mm fig(50)(red) device reaches the highest PDE. While the prelimi-
1340 nary external measurements show only 3 datapoints, a trend above 50 % is visible. This is
1341 expected for devices with larger cell- and pixel-size possesing a higher fill-factor. The increase
1342 in size and therefore PDE comes with a trade-off, increasing size comes with a rise of DCR and
1343 OCT, which are very high at this point (at $\sim 25\%$).

1344 The commercially available LCT5 6mm (HPK S13360) SiPM shows the most promising results.
1345 It reaches a high PDE very quickly compared to its OCT, with $\sim 47\%$ before the OCT reaches
1346 20%. Compared to this, the OCT of the LVR 6mm at a point where the PDE saturates and
1347 reaches the same PDE is very high.

1348 Due to the low fill-factor, the PDE of the SensL FJ60035 device is not competitive.

1349 ' _____ >' CHEC-S measurements of the PDE, add to
1350 figure

1351 1352 8 Conclusion and Outlook

1353 Over the course of this thesis five new-generation Silicon Photomultipliers have been exam-
1354 ined in dark conditions, for their possible use in single photon detection for the high energy
1355 instrument of the Cherenkov Telescope Array. A lasting experimental teststand has been de-
1356 veloped, that is capable to be upgraded for future illumination tests. The teststand involves
1357 a climate chamber for temperature regulation, that functions as a light tight box. For each
1358 SiPM pre-existent shaping electronics has been modified in order to achieve a prefered signal.
1359 Data acquisition code was developed to control the experimental parameters of the teststand
1360 remotely, and storing all experimental data from the internal memory of the oscilloscope on a
1361 Lab-PC. A data analysis procedure has been designed and developed to analyze the data offline,
1362 both were developed in python.

1363 ' _____ >'

1364 For that purpose 5 different SiPM from two manufacturers have been examined.

9 Glossary

- 1367 1. SiPM - Silicon Photomultiplier
- 1368 2. IACT
- 1369 3. CTA - Cherenkov Telescope Array
- 1370 4. LST
- 1371 5. MST
- 1372 6. SST
- 1373 7. GCT
- 1374 8. CHEC
- 1375 9. HPK - Hamamatsu Photonics K.K.
- 1376 10. SensL - Sense Light

1377 1378 10 Bibliography

1379 1380 References

- 1381 [1] Jim Hinton et al. *Teraelectronvolt Astronomy* Ann. Rev. Astron. Astrophys., 47:523
- 1382 [2] The CTA Consortium *Design Concepts for the Cherenkov Telescope Array CTA, An Advanced*
1383 *Facility for Ground-Based High-Energy Gamma-Ray Astronomy* ; arXiv:1008.3703v3 [astro-
1384 ph.IM] 11 Apr 2012
- 1385 [3] Teresa Montaruli et al. *The small size telescope projects for the Cherenkov Telescope Array*
1386 arXiv:1508.06472v1 [astro-ph.IM]
- 1387 [4] *The ASTRONET Infrastructure Roadmap* ISBN: 978-3-923524-63-1
- 1388 [5] Jim Hinton et. al *Seeing the High-Energy Universe with the Cherenkov Telescope Array* As-
1389 troparticle Physics 43 (2013) 1-356
- 1390 [6] R. López-Coto for the HAWC collaboration *Very high energy gamma-ray astronomy with*
1391 *HAWC* arXiv:1612.09078v1 [astro-ph.IM] 29 Dec 2016
- 1392 [7] John Murphy *SensL J-Series Silicon Photomultipliers for High-Performance Timing in Nuclear*
1393 *Medicine*
- 1394 [8] A. N. Otte et al. *Characterization of three high efficient and blue sensitive Silicon photomul-*
1395 *tipliers* arXiv:1606.05186v2 [physics.ins-det] 26 Jan 2017
- 1396 [9] A. Bouvier et al. *Photosensor Characterization for the Cherenkov Telescope Array: Silicon*
1397 *Photomultiplier versus Multi-Anode Photomultiplier Tube* ; arXiv:1308.1390v1 [astro-ph.IM]
1398 6 Aug 2013
- 1399 [10] V. Vassilieva , S. Fegan *Wide field aplanatic two-mirror telescopes for ground-based*
1400 *gamma-ray astronomy* Astropart. Phys. 28 (2007) 10, [astro-ph/0612718] arXiv:astro-
1401 ph/0612718v2 12 Apr 2007
- 1402 [11] A. Zech, J.-P. Amans, S. Blake et al. *SST-GATE: A dual mirror telescope for the Cherenkov*
1403 *Telescope Array* arXiv:1307.3035v1 [astro-ph.IM] 11 Jul 2013
- 1404 [12] Julien Rousselle et al. *Construction of a Schwarzschild-Couder telescope as a candidate for*
1405 *the Cherenkov Telescope Array: status of the optical system* arXiv:1509.01143v1 astro-ph.IM
- 1406 [13] J. Rosado S. Hidalgo *Characterization and modeling of crosstalk and afterpulsing in Hamamatsu*
1407 *silicon photomultipliers.* arXiv:1509.02286v2 [physics.ins-det] 21 Oct 2015
- 1408 [14] K. Boone, Y. Iwai, F. Retiere, C. Rethmeier *Delayed avalanches in Multi-Pixel Photon Counters*
1409 arXiv:1703.04651v1 [physics.ins-det] 14 Mar 2017

- 1410 [15] Robert G. Wagner et al. *The Next Generation of Photo-Detectors for Particle Astrophysics*
1411 arXiv:0904.3565v1 [astro-ph.IM] 22 Apr 2009
- 1412 [16] *Opto-semiconductor handbook Chapter 03 Si APD, MPPC*. Hamamatsu Photonics K.K.
- 1413 [17] Jonathan Biteau et al *Performance of Silicon Photomultipliers for the Dual-Mirror Medium-*
1414 *Sized Telescopes of the Cherenkov Telescope Array* arXiv:1508.06245v1 [astro-ph.IM] 25 Aug
1415 2015
- 1416 [18] Richard White *private communication*. 2017
- 1417 [19] Koei Yamamoto *private correspondence*. 2016
- 1418 [20] Luigi Tibaldo *Initial testing at MPIK (wb July 18 2016)* July 2016
- 1419 [21] T. C. Awes et al. *Configurable electronics with low noise and 14-bit dynamic range for*
1420 *photodiode-based photon detectors* Nuclear Inst. and Methods in Physics Research, Mai 2006
- 1421 [22] Maurice Stephan. *Design and Test of a Low Noise Amplifier for the Auger Radio Detector*
1422 Diploma Thesis, RWTH Aachen University, July 2009
- 1423 [23] Benjamin Glauß. *Optical Test Stand and SiPM characteriation studies*. Master's Thesis,
1424 RWTH Aachen University, June 2012.
- 1425 [24] Hiro Tajima *Roadmap for Procurement of SiPMs*, GCT Meeting, Amsterdam, February
1426 15–17, 2017
- 1427 [25] http://astro.desy.de/gamma_astronomy/cta/index_eng.html
- 1428 [26] [http://www.ung.si/en/research/laboratory-for-astroparticle-physics/
1429 projects/cta/](http://www.ung.si/en/research/laboratory-for-astroparticle-physics/projects/cta/)
- 1430 [27] [http://www.ung.si/en/research/laboratory-for-astroparticle-physics/
1431 projects/fermi-lat/](http://www.ung.si/en/research/laboratory-for-astroparticle-physics/projects/fermi-lat/)
- 1432 [28] [http://212.71.251.65/aspera//index.php?option=com_content&task=
1433 blogcategory&id=111&Itemid=234](http://212.71.251.65/aspera//index.php?option=com_content&task=blogcategory&id=111&Itemid=234)

1434 1435 11 Appendix

1436 A CTA 1437

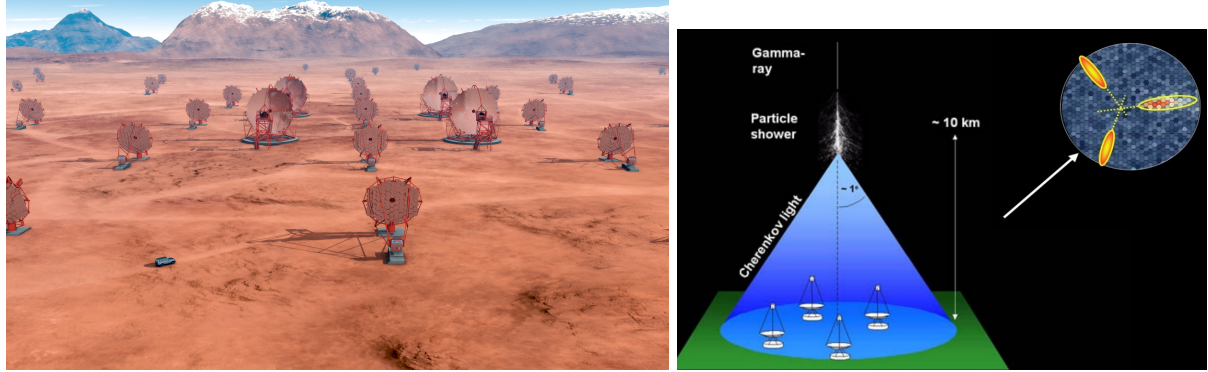


Figure 52: A render of the finished CTA Array at the site in Chile (left) with visible LSTs and MSTs, and the Shower Path Reconstruction technique of the stereoscopic view employed by current IACT experiments like HESS, MAGIC, VERITAS (right).

1438 B progenitor experiments of CTA 1439



Figure 53: IACT Projects: HESS in the Khomas Highland, Namibia. MAGIC at the Roque de los Muchachos Observatory on La Palma , one of the Canary Islands. VERITAS at Mount Hopkins, Arizona, USA

C OCT dependency on cellsize

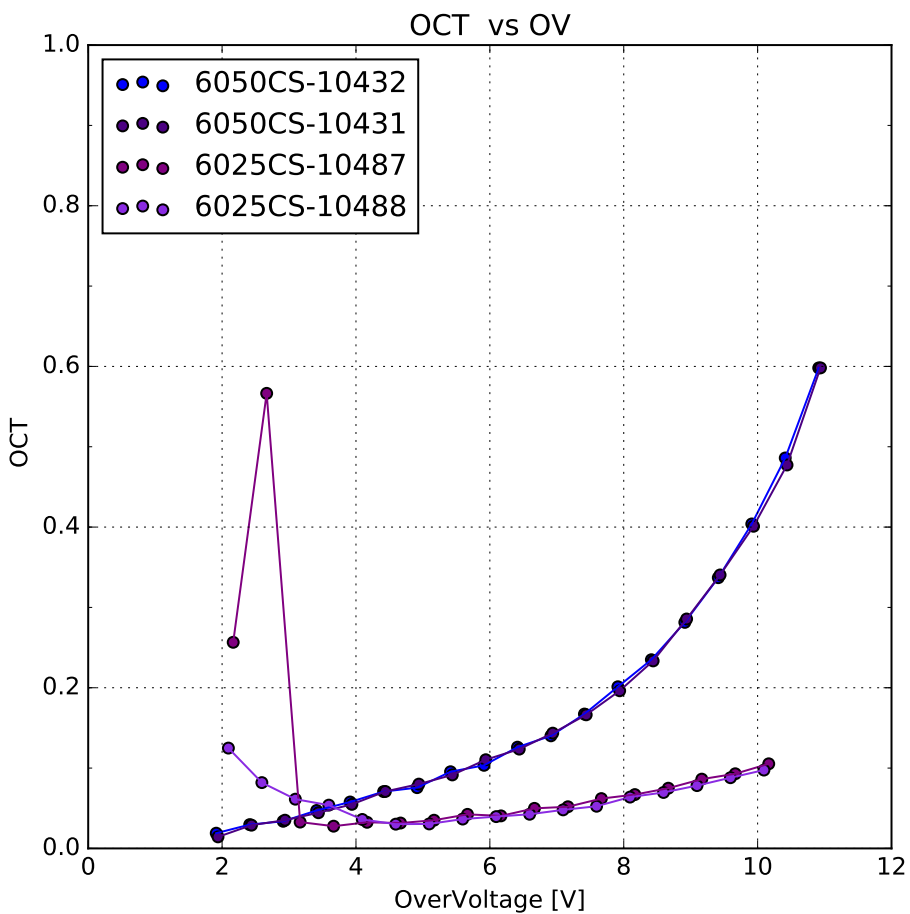


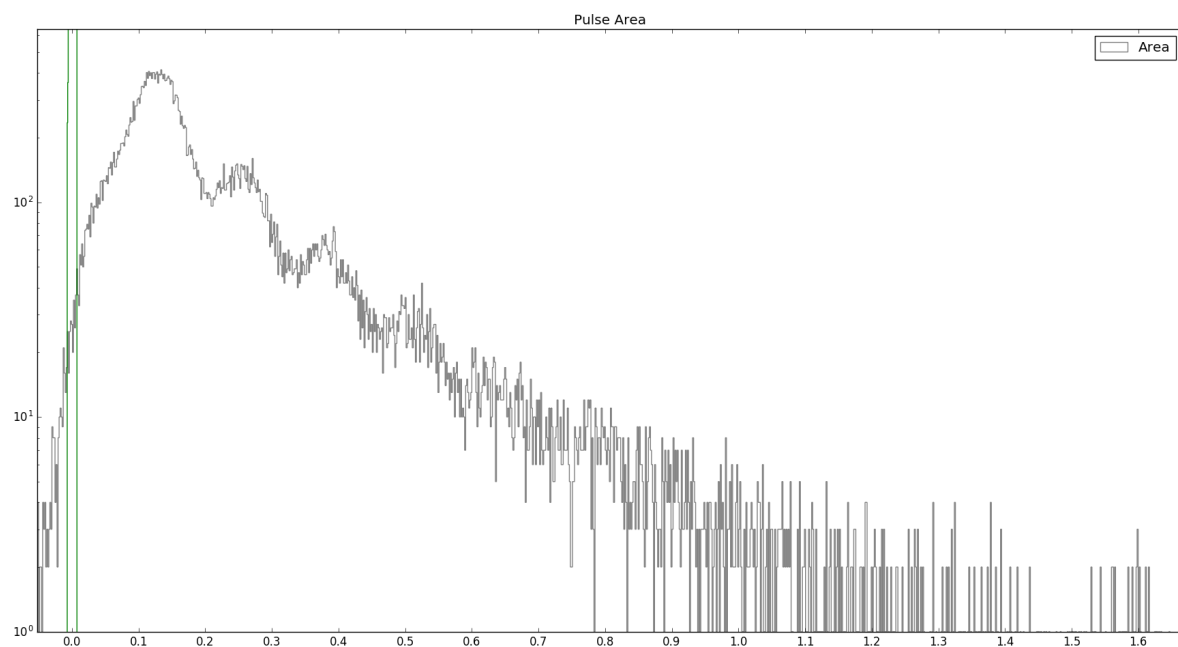
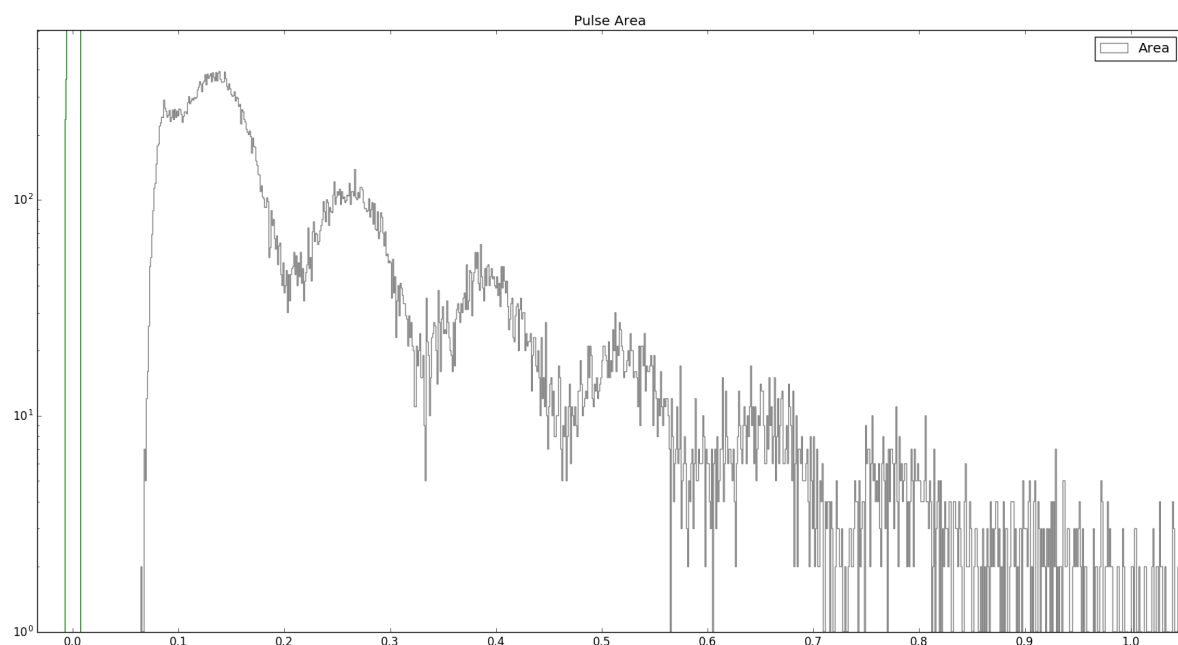
Figure 54: Results of the Optical Cross Talk of two sets of two similar HPK S13360 devices, that only differ in their respective cell-size. HPK S13360 is the first device incorporating physical trenches in the upper layer, optically isolating each cell. Consequence to this is a drastic reduction in prompt cross-talk. Delayed cross-talk and afterpulsing are basically unaffected. Upscaling the $25\mu\text{m}$ results shows an overlap between the 2, see text.

In Figure (54) the results of the complete Optical Cross Talk of 2 sets of $50\mu\text{m}$ and $25\mu\text{m}$ HPK S13360 devices are shown. Plotting the results of 2 similar devices, only different in their cell-size, and then multiplying the $25\mu\text{m}$ results by the factor derived from their difference in area, here 4, a correlation is visible. Scaling up the Optical Cross Talk of the $25\mu\text{m}$ cell, shows an overlap between the 2 cell-sized pixels. This means, that the Optical Cross Talk is directly area and therefore cell-size dependent. Research by J. Rosado and S. Hidalgo [13] on the cross-talk probability of Hamamatsu SiPMs showed through Monte Carlo simulation, that the prompt crosstalk mostly takes place in a small area of pixels (~ 8) around the primary one. Which means, that the cross-talk is directly increasing with increasing cell-size, or in other words: with chance to diffuse to a neighboring cell. Small cells reduce the chance, as there is less area to a neighboring

1452 cell to pass through.

1453 Since the measurements conducted by me do not differ between the range of secondary
1454 avalanche effects, the Optical Cross Talk shown contains every aspect, prompt and delayed
1455 as well as afterpulsing.

D Pulse Area Spectra of different integration window widths



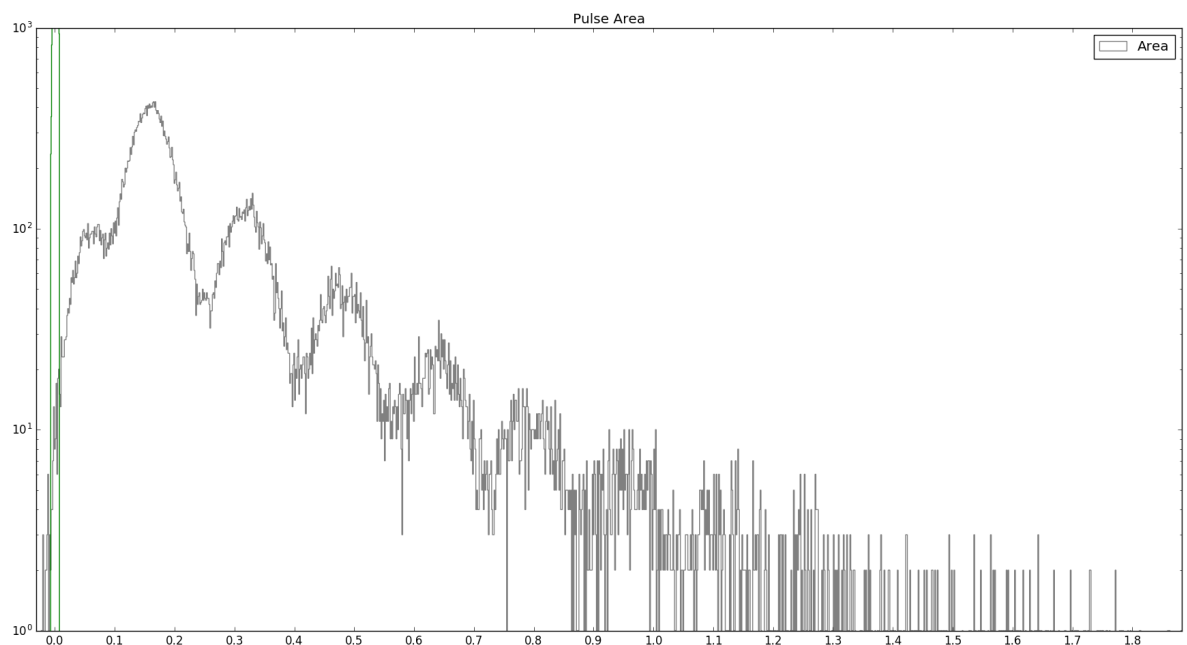


Figure 55: Pulse Area Spectra with window widths of 5 left 5 right (top), 5 left 20 right (middle), 10 left 10 right (bottom) bins respectively. Left of the 1p.e. peak of the top picture a part of the 0p.e. peak is visible. The middle figure shows the distortion an asymmetrical integration window causes. The bottom figure is the employed integration window to derive the pulse area histogram.

E BreakdownVoltage

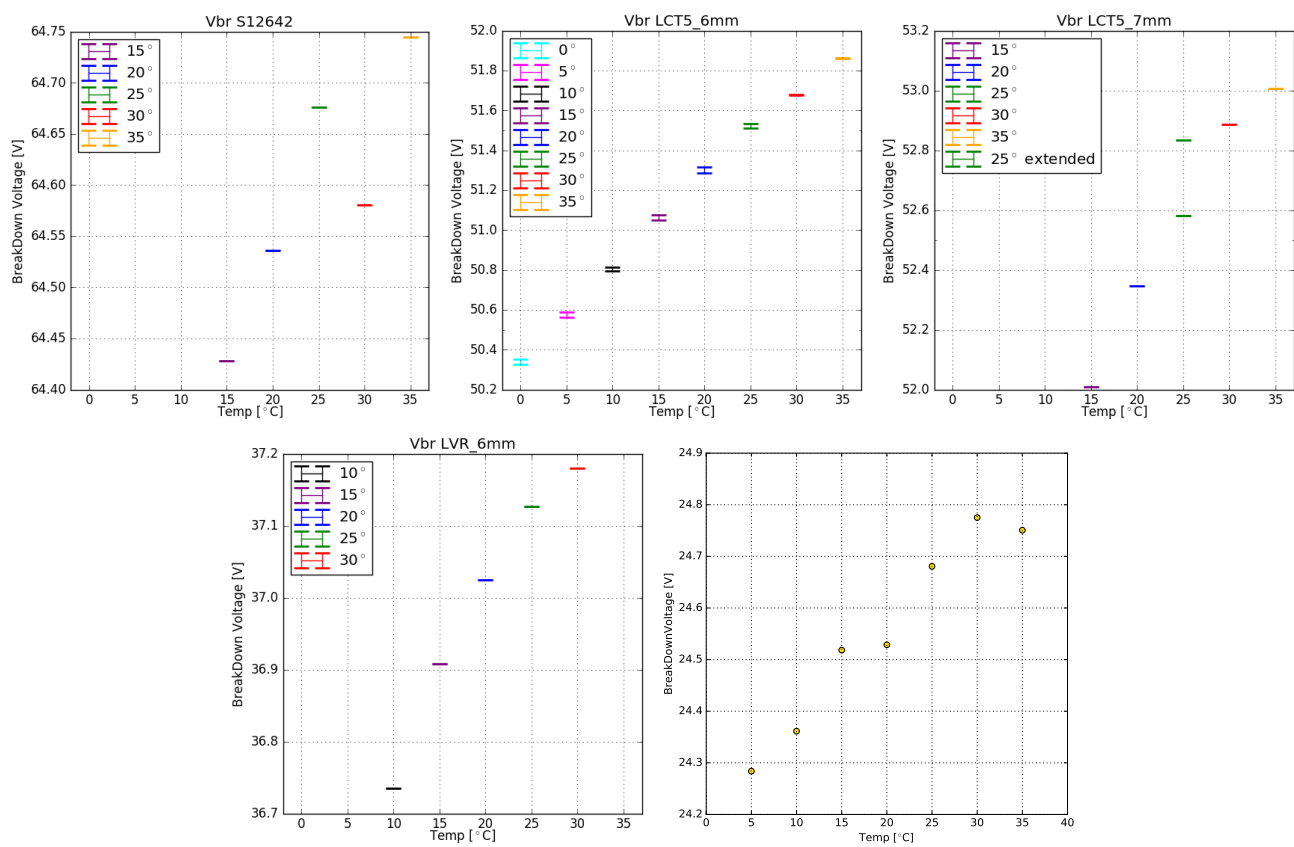


Figure 56: Dependency of the breakdown-voltage of temperature for the 5 measured devices.

For LCT5 7mm , the extended range measurement adds an extra datapoint at 25°C
 HPK S12642 (CHEC-S) (top left) ; HPK LCT5 6mm (top middle) ; HPK LCT5 7mm (top right) ; HPK LCT5 LVR 6mm (bottom left) ; SensL FJ60035 (bottom right).

Device	$\Delta V / T$ [mV/°C]
CHECS	13.1 ± 4.1
LCT5 6mm	43.5 ± 0.4
LCT5 7mm	53.0 ± 4.0
LVR 6mm	25.6 ± 2.6
SensL	15.0 ± 1.1

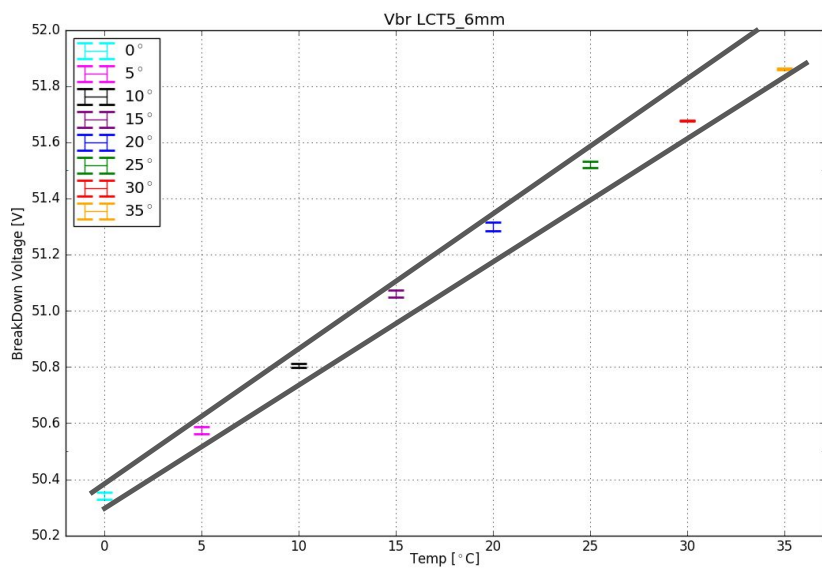


Figure 57: The extracted breakdown-voltage dependence of all measured devices, derived from two regression lines and their mean. For some devices the breakdown-voltage dependency is known through datasheet values. S12642 = 60mV/°C, S13360 = 54mV/°C, SensL FJ60035 =<21.5mV/°C

F Shaper



Figure 58: The shaped and unshaped pulse from a pulse generator emulating the output of the front-end buffer of the CHEC-S SiPM. The unshaped pulse in yellow and negative, due to the buffer-output. The shaped pulse now flipped through the electronics in green. Zoomed, Image credit [20]

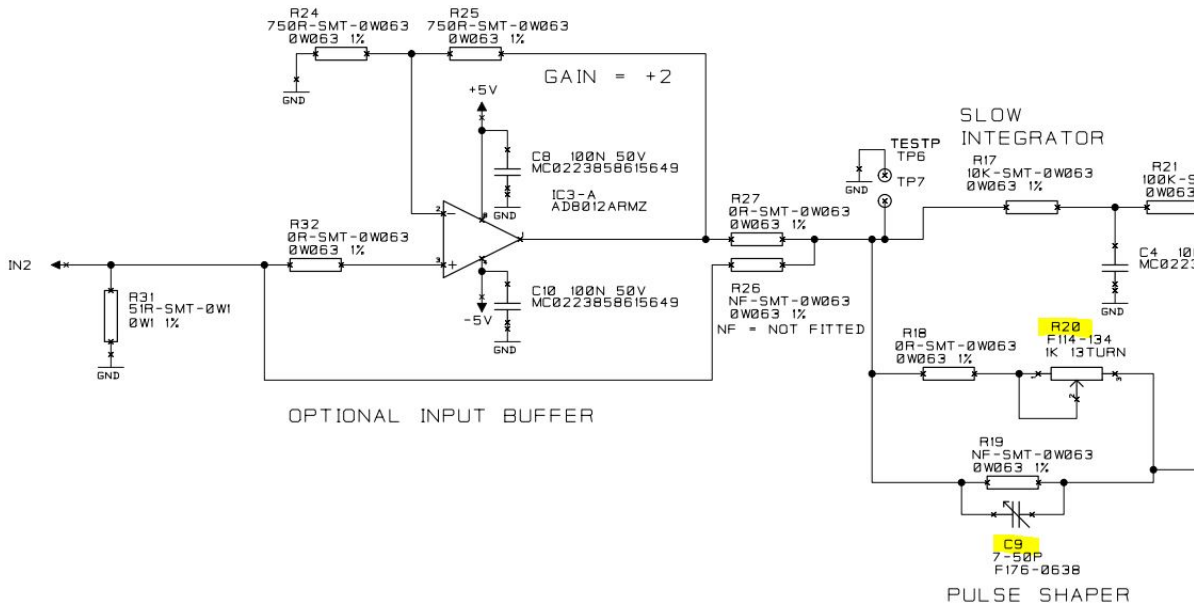


Figure 59: Full schematic of the shaper developed at the University of Leicester.

1462
1463

G Pulse Area and Height Spectra

1464 Example pulse area spectra

H SiPM list tested at University of Nagoya**Test Samples**

Product ID	Pixel size	Cell size	Technology	Short name	Fill factor
S12572-050C	3 mm	50 µm	Standard	REF-50-3	62%
S13360-3050CS	3 mm	50 µm	LCT5	LCT5-50-3	74%
S13360-3050VE	3 mm	50 µm	LCT5, epoxy	LCT5E-50-3	74%
S13360-6050CS	6 mm	50 µm	LCT5	LCT5-50-6	74%
S13360-3075CS	3 mm	75 µm	LCT5	LCT5-75-6	74%
S13360-6075CS	6 mm	75 µm	LCT5	LCT5-75-6	82%
LVR-3050CS	3 mm	50 µm	LVR	LVR-50-3	74%
LVR-6050CS	6 mm	50 µm	LVR	LVR-50-6	74%
LVR-6075CS	6 mm	75 µm	LVR	LVR-75-6	82%
LVR-7050CS	7 mm	50 µm	LVR	LVR-50-7	74%
MicroFJ-SMA-60035	6 mm	35 µm	TSV	FJ-35-6	?
FBK NUV	6 mm	30 µm	NUV	NUV-30-6	49%

Roadmap for Procurement of SiPMs
GCT Meeting, Amsterdam, FEB 15–17 2017

3/11

Figure 60: List of devices in testing at the University of Nagoya, Japan. Taken from [24]

I CHEC-S pixel comparison

1469 Comparison of results from 10 different pixels on the CHEC-S (HPK S12642-1616PA-50) array.
 1470 Every pixel is analyzed with the same technique and analysis parameters.

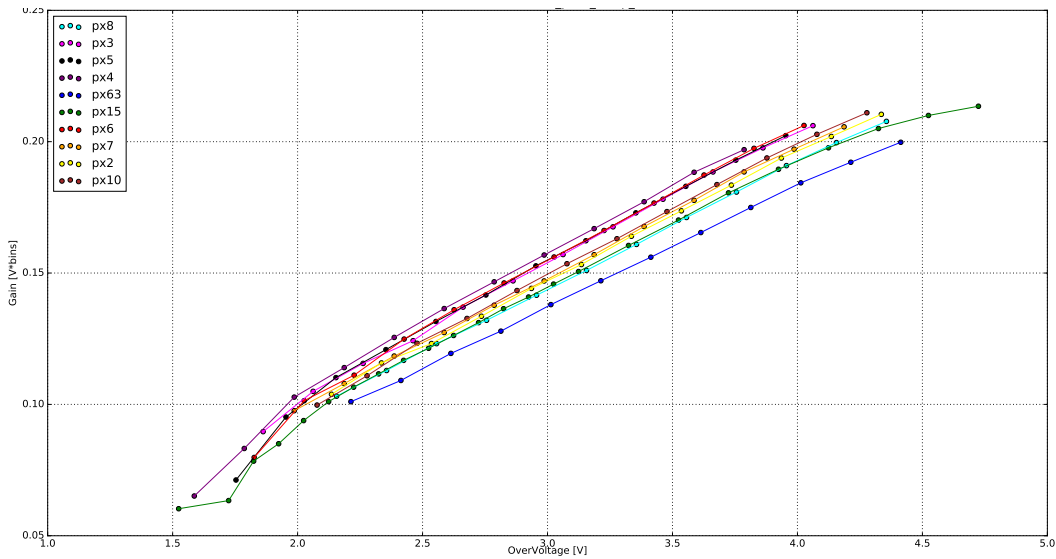


Figure 61: Gain comparison of 10 different pixels of the CHEC-S (HPK S12642-1616PA-50) array

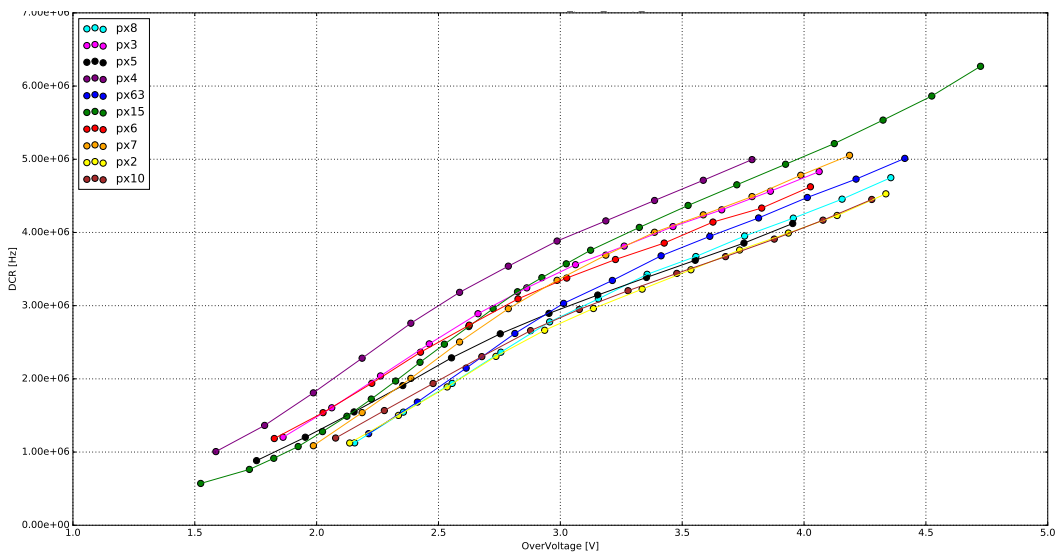


Figure 62: DCR comparison of 10 different pixels of the CHEC-S (HPK S12642-1616PA-50) array

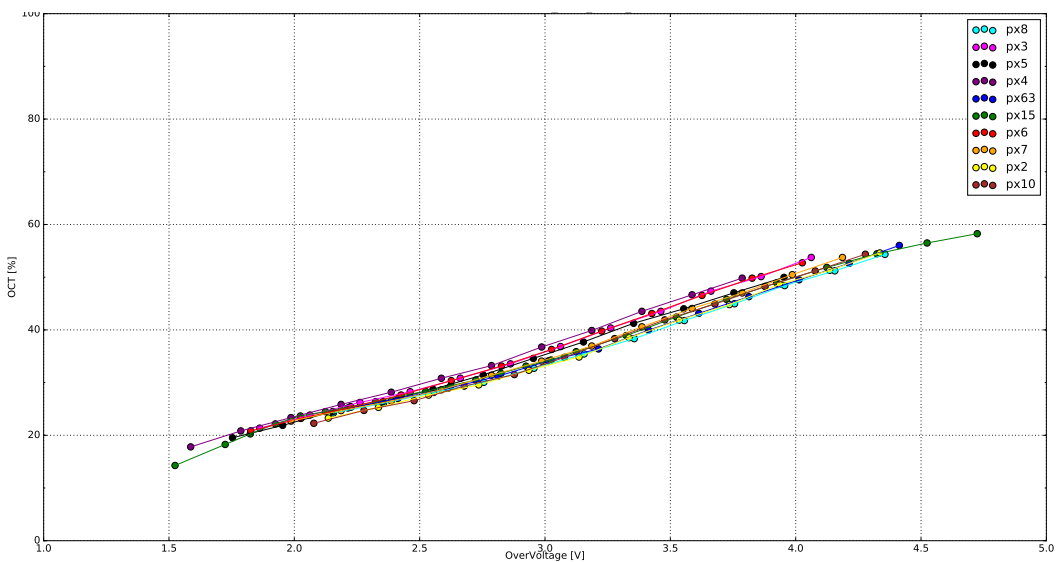
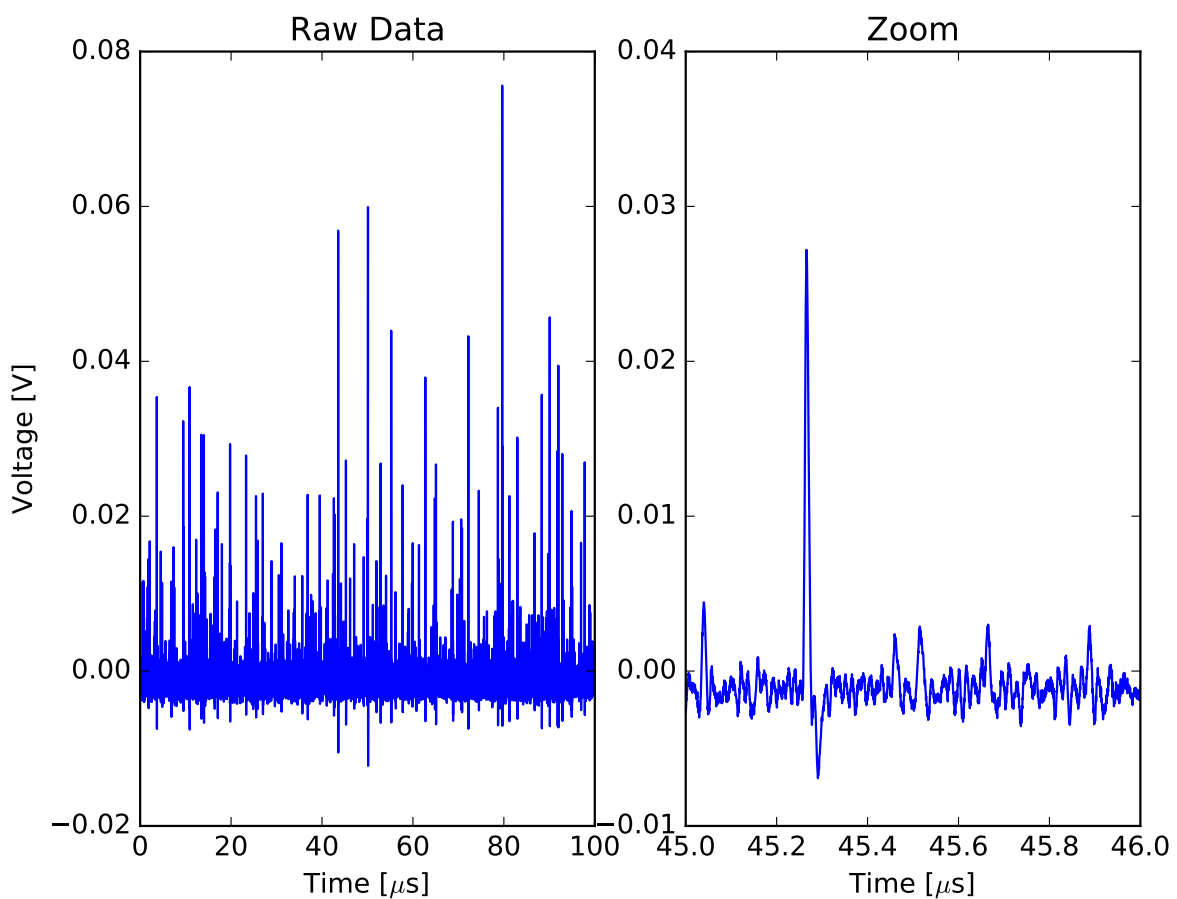


Figure 63: OCT comparison of 10 different pixels of the CHEC-S (HPK S12642-1616PA-50) array

J Additional Data Analysis Plots**Figure 64:** Description

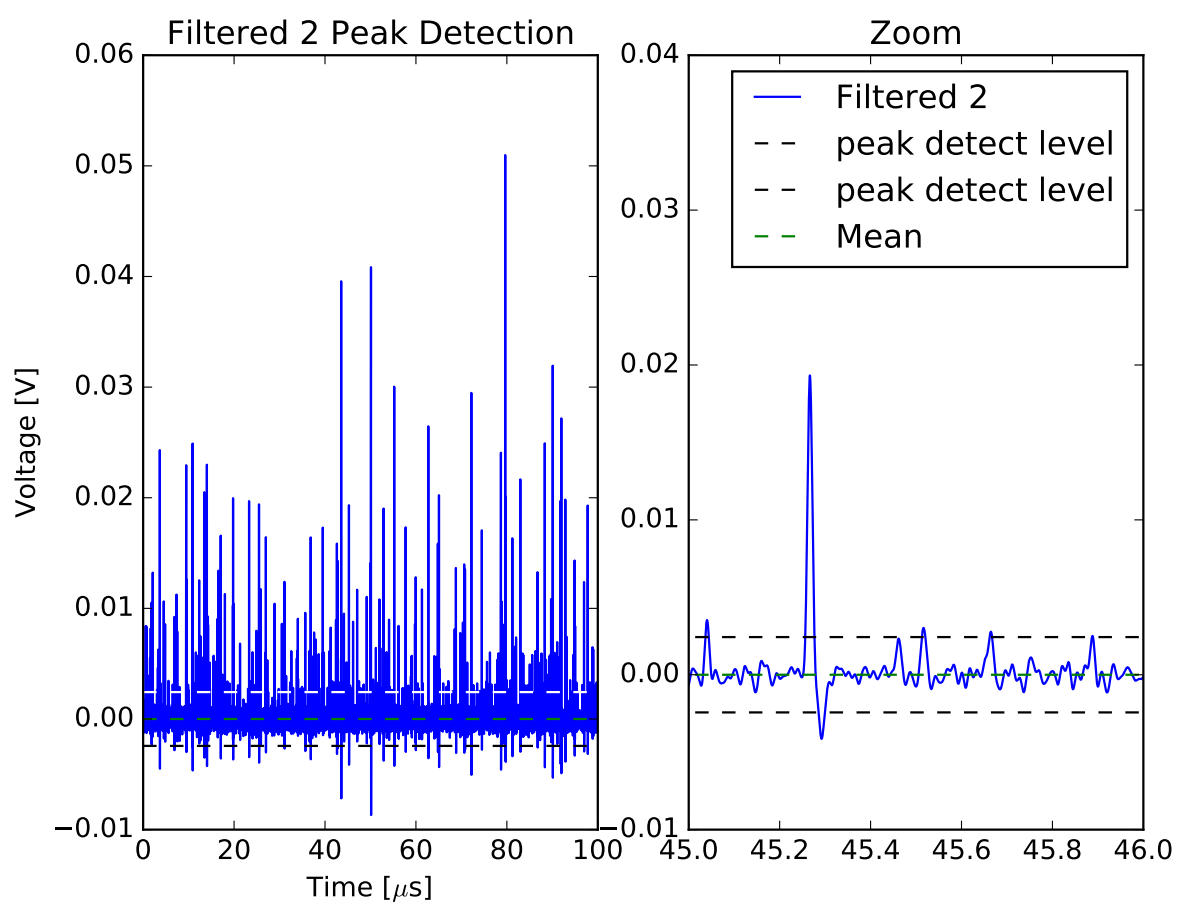


Figure 65: Description

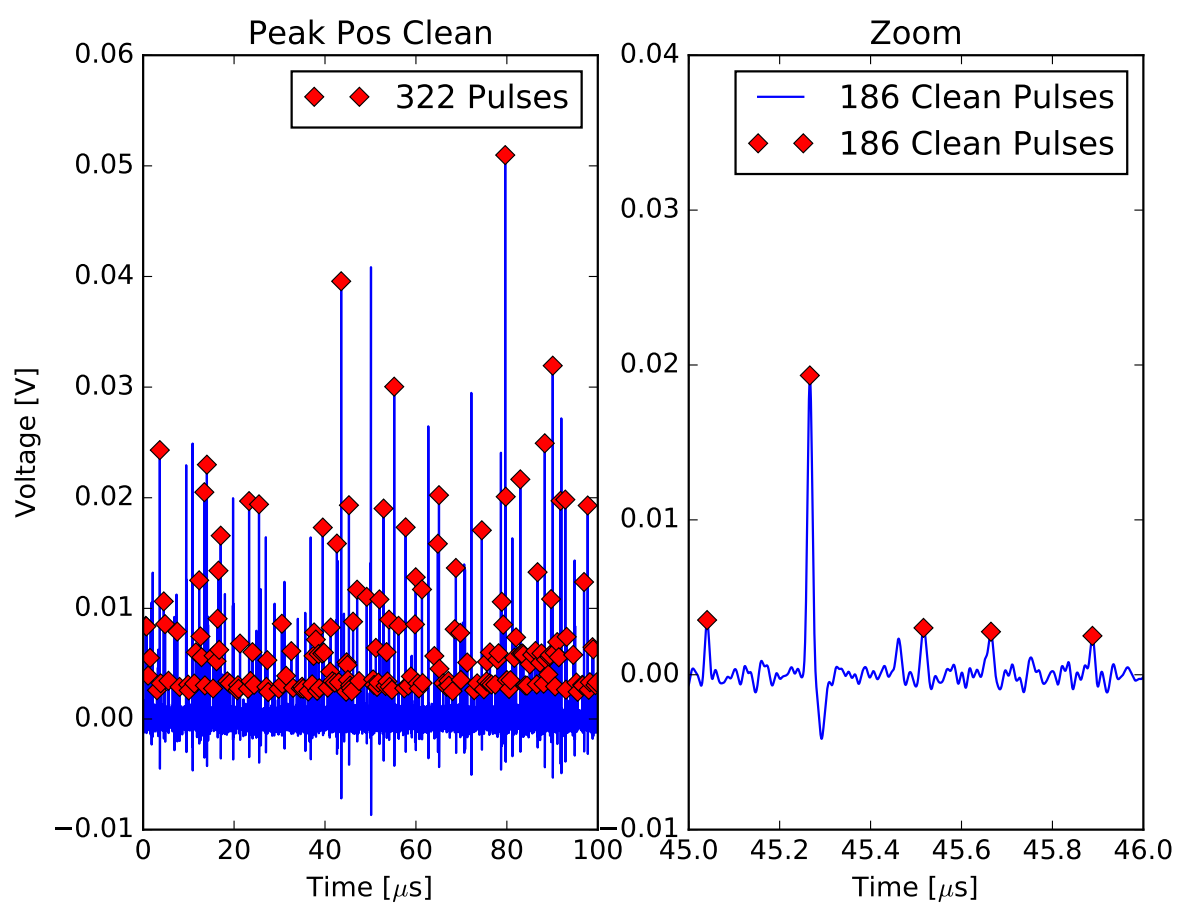


Figure 66: Description

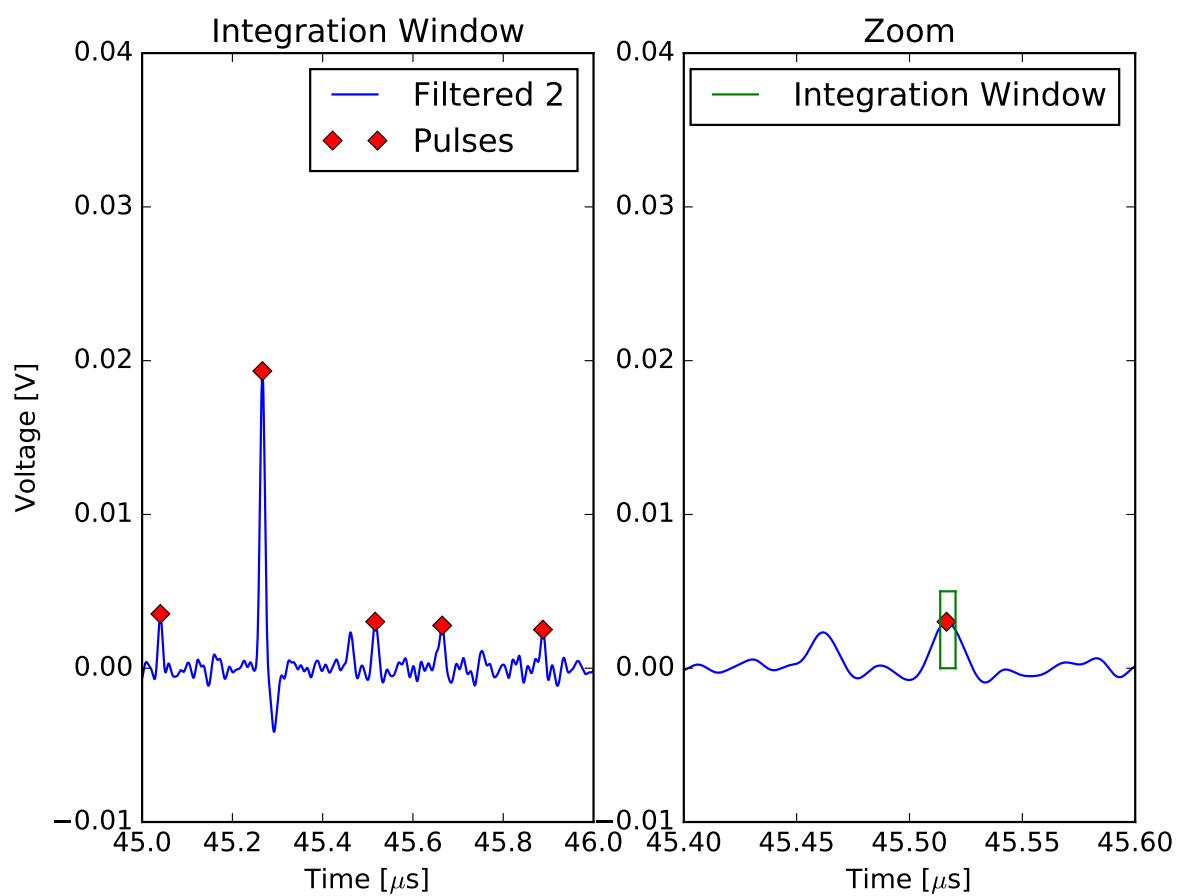


Figure 67: Description

1473 K Multi incident probability and Optical Cross Talk

1475 , _____>,

1476 With increasing Dark Count Rate the probability of two dark events happening at the same
1477 time rises with increasing bias-voltage. This has an effect on the calculated Optical Cross Talk.
1478 In the event of 2 1p.e. pulses coinciding with each other, they could be misinterpreted as 1 2p.e.
1479 pulse. Taking, for example, the Dark Count Rate of S13360, 4 MHz at $V_{ov} = 8V$ and $T = 25^\circ C$,
1480 with the FWHM of the characteristic pulse as 5.6 ns we can calculate the probability of two
1481 coinciding pulses as $\sim 2.2\%$. This probability has a direct effect on the calculated optical Cross
1482 Talk (eq:7), in reducing it compared to the calculation. The Optical Cross Talk at this point is
1483 only $\sim 17\%$, but a $\sim 2.2\%$ shift of the number events $N_{events(\geq 1.5p.e.)}$ to $N_{events(\geq 0.5p.e.)}$ lowers the
1484 OCT by $\sim 0.75\%$. Even though the multi hit coincidence is low, this shows that there are analysis
1485 related problems with high Dark Count Rates.

1486

1487

1488 For devices with high DCR and OCT like S12642 this effect grows in magnitude. At only
1489 $V_{ov} = 4.5V$ at $25^\circ C$ the DCR is 6 MHz. With the pulse FWHM of 9 ns this leads to a coincidence
1490 of 5.4%. The OCT at that point is 55%, so a reduction of 5.4% of the $N_{events(\geq 1.5p.e.)}$ towards the
1491 $N_{events(\geq 0.5p.e.)}$ leads to a reduction of the OCT by 5.6%.

1492 Maybe a half FWHM overlap is more real, since now overlap is marked as true, even when
1493 the 2 pulses blur into a very blurry one by only "touching" with their FWHM. Dont know, maybe
1494 half fwhm would be more real.

1495 L Prompt and delayed cross talk ratio

1496 , _____>,

1497 What happens if we take the OCT of S13360 and scale it with an expected prompt to delayed
1498 crosstalk ratio. evidence only from confidential HPK talk, need citations. Could just make new
1500 plots in HD, evaluate.

1501 Erklärung zur Master-Thesis

1502 Hiermit versichere ich, die vorliegende Master-Thesis ohne Hilfe Dritter nur mit
1503 den angegebenen Quellen und Hilfsmitteln angefertigt zu haben. Alle Stellen, die
1504 aus Quellen entnommen wurden, sind als solche kenntlich gemacht. Diese Arbeit
1505 hat in gleicher oder ähnlicher Form noch keiner Prüfungsbehörde vorgelegen.

1506 Darmstadt, den April 23, 2017

1507 _____
1508 (B. Gebhardt)